ICFO

Institut de Ciències Fotòniques

High-power, fiber-laser-pumped frequency conversion sources for the ultraviolet

Enrique Sánchez Bautista

Universitat Politècnica de Catalunya

Barcelona, September 2015

Doctorate Program: **Photonics**

Duration: **2011-2015**

Thesis advisor: **Prof. Dr. Majid Ebrahim-Zadeh**

Thesis co-advisor: **Dr. Chaitanya Kumar Suddapalli**

Thesis submitted in partial fulfillment of the requirements

for the degree of Doctor of Philosophy of the

Universitat Politècnica de Catalunya

September 2015

Dedicated to my loving parents and young brothers

Declaration

I hereby declare that the matter embodied and presented in the thesis entitled, **"High-power, fiber-laser-pumped frequency conversion sources for the ultraviolet"** is the result of investigations carried out by me at the ICFO – The Institute of Photonic Sciences, Castelldefels, Barcelona, Spain, under the supervision of Prof. Dr. Majid Ebrahim-Zadeh and Dr. Chaitanya Kumar Suddapalli, and that it has not been submitted elsewhere for the award of any degree or diploma. In keeping with the general practice in reporting scientific observations, due acknowledgment has been made whenever the work described is based on the findings of other investigators.

_____

Mr. Enrique Sánchez Bautista

Certificate

I hereby certify that the matter embodied and presented in this thesis entitled, "**High-power, fiber-laser-pumped frequency conversion sources for the ultraviolet**" has been carried out by Mr. Enrique Sánchez Bautista at the ICFO – The Institute of Photonic Sciences, Castelldefels, Barcelona, Spain, under my supervision, and that it has not been submitted elsewhere for the award of any degree or diploma.

_____

Prof. Dr. Majid Ebrahim-Zadeh

(ICFO, Research supervisor)

_____

Dr. Chaitanya Kumar Suddapalli

(ICFO, Research co-supervisor)

Acknowledgements

It is impossible to describe and condensate in few lines what I lived in four years. All this period has been a continuous learning process, both academically and personally, in which I have dealt with diverse circumstances and goals that were completely out of my imagination that had made this period the richest in experiences and learning of my life.

First and foremost, I want to express my sincere gratitude to Prof. Majid Ebrahim-Zadeh for giving me the opportunity to pursue doctoral studies under his supervision. He always knows how to create a perfect environment for working in the research group. He gave me the opportunity and freedom to be right and to be wrong; he knows my path here has had bright and dark spots, and he always gave me truthful advices on any topic. Moreover, I want to express my very best gratitude to Dr. Chaitanya Kumar Suddapalli who has been my thesis co-supervisor. This thesis will not be possible without his help, perseverance and sincere advices. I will always remember our conversations and his hard-working-oriented personality is an example to me that I will remember forever. Chaitanya imprints a character, and I am taking that with me. Additionally, this thesis is the fruit of collaboration with very bright people from my group: Kavita, Adolfo, Ossi, Shahrzad, Josep, and Junxiong. Ramaiah have been almost a second mentor and my best *roomie*. Really, thank you!

I want to express my best gratitude to Prof. Lluís Torner, Director of the ICFO for creating this wonderful place for research and personal development. I believe how good a place for work is depends on how big the smile of its workers are, and just a glance is necessary to realize ICFO is unbeatable. All the administration team at ICFO

(management, IT, HR, logistics, etc.) facilitated our daily work, allowing us really focus in top research and cutting-edge technology. But not only research and technology; are the leadership techniques, the personal development courses and the entrepreneurial spirit that everyday involves to each and every ICFOnian what makes the difference between a *great* place and a *top* place. I am embedded in this philosophy and I truly believe ICFO is addressed to create new world leaders in the future. Additionally, I would also like to thank the KTT unit for giving me the possibility of organizing outreach activities parallel to my daily work. I also thank to my peers at ICONS with whom I could learn and develop many activities. I surely believe *top*-profile people are *broadband*-profile people and both –KTT and ICONS–, are key elements to make better researchers, better leaders and better people. Lluís, thank you for creating this wonderful place!

I would also want to thank to my teachers from Universidad Complutense de Madrid, where I had the pleasure to study my degree in Physics, learn and become an adult. And my condolences to Prof. Paz Godino Gómez, who I had the pleasure to work with and who passed away few months ago.

During my time in Barcelona I have got the opportunity to meet many wonderful people from different countries and continents. Special thanks to these people that has been part of my time here, from which I could learn, share different visions about politics, society, enjoy moments and a very long etcetera. Particular thanks to Alejandro, Salva, Michael, Miriam, José and Katy, who helped me with the corrections into English. I am also grateful to all those who stayed back when I came to Barcelona to pursue for my doctoral studies. It is a pleasure to thank to all my friends from Madrid. Edu, Rupe, Iván, Jorge, Busta, Felipe and Anita. Special thanks to my samba band, *Samba Da Rua*. I still remember the farewell surprise you made me when I came here. To all of you, thank you!

I have also been gifted with a wonderful family that believed in me and supported

me along all this time. Special thanks to my mum and my dad. You know better than anyone how has been this path today I am finishing and I am very proud of you. It is a pleasure to remember and thank to my *tía* Carola, because she recommended me one day to study physics. And my very best thank and gratitude to Jennifer, not only for helping me in the translation into Catalan. You have been the best surprise I could have during these four years and I am very grateful for your unconditional support. Really, thank you!

And I have no words to my grandfather. Long time ago you are not with me but this is the result of the promise I made you long time ago. I remember you every day when I listen your song while running. You are the best example I could have in my life. *¡Muchas gracias!*

Abstract

High-power, stable, high-repetition-rate, picosecond ultraviolet (UV) sources are of crucial importance for a variety of applications, such as atmospheric sensing, spectroscopy or optical data storage. Further, precise material processing or laser patterning requires high energy sources with ultrashort pulses for increased accuracy.

Nonlinear, single-pass, frequency conversion sources present a highly effective and simplified approach to cover the UV spectral regions inaccessible to lasers, offering potential solutions for many of the applications mentioned above. The development of high-average-power UV sources through third- and fourth-harmonic generation (THG and FHG, respectively) of 1064 nm fiber lasers in nonlinear crystals is of particular importance due to their compact footprint, high efficiency, long lifetime, excellent stability and cost-effective design. The features of these sources are strongly dependent on the choice of the nonlinear crystal. For UV generation, this choice is particularly challenging when low-intensity picosecond pulses at high repetition rates are involved. Borate-based birefringent crystals are the most viable candidates for UV generation in the absence of suitable periodically-poled nonlinear materials, and are readily available.

This thesis presents the development of high-power frequency conversion sources for the UV spectral range, employing different experimental configurations and nonlinear crystals, making them compact, reliable and low cost designs. In particular, the nonlinear crystals β-BaB$_2$O$_4$ (BBO) and BiB$_3$O$_6$, (BIBO), with better optical, thermal and phase-matching properties for THG and FHG, are shown to be the materials of choice for the development of efficient high-average-power picosecond UV sources. A commercial

high-power Yb-fiber laser at 1064 nm has been exploited as the pump source in the work presented in this thesis.

Firstly, we have demonstrated a simple, inexpensive and novel UV source at 355 nm comprising two stages in an innovative multicrystal scheme. This involved two BIBO crystals efficiently addressing the effects induced by the birefringence of the material while implementing optimal focusing techniques. This source was capable of simultaneously generating the second- and third-harmonic of a high-power, picosecond Yb-fiber laser at 1064 nm, delivering excellent stability and high quality beam profile.

Moreover, efforts to refine the THG efficiency led to a successful improvement of the aforementioned fiber-based source at 355 nm. This was achieved by deploying a single-pass second-harmonic generation (SHG) under noncritical phase-matching in LiB_3O_5 (LBO) crystal, which considerably enhanced the output power and improved the overall performance with regard to stability and beam quality in the green, that are technologically important for a diverse range of technological applications. The obtained results at 355 nm confirm the viability of BIBO as a highly attractive material for efficient generation of low-intensity, high-average-power picosecond pulses in the UV.

Further, we demonstrated a fiber-based high-repetition-rate UV source at 266 nm based on single-pass FHG in BBO crystal in a simple and practical design. Using direct single-pass SHG of 1064 nm in LBO as a pump source for the BBO crystal, 1.7 W of output power at 266 nm was generated in a high beam quality with excellent stability and spectral features. This compact and robust design represents the highest single-pass efficiency and average power of a MHz-repetition-rate picoseconds UV source at 266 nm ever demonstrated.

Resumen

Las fuentes estables de luz pulsada en el ultravioleta (UV) en el régimen de picosegundos con altas frecuencias de repetición y de alta potencia juegan un papel crucial en gran cantidad de aplicaciones. Alguno de estos ejemplos son la detección atmosférica de gases, técnicas de espectroscopia o el almacenamiento óptico de datos. Además, las nuevas técnicas de procesado de materiales y de grabado láser requieren estas fuentes de pulsos ultracortos de alta potencia para conseguir los más altos niveles de precisión.

En este sentido, las fuentes no lineales de radiación basadas en la conversión de frecuencias de paso único presentan las mejores características para cubrir dicha región espectral a día de hoy inaccesible a los láseres convencionales, ofreciendo un amplio abanico de soluciones para todas las aplicaciones anteriormente mencionadas. El desarrollo de estas fuentes de luz de alta potencia basadas en la generación del tercer y cuarto armónico (THG y FHG de sus siglas en inglés) de láseres de fibra de 1064 nm son de gran interés gracias a su compacto diseño, alta eficiencia, larga vida, excelente estabilidad y buena relación calidad-precio. Las características de estas fuentes están fuertemente determinadas por la elección del cristal no lineal que se utilice. La generación de radiación UV presenta particulares dificultades cuando se trata de pulsos de picosegundos a baja intensidad con altas frecuencias de repetición. En estos casos, los cristales birrefringentes de la familia de los boratos son los candidatos más atractivos para la generación de esta radiación dada la ausencia de materiales no lineales periódicamente polarizados adecuados para este fin.

En esta tesis se presenta el desarrollo de varias fuentes de UV de alta potencia

basadas en la conversión de frecuencias, empleando diferentes configuraciones experimentales así como distintos cristales no lineales, construyendo diseños compactos, fiables y de bajo coste. En concreto, se escogieron los cristales relativamente nuevos, β-BaB_2O_4 (BBO) y BiB_3O_6, (BIBO), para nuestras fuentes de UV. Estos presentan mejoras sustanciales en las propiedades ópticas, térmicas y de ajuste de fases para THG y FHG. Por otro lado, en los trabajos presentados en esta tesis se utilizó un láser de fibra de iterbio a 1064 nm como fuente de bombeo.

En primer lugar, se demostró una novedosa fuente de UV de 355 nm comprendida por dos etapas en un simple e innovador esquema multicristal. Este incluye dos cristales BIBO que amplifican eficientemente los efectos inducidos por su propia birrefringencia. Esta fuente generó simultáneamente el segundo y tercer armónico de un láser de fibra de iterbio a 1064 nm de alta potencia, presentando una excelente estabilidad con un perfil en el haz de alta calidad. Además, se depuraron al máximo las técnicas para un óptimo enfoque y el consiguiente aumento de la eficiencia.

En segundo lugar, gracias a los esfuerzos para incrementar la eficiencia del THG se obtuvieron mejoras sustanciales respecto a la anterior fuente de UV de 355 nm. La generación del segundo armónico (SHG de sus siglas en inglés) se realizó implementando un cristal LiB_3O_5 (LBO), que presenta ajuste de fases no crítico de paso único. Gracias a ello, se incrementó la potencia y se mejoraron las características de salida de la fuente como la estabilidad y la calidad del haz de 532 nm, las cuales son importantes para diversas aplicaciones tecnológicas. Posteriormente se procedió, como en el caso anterior, a sumar las frecuencias –1064 nm y 532 nm–, obteniendo unos resultados a 355 nm que confirman la viabilidad del BIBO como un excelente material para generar eficientemente pulsos de picosegundos de baja intensidad en el UV.

Por último, también demostramos una fuente de radiación de 266 nm con alta

frecuencia de repetición basado en FHG de paso único usando un cristal BBO mediante un diseño simple y práctico. Utilizando el SHG de 1064 nm de paso único generado en un cristal LBO como fuente de bombeo para el cristal BBO, pudimos generar hasta 1.7 W de potencia de salida a 266 nm, presentando un haz de gran calidad con unas excelentes características espectrales y de estabilidad. Este diseño, compacto y robusto, presenta la mayor eficiencia de paso único y potencia media en una fuente de 266 nm de picosegundos con frecuencia de repetición de MHz jamás demostrada.

Resum

Les fonts estables de llum polsada en l'ultraviolat (UV) en el règim de picosegons amb altes freqüències de repetició i d'alta potència, juguen un paper crucial en gran quantitat d'aplicacions. Algun d'aquests exemples són la detecció atmosfèrica de gasos, tècniques d'espectroscòpia o l'emmagatzemat òptic de dades. A més a més, les noves tècniques de processat de materials i de gravat làser requereixen aquestes fonts de polsos ultracurts d'alta potència per aconseguir els més alts nivells de precisió.

En aquest sentit, les fonts de radiació no lineal basades en la conversió de freqüències de pas únic presenten les millors característiques per cobrir aquesta regió espectral a dia d'avui inaccessible als làsers convencionals, oferint un ampli ventall de solucions per totes les aplicacions anteriorment esmentades. El desenvolupament d'aquestes fonts de llum d'alta potència basades en la generació del tercer i quart harmònic (THG i FHG per les seves sigles en anglès) del làser de fibra de 1064 nm són de gran interès gràcies al seu compacte disseny, alta eficiència, llarga vida, excel·lent estabilitat i bona relació qualitat-preu. Les característiques d'aquestes fonts estan fortament determinades per l'elecció del cristall no lineal que s'utilitzi. La generació de radiació UV presenta particulars dificultats quan es tracta de polsos de picosegons a baixa intensitat amb altes freqüències de repetició. En aquests casos, els cristalls birefringents de la família dels borats són els candidats més atractius per la generació d'aquesta radiació donada l'absència de materials no lineals periòdicament polaritzats adequats per aquesta finalitat.

En aquesta tesi es presenta el desenvolupament de diverses fonts d'UV d'alta

potència basades en la conversió de freqüències, emprant diferents configuracions experimentals així com diferents cristalls no lineals, construint dissenys compactes, fiables i de baix cost. En concret, es van escollir els cristalls relativament nous, β-BaB$_2$O$_4$ (BBO) i BiB$_3$O$_6$, (BIBO), per les nostres fonts d'UV. Aquests presenten millores substancials pel que fa a les propietats òptiques, tèrmiques i d'ajust de fases per THG i FHG. D'altra banda, en els treballs presentats en aquesta tesi es va utilitzar un làser de fibra d'iterbi a 1064 nm com a font de bombeig.

En primer lloc, es va demostrar una nova font d'UV de 355 nm que consta de dues etapes en un simple i innovador esquema multi-cristall. Aquest inclou dos cristalls BIBO que amplifiquen eficientment els efectes induïts per la seva pròpia birefringència. Aquesta font va generar simultàniament el segon i tercer harmònic d'un làser de fibra d'iterbi a 1064 nm d'alta potència, presentant una excel·lent estabilitat amb un perfil al feix d'alta qualitat. A més a més, es van fer servir al màxim les tècniques per un òptim enfocament i el consegüent augment de l'eficiència.

En segon lloc, els esforços per incrementar l'eficiència del THG van resultar en millores substancials respecte l'anterior font d'UV de 355 nm. La generació del segon harmònic (SHG per les seves sigles en anglès) es va realitzar mitjançant la implementació d'un cristall LiB$_3$O$_5$ (LBO), que presenta un ajust de fases no crític de pas únic. Gràcies a aquesta acció, es va realçar la potència i es van millorar les característiques de sortida de la font com l'estabilitat i la qualitat del feix de 532 nm, les quals són importants per diverses aplicacions tecnològiques. Posteriorment es va procedir, com en el cas anterior, a sumar les freqüències –1064 nm i 532 nm–, obtenint uns resultats a 355 nm que confirmen la viabilitat del BIBO com un excel·lent material per generar eficientment polsos de picosegons de baixa intensitat en el UV.

Per últim, també vam demostrar una font de radiació de 266 nm amb un alta

freqüència de repetició basat en FHG de pas únic utilitzant un cristall BBO mitjançant un disseny simple i pràctic. Utilitzant el SHG de 1064 nm de pas únic generat en un cristall LBO com a font de bombeig per el cristall BBO, va poder generar fins a 1.7 W de potència de sortida a 266 nm, presentant un feix de gran qualitat amb unes excel·lents característiques espectrals i d'estabilitat. Aquest disseny és compacte i robust, presenta la major eficàcia de pas únic i potència mitja en una font de 266 nm de picosegons amb freqüència de repetició de MHz mai demostrada fins ara.

Publications

1. S. Chaitanya Kumar, J. Canals Casals, **E. Sánchez Bautista**, K. Devi and M. Ebrahim-Zadeh: "*1.8 W, 80 MHz, picoseconds, Yb-fiber-based ultraviolet sources at 266 nm using β-BaB$_2$O$_4$,*" *Optics Letters*, **40**(10), 2397-2400 (2015).

2. S. Chaitanya Kumar, **E. Sánchez Bautista** and M. Ebrahim-Zadeh: "*Stable, high-power, Yb-fiber-based, picosecond ultraviolet generation at 355 nm using BiB$_3$O$_6$,*" *Optics Letters*, **40**(3), 403-406 (2015).

3. S. Chaitanya Kumar, **E. Sánchez Bautista** and M. Ebrahim-Zadeh: "*Stable, high-power, Yb-fiber-based, picosecond ultraviolet generation at 355 nm using BiB$_3$O$_6$,*" *Virtual Journal for Biomedical Optics*, **10**(3), (2015).

4. S. Chaitanya Kumar, J. Canals Casals, **E. Sánchez Bautista**, K. Devi and M. Ebrahim-Zadeh: "*1.8 W, 80 MHz, picoseconds, Yb-fiber-based ultraviolet sources at 266 nm using β-BaB$_2$O$_4$*", CLEO-Europe, Munich, Germany, June 2015.

5. S. Chaitanya Kumar, **E. Sánchez Bautista** and M. Ebrahim-Zadeh, "*1.2 W-average-power, Yb-fiber-pumped, picosecond ultraviolet source at 355 nm based on BiB$_3$O$_6$,*" CLEO-USA, San Jose, 2015.

6. S. Chaitanya Kumar**, E. Sánchez Bautista** and M. Ebrahim-Zadeh: "*Stable, high-power, fiber-based, picosecond ultraviolet source at 355 nm*", PhD Open Days, ICFO – The Institute of Photonic Sciences, December 2014.

7. S. Chaitanya Kumar**, E. Sánchez Bautista** and M. Ebrahim-Zadeh: "*Stable, high-power, fiber-based, picosecond ultraviolet source at 355 nm,*" Paper: WeP-T1-P-19, 6th EPS-QEOD Europhoton Conference, Neuchatel, Switzerland, August 2014.

Simplicity is the ultimate form of sophistication.

Leonardo da Vinci

High-power, fiber-laser-pumped

frequency conversion sources for the

ultraviolet

Contents

List of tables

List of figures

1 Introduction

The laser has become one of the key developments of the last century with widespread use in our daily life. Since the invention of the laser [1], it has experienced tremendous progress in the last few decades, becoming omnipresent in various industrial and medical techniques, communications, illumination and many other applications playing an irreplaceable role in different aspects of our society. The laser can provide the most spectrally pure light based on stimulated emission between quantized energy levels in the active medium within the laser device. This property, together with its direct generation and easy manipulation, has made the laser a remarkable tool in many applications. From reading bar codes to aerospace communications, our welfare and technological development of society requires laser at countless different levels in various practical applications. Some of them need high output power as well as high efficiency, stability and good beam profile. Broad wavelength tunability is also required for numerous applications [2].

However, more than 50 years after the invention of the laser, substantial portions of the optical spectrum from the ultraviolet (UV) to the infrared (IR) remain inaccessible to conventional laser sources, due to the restricted availability of suitable gain media.

Nonlinear optical techniques based on frequency conversion of laser light in second-order nonlinear materials offer a highly effective method to expand the spectral range of existing laser sources, overcoming the spectral limitations of lasers [3,4].

Nonlinear optics, and in particular nonlinear frequency conversion, has pushed the barriers of knowledge and technology, leading to the development of coherent light sources and enabling access to the above-mentioned spectral regions not covered by conventional lasers. Moreover, nonlinear frequency conversion provides a flexible capability of generating both single frequency photons or a wavelength tunability across extended spectral regions from a single device depending on our technological needs [5,6]. At the same time, the instantaneous nature of nonlinear gain allows frequency conversion processes to keep the temporal characteristics of the input pump laser, thus enabling wavelength generation in all temporal regimes from the continuous wave (cw) to ultrafast femtosecond time scales upon the choice of the pump laser [3]. These capabilities are of great interest for variety of applications such as spectroscopy, biomedicine, remote sensing and environmental monitoring [7].

The concept of the parametric processes was first reported at the beginning of the 20th century [8]. In 1926, S. Vavilov and V. L. Levishin, found a reduction in the light absorption by uranium doped glass as the intensity of light was increased [8]. Afterwards, C. V. Raman in 1928 [9] discovered spontaneous scattering of photons into new frequencies passing through a transparent medium.

The term *nonlinear optics* was introduced in 1943 by E. Schrodinger [10,11]. Nonlinear optics describes the nonlinear response of a material when an electromagnetic field propagates inside it. Typically, for the observation of this phenomenon an electromagnetic field strong enough to induce a nonlinear response within the material is necessary. With the invention of laser in 1960 by T. Maiman [1], a new field in the study

16

of various nonlinear optical phenomena was opened [1] that still remains today. Under the exciting opportunity of having this new device in his laboratory, in 1961, P. A. Franken decided to rent a ruby laser form Trion Instruments Inc., the first company to manufacture ruby lasers, in order to investigate the unprecedented optical intensities that were available from that moment by using that exciting new device. Technically, the laser provided 3 J, 1 ms-long pulses at 694.3 nm, that were focused into a quartz crystal, thus successfully demonstrating the first observation of second-harmonic generation (SHG) at 347.2 nm [12]. The description of the SHG effect gave way to a significant field of research, which in the following years, led to some of the most important milestone developments in the field of nonlinear optics. In January 1962, M. Bass *et al.* [13], reported the first experimental observation of frequency mixing by deploying two ruby lasers from the same company – again Trion Instruments Inc. –, operating them at different output frequencies separated by 1 nm. They could obtain such a difference in the generated wavelengths by letting one laser work at room temperature whereas the other one was cooled down to liquid nitrogen temperature. By pumping various crystals with these wavelengths, they found that 'triglycine sulfate' was the most effective nonlinear crystal at the time generating optical harmonics, and therefore leading to the first experimental observation of sum-frequency generation (SFG). However, both SHG and SFG presented very low conversion efficiencies. On the other hand, in order to generate an efficient nonlinear frequency conversion process, in other words, to obtain high conversion efficiencies, it is required to have a proper phase relationship between the interacting waves along the propagation direction within the nonlinear media. This relationship is denominated as the *phase-matching* condition. The theoretical concept of phase-matching was proposed even before the invention of laser in 1958 by P. K. Tien in the context of radio waves [14,15]. However, it was first demonstrated in 1962 by

Event	Authors	Reference	Year
First report of an optical nonlinearity effect	S. Vavilov *et al.*	[8]	1926
Discovery of the Raman scattering or Raman effect	C. V. Raman *et al.*	[9]	1928
Theoretical postulation of the concept of phase-matching in radio waves	P. K. Tien	[14,15]	1958
First demonstration of laser	T. H. Maiman	[1]	1960
First experimental demonstration of SHG	P. Franken *et. al.*	[12]	1961
Publication of the article "Interaction between light waves in a nonlinear dielectric"	J. A. Armstrong *et. al.*	[4]	1962
First demonstration of experimental observation of frequency mixing (SFG)	M. Bass *et. al.*	[13]	1962
First demonstration of the phase-matching condition	J. A. Giordmaine *et al.*	[16]	1962
Theoretical postulation of optical parametric generation (OPG)	R. H. Kingston *et al.*	[17]	1962
First theoretical proposal of optical parametric oscillator (OPO)	N. M. Kroll	[18]	1962
First observation of THG	R. W. Terhune *et al.*	[19]	1962
First demonstration of difference-frequency generation (DFG)	A. W. Smith *et. al.*	[20]	1963
First experimental demonstration of an OPO	J. A. Giordmaine *et al.*	[21]	1965
First demonstration of continuous-wave OPO	R. G. Smith *et al.* R. L. Byer *et al.*	[22] [23]	1968
First implementation of periodic poling technology 40 years after its postulation	S. Matsumoto *et. at.*	[24]	1991

Table 1.1: Advances in nonlinear optics.

J. A. Giordmaine *et al.* [16], although phase-matching was also suggested by P. D. Maker *et al.* [25] in the same year. Right after, R. W. Terhune *et al.* [19], described the first observation of third-harmonic generation (THG) in May 1962, and later in 1963 A. W. Smith and N. Braslau demonstrated the first difference-frequency generation (DFG) experiment [20]. During the same period, the importance of parametric generation and amplification was highlighted as an important technique for the generation of tunable coherent radiation in new spectral regions [17,18,26], opening the possibility to the first corroboration of the optical parametric generation (OPG) processes. This led to the first experimental demonstration of a pulsed optical parametric oscillator (OPO) by J. A. Giordmaine and R. C. Miller in 1965 [21], followed independently by R. G. Smith *et al.* [22] and R. L. Byer *et al.* [23] with the first demonstration of continuous-wave OPOs in 1968. Table 1.1 shows some of the most important milestones in the field of nonlinear optics.

Although, since then, the basic principles behind frequency conversion processes have been well developed and understood, the unavailability of suitable pump lasers and proper nonlinear optical materials have hindered the extension of these techniques to different wavelength regions and time-scales [27]. For this reason, access to extended regions in the UV, visible and IR has remained difficult because of the absence of suitable solid-state gain materials [28]. Even today, after a period of well-established implementation of laser technology in our daily lives, wide regions of the optical spectrum in the UV remain inaccessible to conventional mode-locked laser sources [3]. Figure 1.1 shows the wavelength of some of the UV lasers commercially available.

Time-domain spectroscopy, including quantum optics, optical data storage, atmospheric sensing, combustion diagnostics and bio-imaging are some, but not all, of
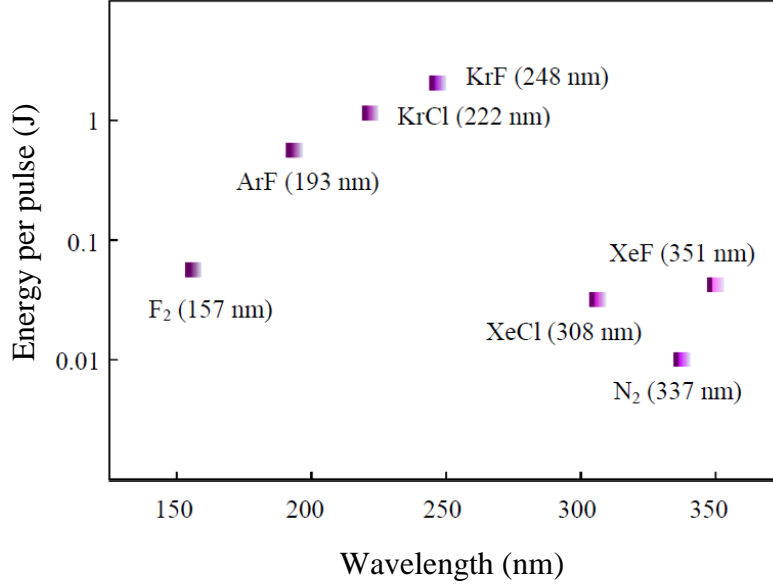
Figure 1.1: Spectral coverage of conventional UV lasers.

the promising applications with a strong need for stable, coherent and high-beam-quality sources in the UV [29,30]. Previously, access to this spectral region was achieved with excimer lasers, however, their bulky complex and power-hungry gas gain media required massive installations, making them unviable for many applications. These facts kept the interest of researchers and industry in the development of high-repetition-rate UV sources at practical average power and efficiency, in simple, compact, cost-effective and practical architecture.

The advent of new optical materials, together with the development of new nonlinear optical techniques based on frequency conversion of laser light in second-order nonlinear materials, has paved the way to reach some of the inaccessible regions in the UV spectrum, offering a highly effective method to expand the wavelength range of existing laser sources. The above mentioned nonlinear frequency conversion techniques –SHG and SFG– can provide spectral extension of laser sources to shorter wavelengths,

making them a promising, but still challenging, method of coverage of the UV region at high efficiency and practical powers.

Any frequency conversion process is inherently correlated with the nonlinear optical material in which it is generated together with the input laser pump source. Both elements constitute the essential components in the practical development of any frequency conversion system. In the early 1980's, a new generation of birefringent nonlinear crystals, primarily β-BaB$_2$O$_4$ (BBO) and LiB$_3$O$_5$ (LBO), with higher damage thresholds than the previous classical nonlinear optical materials were developed. This fact, together with the advent of new crystalline solid-state and fiber lasers with improved spectral and spatial coherence as well as higher output powers, led to the development of a new family of frequency conversion sources with properties never achieved before operating in all temporal regimes, from the cw to the femtosecond time-scales. In 1991, a matured crystal growth technology for periodically poling the ferroelectric materials was achieved [24], bringing into action quasi-phase-matching (QPM) technique nearly three decades after its postulation in 1962 [4].

Today, there are well-established frequency conversion technologies for the generation of different frequencies, from mid-IR [2,7,31] to visible [32], down to the UV [33], using BBO and LBO, and the relatively new nonlinear material bismuth borate, BiB$_3$O$_6$ (BIBO), first described by H. Hellwig *et al.* [34,35] in 1999. Earlier reports demonstrated BIBO as a reliable source for UV generation by achieving THG of a mode-locked picosecond Nd:YAG laser at 355 nm [36]. Tunable pulses from 375 to 435 nm were also obtained using a mode-locked Ti:sapphire laser in the femtosecond and picosecond regime [37,38]. Recent studies also demonstrated BIBO crystal as a very promising nonlinear material for the visible [39] and the UV [40] in picosecond and cw,

respectively. Additionally, a group of periodically poled crystals such as MgO-doped periodically poled lithium niobate (MgO:PPLN), periodically poled KTiOPO$_4$ (PPKTP), as well as MgO-doped periodically poled lithium tantalate (MgO:PPLT) constitute solid and reliable materials for the mid-IR generation [41-44]. Progress in the development of new frequency conversion techniques using these crystals has led to important advances in nonlinear optics as a whole, extending the wavelength range of existing laser sources to new regions in the UV. Despite the many advances, there still remain important challenges in this technology, which should be faced by a continued research for innovative design concepts, alternative new nonlinear materials, and different laser pump sources.

The context of the research work presented in this thesis is built on well-established frequency conversion methods, while significantly improving previous techniques, leading to improved results using simple and reliable concepts for the generation of UV wavelengths in the picosecond regime. All the devices presented here are based on fiber laser technology, making them compact, practical and robust. Moreover, the simplicity of the properties of the BIBO crystal, which has been used in most of the steps in the experiments, can provide most of its highlighted characteristics at room temperature, emphasizing in the simplicity of the setups presented in this thesis. A desirable implementation of this technology into more complex devices or systems for engineering applications such as aerospace industry require simplicity and robustness, where typically the complexity of the payloads constitutes a limiting factor for a successful prospective mission.

This thesis is organized into 5 chapters as follows:

Chapter 2 provides a brief introduction to various nonlinear optical phenomena presented throughout this thesis, such as SHG and SFG, as well as a theoretical description of the phase-matching condition, which is crucial for effective amplification and macroscopic observation of any nonlinear effect. An in-depth analysis of the concepts of acceptance bandwidths is presented. A more extensive discussion of these concepts can be found in other References [45,46].

Chapter 3 is divided into two subsections, both of them based on the description of the highly reliable, high-power, picosecond UV sources at 355 nm, by exploiting the unique properties of the BIBO crystal. In the first subsection, we present a stable, compact, Yb-fiber-based, high-power, all-BIBO, picosecond UV source providing up to 164 mW. The compact UV source is based on a novel multicrystal scheme comprising two stages, both involving single-pass frequency conversion in BIBO. The generation of the UV was challenging due to the inherent phase-matching requirements of the SFG effect ($k_{1064} + k_{532} = k_{355}$) within the second crystal, for which the polarization of the interacting waves needed a selective rotation. The source also simultaneously generates 4.9 W of picosecond green power at 532 nm. In the second subsection, we present an improved version of the previous setup. Also, we present a stable, compact, Yb-fiber-based, high-power, picosecond UV source based on the BIBO crystal. Nevertheless, in this case, we performed single-pass SHG using LBO to provide up to 9.1 W of average green power at 532 nm. This green radiation was then sum-frequency-mixed with the fundamental in a BIBO crystal, providing up to 1.2 W of average UV power at 355 nm.

In Chapter 4 we report a stable, high-power, picoseconds UV source at 266 nm based on single-pass FHG of the Yb-fiber laser, generating as high as 1.7 W of UV power at 79.5 MHz in an elliptic Gaussain beam with a TEM$_{00}$ mode profile.

Chapter 5 provides in an overall summary of all the experiments and results presented in this thesis.

2 Basics of Nonlinear Optics

Optics is the study of the interaction between light and matter, and nonlinear optics is the field of optics that studies the phenomena that occur as a consequence of the modification of the optical properties of a material by the presence of light [45]. When an electro-magnetic field propagates in a material, the electrons are displaced with respect to the nuclei, and as a result it generates an induced polarization field in the medium [5]. In general, the response of the system to an applied optical field is linear, resulting in the penetration and propagation of several electro-magnetic waves inside the material without any interaction between the waves. However, when the incident electromagnetic fields are intense enough, an induced polarization can appear due to the intrinsic nonlinear response of the medium. Under this condition, the response of a material system to an applied optical field becomes nonlinear with the strength of the optical field [45,47]. Normally, only the laser light is sufficiently intense to modify the optical properties of the material [45], thus making the nonlinear effects observable within the material. In fact, it is broadly established that the field of nonlinear optics began with the observation of the SHG effect by P. Franken *et al.* in 1961 [12], shortly after the demonstration of the first working

laser by T. Maiman in 1960 [1].

The electromagnetic response of a material to the applied field can be considered as the dependence of the dipole moment per unit volume, or polarization, P, of the material upon the strength, E, of the applied optical field [45,47]. If the applied field is not sufficiently intense, then the induced polarization depends linearly upon the electric field strength and can be described as,

$$P = \varepsilon_0 \, \chi^{(1)} E(t) \tag{2.1}$$

where P and E are the polarization and the electric field vectors, respectively, $\chi^{(1)}$ is the linear susceptibility of the medium, and ε_0 is the permittivity of free space. However, when the strength of the interacting field is comparable to the intra-atomic electric field in the material, the response of the material is no longer linear [5]. In this case, the optical response of the material becomes nonlinear, and can be described by generalizing the equation 2.1, by expressing the polarization as a power series in the applied electric field,

$$P = \varepsilon_0 \, \chi^{(1)} E + \varepsilon_0 \, \chi^{(2)} E^2 + \varepsilon_0 \, \chi^{(3)} E^3 + \ldots = P_L + P_{NL} \tag{2.2}$$

where $\chi^{(2)}$ and $\chi^{(3)}$ are the second- and third-order nonlinear susceptibilities, respectively. The induced polarization that depends linearly upon the electric field strength can be described P_L, whereas P_{NL} corresponds to the induced polarization which is nonlinearly dependent upon the strength of the incident electric field. The work presented in this thesis is mainly based on interactions involving second-order nonlinear processes, which are governed by the second-order nonlinear susceptibility, $\chi^{(2)}$.

Nowadays, nonlinear optics is one of the most important fields of physics with diverse range of applications in many other areas of science, and lot of literature can be

found on the treatment of other higher-order interactions in a multitude of References

[4,45,46].

2.1 Second-order nonlinear processes

Any second-order optical process based on $\chi^{(2)}$ exhibits a mutual interaction of three

waves of frequencies ω_1, ω_2 and $\omega_3 = \omega_1 + \omega_2$. The induced second-order nonlinear

polarization dependent upon the strength of the three waves can be extracted from

equation 2.2 as,

$$P_{NL}(t) = \chi^{(2)}\varepsilon_0 E(t)^2 \tag{2.3}$$

Considering an optical field consisting of two distinct frequency components, ω_1 and ω_2,

incident on a second-order nonlinear optical medium,

$$E(t) = E_1(t)e^{-i\omega_1 t} + E_2(t)e^{-i\omega_2 t} + c.c. \tag{2.4}$$

Subsequently, the second-order nonlinear polarization, using the equations 2.3 and 2.4, is

given by,

$$P_{NL} = \sum_n P(\omega_n)e^{-i\omega_n t}$$

$$= \varepsilon_0\,\chi^{(2)}\big[E_1^2 e^{-2i\omega_1 t} + E_2^2 e^{-2i\omega_2 t} + 2E_1 E_2 e^{-i(\omega_1+\omega_2)t}$$

$$+2E_1 E_2^* e^{-i(\omega_1-\omega_2)t} + c.c.\big] + 2\varepsilon_0\,\chi^{(2)}[E_1 E_1^* + E_2 E_2^*]) \tag{2.5}$$

Therefore, the optical parametric processes of the three-wave interaction consist of the

following frequency-mixing processes that can be inferred from the previous expression.

Here, in the equation 2.5, the first two terms represent the SHG process, the third term

represents the SFG term and the fourth term represents the DFG process. SHG is

described schematically in Figure 2.1(a). It is the degenerate case of SFG in which a single pump wave, the fundamental at frequency ω, is incident on a nonlinear medium and generates a wave at the second-harmonic frequency 2ω. The general case of SFG involves two input waves at frequencies ω_1, ω_2 and the result of its combination $\omega_3 = \omega_1 + \omega_2$ is shown in Figure 2.1(b). In addition to these processes, DFG also involves two input waves at frequencies ω_2, ω_3 with the result of the generation of a photon at a frequency $\omega_1 = \omega_3 - \omega_2$, as shown in Figure 2.1(c). Another possible parametric process is OPG, also known as parametric down-conversion. In this process, only one input wave at frequency ω_3 leads to the generation of two lower-energy waves at frequencies ω_1 and ω_2. By convetion, the generated wave with the higher frequency is referred to as *signal*, and the wave at lower frequency is termed *idler*. This process, shown in Figure 2.1(d), both conservation laws: conservation of energy ($\omega_p = \omega_s + \omega_i$) and momentum ($k_p = k_s + k_i$) –also called phase-matching condition– must be satisfied. For efficient enhancement of the effect, and thus attainment of an appreciable conversion efficiency, it is possible to enclose the OPG system in a resonator, resulting in an OPO, which is generally used for many practical applications [48-50].

The significance of the processes described in this chapter is primarily in the area of generating coherent radiation at new frequencies that are not usually available with conventional lasers. By combining different lasers sources with different materials and nonlinear processes, tunable coherent radiation from the UV to the IR has been generated for spectroscopy, remote sensing, optical radar and other applications [46].

(a)

$$2\omega = \omega + \omega$$

$$k_{2\omega} = k_\omega + k_\omega$$

(b)

$$\omega_3 = \omega_1 + \omega_2$$

$$k_{\omega_3} = k_{\omega_1} + k_{\omega_2}$$

(c)

$$\omega_1 = \omega_3 + \omega_2$$

$$k_{\omega_1} = k_{\omega_3} + k_{\omega_2}$$

(d)

$$\omega_p = \omega_s + \omega_i$$

$$k_p = k_s + k_i$$
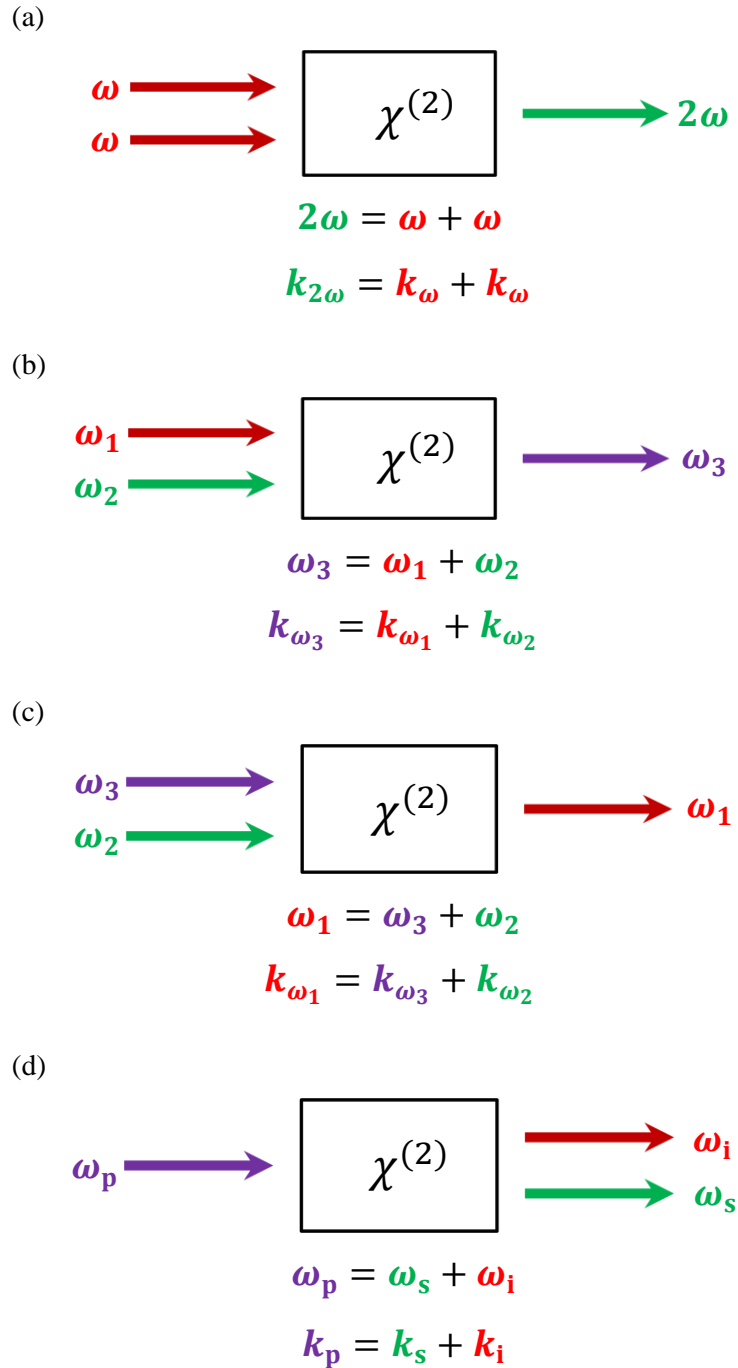
Figure 2.1: Schematic of primary second-order nonlinear processes. (a) Represents second-harmonic generation (SHG); (b) sum-frequency generation (SFG); (c) difference-frequency generation (DFG); and (d) optical parametric generation (OPG).

2.2 Nonlinear susceptibility

Previously it was described how any second-order interaction exhibits mutual interaction of three waves of frequencies ω_1, ω_2 and $\omega_3 = \omega_1 + \omega_2$. A complete description of the interaction between these three waves requires an understanding of how the nonlinear polarizations of the waves interact with each other. In order to describe these interactions, it becomes necessary use the nonlinear susceptibility in a tensor form. Focusing our attention on the second-order nonlinear susceptibility, $\chi^{(2)}$, a full description involves its representation as a tensor of 27 elements, $\chi^{(2)} = \chi_{ijk}^{(2)}$, where the indices i, j, k correspond to x, y, z, and represent the polarization of the interacting waves. At this stage, it is important to describe another notation commonly used in second-order nonlinear optics [46]. Often, the susceptibility is represented as the so-called *d*-coefficient, where the *d* is a tensor described as,

$$d_{ijk} = \frac{1}{2}\chi_{ijk}^{(2)} \tag{2.6}$$

It is often the case that in many applications all frequencies and their combination are far from any material resonance. Therefore, the susceptibilities can be treated as real quantities and any susceptibility is thus equal to its complex conjugate because the nonlinear susceptibility becomes independent of the frequency of the interacting fields, and then the dispersion can be ignored. This is known as *Kleinman symmetry* condition, fully described in many References [46,51,52]. In-depth treatment of the formal symmetry properties of the nonlinear susceptibility implies that the polarizations can be freely permutated without permutating the cartesian subscript [46]. Hence, the second-order nonlinear susceptibility tensor, $\chi_{ijk}^{(2)}$, can be transformed into a 3×6-element matrix,

$$d_{il} = \begin{bmatrix} d_{11} & d_{12} & d_{13} & d_{14} & d_{15} & d_{16} \\ d_{21} & d_{22} & d_{23} & d_{24} & d_{25} & d_{26} \\ d_{31} & d_{32} & d_{33} & d_{34} & d_{35} & d_{36} \end{bmatrix} \tag{2.7}$$

The matrix components, d_{il}, are known as the nonlinear coefficients of the material. After this consideration, introducing the d_{il} matrix within the general expression for the second-order nonlinear polarization, it is observed that,

$$\begin{pmatrix} P_x(\omega_3) \\ P_y(\omega_3) \\ P_z(\omega_3) \end{pmatrix} = 2\varepsilon_0 K \begin{bmatrix} d_{11} & d_{12} & d_{13} & d_{14} & d_{15} & d_{16} \\ d_{21} & d_{22} & d_{23} & d_{24} & d_{25} & d_{26} \\ d_{31} & d_{32} & d_{33} & d_{34} & d_{35} & d_{36} \end{bmatrix} \times \begin{pmatrix} E_x(\omega_1)E_x(\omega_2) \\ E_y(\omega_1)E_y(\omega_2) \\ E_z(\omega_1)E_z(\omega_2) \\ E_y(\omega_1)E_z(\omega_2) + E_z(\omega_1)E_y(\omega_2) \\ E_x(\omega_1)E_z(\omega_2) + E_z(\omega_1)E_x(\omega_2) \\ E_x(\omega_1)E_y(\omega_2) + E_y(\omega_1)E_x(\omega_2) \end{pmatrix} \tag{2.8}$$

with K being the degeneracy factor, which can take different values upon the represented second-order nonlinear process [45]. Therefore, the equation that represents SHG process in terms of d_{il} results,

$$\begin{pmatrix} P_x(2\omega) \\ P_y(2\omega) \\ P_z(2\omega) \end{pmatrix} = \varepsilon_0 \begin{bmatrix} d_{11} & d_{12} & d_{13} & d_{14} & d_{15} & d_{16} \\ d_{21} & d_{22} & d_{23} & d_{24} & d_{25} & d_{26} \\ d_{31} & d_{32} & d_{33} & d_{34} & d_{35} & d_{36} \end{bmatrix} \times \begin{pmatrix} E_x^2(\omega) \\ E_y^2(\omega) \\ E_z^2(\omega) \\ 2E_y(\omega)E_z(\omega) \\ 2E_x(\omega)E_z(\omega) \\ 2E_x(\omega)E_y(\omega) \end{pmatrix} \tag{2.9}$$

One of the symmetry properties present in some materials is the geometrical symmetry, inherent to the structural or spatial symmetry of the material. For those crystals that possess inversion of symmetry in their crystal structure (center of inversion), the nonlinear susceptibility, $\chi^{(2)}$, vanishes identically [53]. All materials with this characteristic are denominated *centrosymmetric* materials.

Second-order nonlinear process	SHG $\omega_1 = \omega_2 = \omega$	SFG $\omega_1 + \omega_2 = \omega_3$	DFG $\omega_1 = \omega_3 - \omega_2$	OPG $\omega_3 = \omega_1 + \omega_2$	Optical rectification $\omega_1 = \omega, \omega_2 = -\omega$
Degeneracy factor, K	1/2	1	1	1	1/2

Table 2.1: Degeneracy factor, K, value for each second-order nonlinear process.

Physically, the inversion of symmetry implies that under a change in the sign of the applied electric field $E(t)$, the sign of the induced polarization must also change. Therefore, the expression 2.3 should be replaced by,

$$-P_{NL}(t) = \chi^{(2)}\varepsilon_0(-E(t))^2 \qquad (2.10)$$

Simple calculation arises that,

$$-P_{NL}(t) = \chi^{(2)}\varepsilon_0 E(t)^2 \qquad (2.11)$$

So, by combining both expressions 2.10 and 2.11, $P_{NL}(t)$ must be equal to $-P_{NL}(t)$, which can only happen under the consideration that $P_{NL}(t)$ vanishes identically and, consequently, resulting in:

$$\chi^{(2)} = 0 \qquad (2.12)$$

Therefore, to exhibit second-order nonlinearity, the medium must be a *non-centrosymmetric* material. According with their point group symmetry classification, out of the 32 crystals groups classified and presented in Table 2.2 [54,55], just 20 of the 21 accentric class exhibit quadratic susceptibility [5].

Intuitively, the motion of an electron in a nonparabolic potential can be described for *centrosymmetric* versus *non-centrosymmetric* materials. Figure 2.2(a) shows an incident electromagnetic field of frequency ω. Media with linear response, Figure 2.2(b),

(a)

$E(t)$

(b)

$P(t)$

(c)

$P(t)$

(d)

$P(t)$
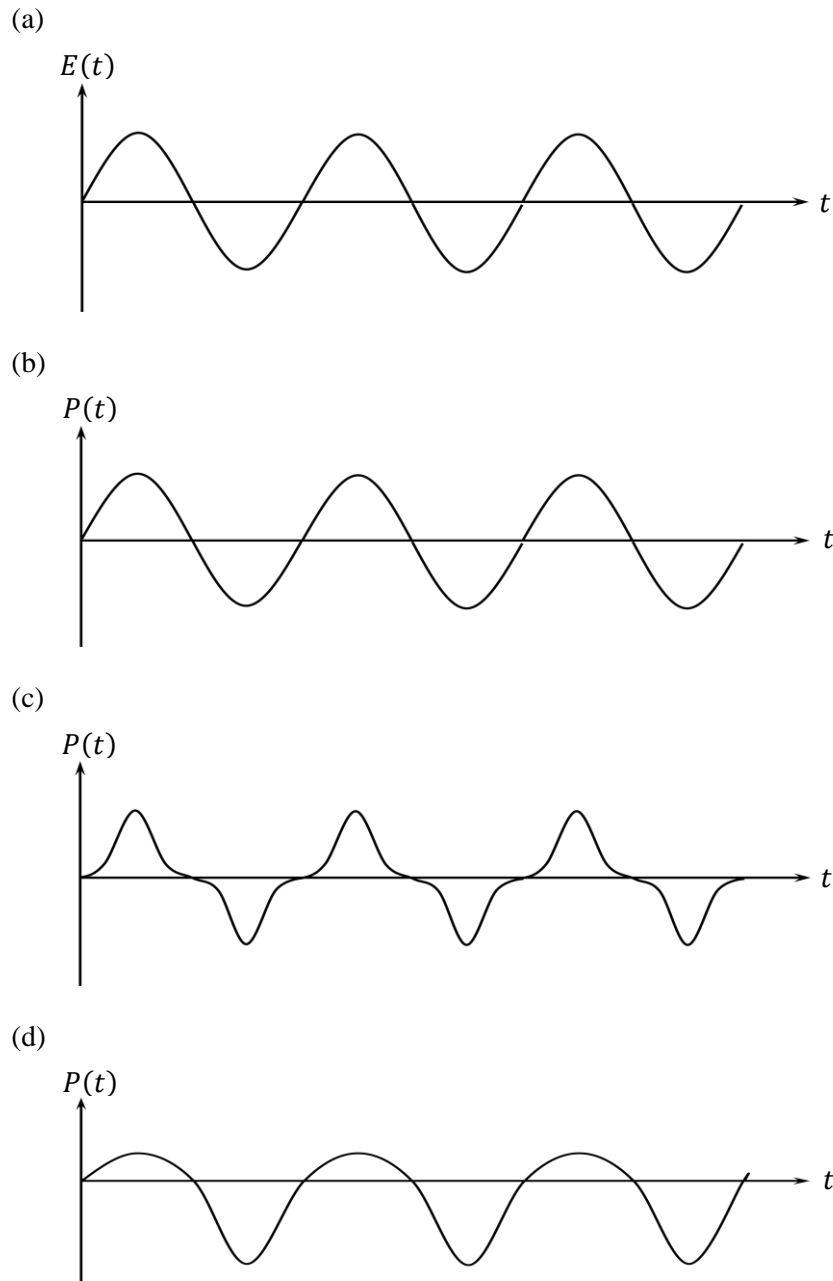
Figure 2.2: Waveforms associated with the atomic response when applying one field.
(a) represents the applied field; (b) represents the linear response; (c) the
nonlinear response of a centrosymmetric material; and (d) the nonlinear
response of a non-centrosymmetric material.

do not present any distortion on the waveform associated with the polarization of the medium. The waveform associated to the induced polarization on a *centrosymmetric* material, Figure 2.2(c), and on a *non-centrosymmetric* material, Figure 2.2(d), shows a qualitative difference between the waveforms. The polarization of the *centrosymmetric* material is zero time-averaged, whereas the *non-centrosymmetric* material responds in a different manner under an upward-direction electric field than to a downward-direction electric field, and then generating a polarization different to zero time-averaged.

Moreover, for small incident electromagnetic field strengths, *S*, the induced polarization displacement, *d*, presents a linear response, as shown in Figure 2.3(a). However, the dipole displacement becomes increasingly nonlinear at larger field strengths and the shape of its response depends on their point group symmetry classification as mentioned before. For centrosymmetric crystals, the response is symmetric with respect to the field direction, as shown in Figure 2.3(b), whereas for non-centrosymmetric crystals, Figure 2.3(c), the responses asymmetric [56].

2.3 Coupled-wave equations for second-order nonlinear processes

In-depth analysis of the nonlinear interaction between the involved fields within the nonlinear medium and the generation of new frequencies can be described using Maxwell's wave equations, as follows,

$$\nabla \times E = -\mu_0 \frac{\partial H}{\partial t} \tag{2.13}$$

$$\nabla \times H = \frac{\partial D}{\partial t} \tag{2.14}$$

(a)

(b)

(c)
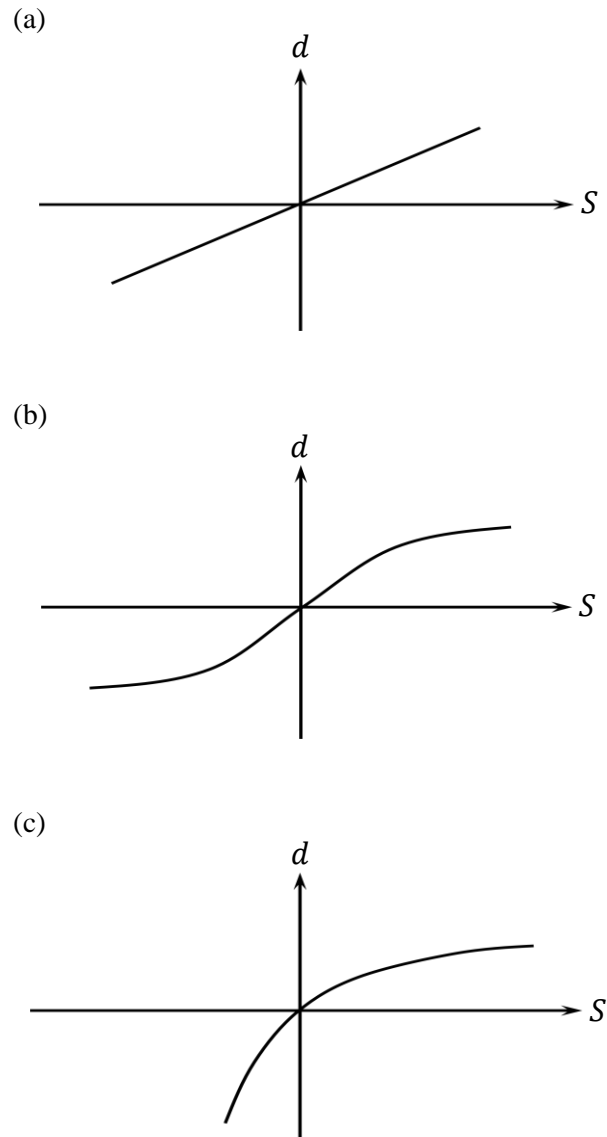
Figure 2.3: Dipole displacement response under different incident electromagnetic field strengths depending upon their symmetry group. (a) Represents the regime of linear optics under small incident electromagnetic fields; (b) the nonlinear response of centrosymmetric materials under strong incident electromagnetic fields; and (c) the nonlinear response of non-centrosymmetric materials under strong incident electromagnetic fields.

with H being the magnetic field strength, μ_0 the permeability of free space, and D the displacement vector defined as $D = \varepsilon_0 E + P$. Both equations 2.13 and 2.14 describe the light propagation within a non-magnetic and transparent ($J = 0$) nonlinear material. In other words, the driving polarizations generate in the nonlinear medium an electric field expressed by,

$$\nabla^2 E - \frac{1}{c^2}\frac{\partial^2 c}{\partial t^2} = \frac{1}{\varepsilon_0 c^2}\frac{\partial^2 P}{\partial t^2} \tag{2.15}$$

For a lossless, non-conducting, and nonmagnetic medium, an electric field, E, propagating along the x-axis and its associated polarization P are expressed as,

$$E_j(x,t) = E(x,\omega_j)e^{-i(k_j x - \omega_j t)} + c.c. \tag{2.16}$$

$$P_j(x,t) = P(x,\omega_j)e^{-i(k_j x - \omega_j t)} + c.c. \tag{2.17}$$

where $j = 1, 2, 3$ correspond to each of the three fields involved in the interaction, ω and k are the frequency and wave number associated with each of the interacting fields. The wave number, k, is given by,

$$k = \frac{n(\omega)\omega}{c} \tag{2.18}$$

where $n(\omega)$ corresponds to the refractive index of the nonlinear material at frequency ω expressed as,

$$n(\omega) = \sqrt{\frac{\varepsilon(\omega)}{\varepsilon_0}} \tag{2.19}$$

Each of the three fields involved in the second-order nonlinear process are interacting with each other along the medium. Mathematically, equations 2.16 and 2.17

Optic axis	Crystal class	Cento-symmetric point groups		Non-centrosymmetric point groups				
				Polar		Non-polar		
Biaxial	Triclinic	$\bar{1}$		1		None		
	Monoclinic	2 or m		2	m	None		
	Orthorhombic	mmm		mm2		222		
Uniaxial	Tetragonal	4 or m	4 or mmm	4	4mm	$\bar{4}$	$\bar{4}2m$	422
	Trigonal	$\bar{3}$	$\bar{3}m$	3	3m	32		
	Hexagonal	6 or m	6 or mmm	6	6mm	$\bar{6}$	$\bar{6}m2$	622
Optically isotropic	Cubid	m3	m3m	None		432	$\bar{3}m$	23
Total number		11 groups		10 groups		11 groups		

Table 2.2: Classification of crystal groups.

are expressed as a complex functions of the optical field. As the waves at three different frequencies are exchanging energy through $\chi^{(2)}$ process, as they propagate through the medium, the respective amplitudes will normally vary with position. Consequently, the complex field amplitudes are expressed as a function of *x*. Further, we assume that the amplitudes of the interacting fields vary slowly over distances comparable to a wavelength. This approximation – known as *slowly varying amplitude approximation* [45,57] – considerably simplifies our wave equations from second-order differential equations to first-order differential equations [5].

$$\left| \frac{\partial^2 E_j}{\partial x^2} \right| \ll \left| k_j \frac{\partial E_j}{\partial x} \right| \tag{2.20}$$

As a result, using the equations 2.3, 2.16, 2.17 and 2.18, we obtain,

$$\frac{\partial E_1}{\partial x} = \frac{i\omega_1^2 d_{eff}}{k_1 c^2} E_3 E_2^* e^{i\Delta kx} \tag{2.21a}$$

$$\frac{\partial E_2}{\partial x} = \frac{i\omega_2^2 d_{eff}}{k_2 c^2} E_3 E_1^* e^{i\Delta kx} \tag{2.21b}$$

$$\frac{\partial E_3}{\partial x} = \frac{i\omega_3^2 d_{eff}}{k_3 c^2} E_1 E_2 e^{-i\Delta kx} \tag{2.21c}$$

where E_1, E_2 and E_3 are the amplitudes of the electric fields of interacting waves, and d_{eff} is the *effective nonlinear coefficient*. The three basic equations imply that the amplitude of the newly produced waves is coupled to the incoming wave through the nonlinear coefficient, d_{eff}. These equations are commonly known as *coupled wave equations*. Physically, there is energy flow between the interacting fields at frequencies

ω_1 and ω_2 and the field at frequency ω_3. Similarly, the inverse process will also take place, i.e. processes where the newly generated frequency ω_3 mixes with one of the two incoming fields in a difference-frequency mixing process, such as $\omega_1 = \omega_3 - \omega_2$ [48]. Finally, $\Delta k = k_3 - k_2 - k_1$ is the wave *vector mismatch* between the interacting fields, also defining the *phase-matching* condition.

2.4 Phase-matching

Any nonlinear effect requires an efficient coupling between the interacting fields in the medium in order to undergo macroscopic amplification. Describing the coupled-wave equations (2.21a, 2.21b and 2.21c), we defined the wave vector mismatch $\Delta k = k_3 - k_2 - k_1$ between the interacting fields. Physically, Δk represents the mismatch in phase between the interacting fields when they propagate through the nonlinear medium. Only when there is perfect phase velocity matching between the interacting waves, we have,

$$\Delta k = 0 \tag{2.22}$$

The phase-velocity mismatch between the interacting fields could be offset and translate it into a macroscopic effect in a *non-centrosymmetric* nonlinear medium. In other words, this condition is necessary for achieving an efficient frequency conversion. This condition was proposed separately by J. A. Giordmaine [16] and P. D. Maker [25] in 1962, and it is known as *phase-matching* condition.

Physically, when the interacting fields at different frequencies travel through the medium, they experience different associated phase velocities due to the dispersion in the medium. In other words, the wave vector mismatch, Δk, is different from zero ($\Delta k \neq 0$). Under this condition, the interacting fields periodically step out of phase and interfere

constructively and destructively when they travel through the nonlinear medium, exchanging energy back and forth. As a result, the intensities of the generated fields experience oscillations along the propagation direction, as shown in Figure 2.4. Compensating phase mismatch can be done in several ways. The two most widely used methods to facilitate control over the phase mismatch are *birefringent phase-matching* (BPM) and *quasi-phase-matching* (QPM).

2.4.1 Birefringent phase-matching

This is the most common and widespread technique to offset the phase velocity mismatch. In this technique, the birefringence of a nonlinear crystal is exploited for achieving the phase-matching condition, $\Delta k = 0$. Due to the fact that the different interacting fields in the nonlinear process travel with different phase velocities inside the nonlinear material, the generated fields can phase-mismatch. Nevertheless, to obtain amplification, first it is necessary to ensure that the propagation of the interacting fields through the material is "synchronized" in a particular direction [56]. There are two properties inherent to the materials that generate differences in the refractive indices. Firstly, the dispersion of the material regarding the wavelength of the interacting field. As a result, different fields will experiment different refractive indices. Secondly, the property of certain optical crystals to generate different refractive indices depends on the polarization of the interacting fields. This property present in some crystal is called *birefringence*. Then, by a proper adjustment, when the interacting fields at different frequencies are differently polarized, their corresponding phase velocities can be adjusted, balancing both factors such that the index difference due to dispersion is
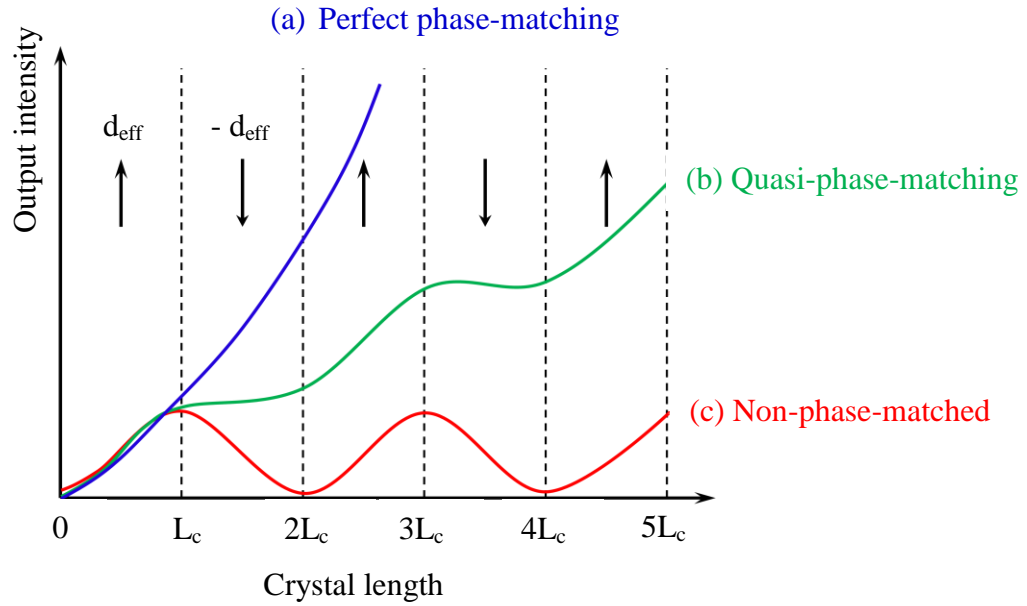
Figure 2.4: Illustration of (a) perfectly birefringent phase-matching ($\Delta k = 0$), (b) quasi-phase-matching and (c) non-phase-matching ($\Delta k \neq 0$) conditions in a second-order nonlinear process depending upon the crystal length and the output intensity incident in the nonlinear crystal.

compensated through the birefringence. This technique is known as *birefringent phase-matching* (BPM).

Going back to the inherent properties of the materials that exhibit birefringence – known as *birefringent materials* –, they can be classified into two distinct categories. Optically *uniaxial crystals*, in which $n_x = n_y \neq n_z$, and optically *biaxial crystals* in which $n_x \neq n_y \neq n_z$. When an incident field enters in an uniaxial crystal, light might be divided into two orthogonal polarizations. One experiences the same refractive index, independently of the direction of propagation in the medium. This is known as *ordinary index of refraction*, n_o, and this wave propagates with *ordinary polarization*
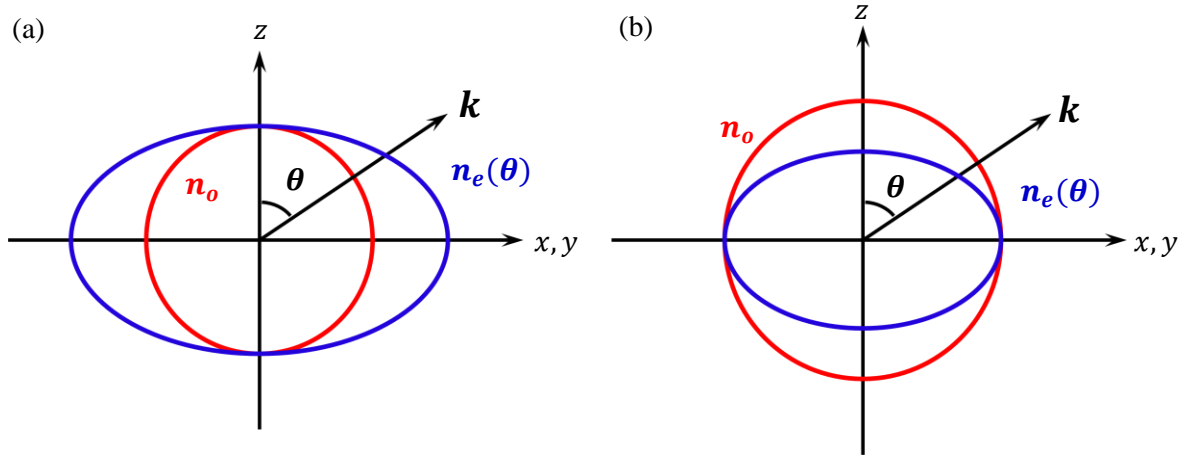
Figure 2.5: Normal index surface for positive (a) and negative (b) uniaxial crystals.

(*o*-polarization). However, the second polarization experiences a different refractive index depending upon the direction of propagation. This is called as *extraordinary index of refraction*, n_e, and this wave propagates with *extraordinary polarization* (*e*-polarization). The direction of propagation can be given by the angle, θ, relative to one of the principal axes of the medium, and it is given in [51] by the expression,

$$\frac{1}{n_e^2(\theta)} = \frac{cos^2(\theta)}{n_o^2} + \frac{sin^2(\theta)}{n_e^2} \qquad (2.23)$$

The difference between the ordinary and the extraordinary indices of refraction, $\Delta n = n_e - n_o$, provides information about the quantification of the birefringence. Depending of the value of Δn, birefringent materials are divided into positive ($\Delta n > 0$) and negative ($\Delta n < 0$), as shown in the Figure 2.5 for uniaxial crystals. Further, depending of the polarization of the interacting fields, BPM can be classified in two types, known as type-I and type-II. In type-I phase-matching, the driving fields present the same polarization and the generated field is orthogonally polarized compared to the driving fields (*ee*→*o* or *oo*→*e*), whereas in type-II phase-matching, the driving fields are
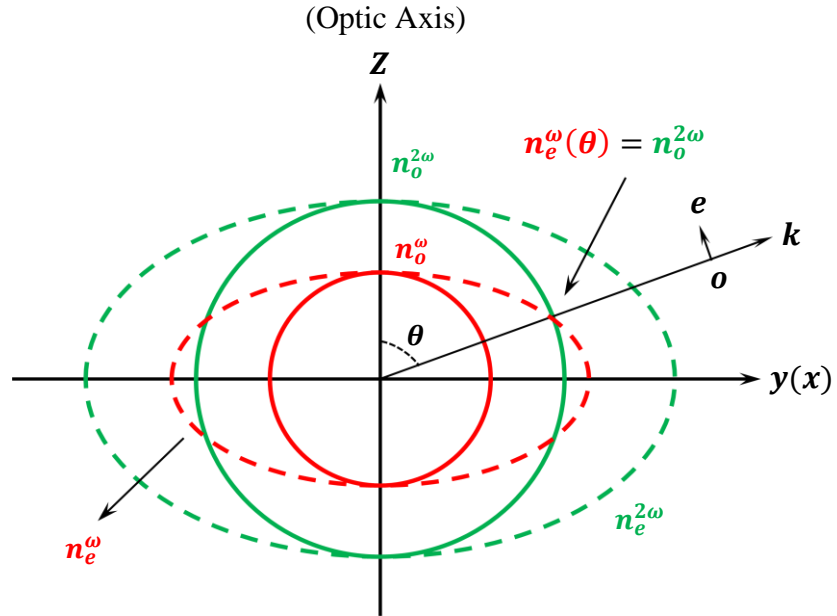
Figure 2.6: Illustration of perfect (type-I) phase-matching for SHG in case of extraordinary fundamental wave to generate ordinary second-harmonic wave.

orthogonally polarized (*eo→e* or *oe→o*). Figure. 2.6 shows the propagation direction at an angle of a positive uniaxial crystal, where the extraordinary index for the fundamental wave of frequency ω is equal to the ordinary index for second harmonic wave of frequency 2ω, thus birefringence compensating the dispersion and resulting in perfect type-I phase-matching [5].

Whenever the angle, θ, between the propagation direction and the optical axis has a value other than $\theta = 90°$, the Poynting vector, *S,* and the propagation vector, *k,* are not parallel for extraordinary rays. As a result, ordinary and extraordinary rays with parallel propagation vectors will diverge from each other as they propagate through the nonlinear medium. This phenomenon is known as *Poynting vector walk-off* or simply *spatial walk-off*. The expression of the walk-off angle, ρ, derives from,

$$tan \, \rho = -\frac{1}{n_e} \frac{dn_e}{d\theta} \tag{2.24}$$

Then, by combining 2.23 and 2.24, ρ arises as,

$$\rho = arctan \left(-\frac{1}{2} |n_e(\theta)|^2 \left(\frac{1}{n_e^2} - \frac{1}{n_o^2} \right) sin \, (2\theta) \right) \tag{2.25}$$

The walk-off reduces the synchronization between the interacting *e*-field and *o*-field within the nonlinear crystal, and then limiting the interaction length of the nonlinear material. This effective crystal length is called *aperture length* and it is given by,

$$l_a = \frac{\sqrt{\pi} w_0}{\rho} \tag{2.26}$$

where ω_0 is the input beam waist radius and ρ is the spatial walk-off angle.

Looking in the expression 2.26, it comes up rapidly that the aperture length and is linearly proportional to the input beam waist radius, w_0. Additionally, as it was stated at the beginning of this chapter, nonlinear optical processes require high intensity, and hence small beam waist. This implies that for long interaction lengths large spot sizes should be used, which is a contradiction. To overcome with this situation there is a special case that arises when the phase-matching angle turns out to be $\theta_{pm} = 90°$. This technique is possible in some materials at a particular temperature and it is known as *noncritical phase-matching* (NCPM). On the other hand, when $\theta_{pm} \neq 90°$ the phase-matching technique is called *critical phase-matching* (CPM). NCPM is advantageous for two reasons. First, it is less sensitive to beam divergence and walk-off, both of which can low the conversion efficiency. Second, the walk-off angle in this case is zero, which places less constrains on the beam size and the length of the nonlinear crystal [46].

Besides, in NCPM configuration, as the spatial walk-off vanishes, the nonlinear crystal length becomes the effective interaction length of the nonlinear optical process.

2.4.2 Quasi-phase-matching

In any birefringent material, even though we have the major problem of walk-off, it is still possible to fulfill both the energy conservation and phase-matching under certain conditions since the refractive index depends on the polarization of the interacting waves in the nonlinear medium. Additionally, for efficient nonlinear frequency conversion, it is necessary to use materials with a large nonlinear optical coefficient, d_{eff}. Facing this problem, J. A. Armstrong *et al.* [4] postulated in 1962 an alternative technique to birefringent phase-matching called *quasi-phase-matching* (QPM). The lack of momentum conservation in QPM is compensated by adding an artificial momentum originated from the local periodicity of the structure of the nonlinear material, as shown in Figure 2.7. An example of a negative birefringent nonlinear crystal is the well-known lihitum-niobate (LiNbO$_3$) [24,35]. Its largest nonlinear coefficient is d_{333}, which implies that the polarizations of the three interacting fields need to be in the same orientation. In birefringent phase-matching, this coefficient cannot be accessed either by type-I or type-II phase-matching. However this is possible using QPM.

In QPM, the nonlinear coefficient is modulated using a technique called *periodical poling* over the distance within the nonlinear crystal where the interacting fields are in phase. This is called the *coherence length* and is given by,

$$L_c = \frac{2\pi}{\Delta k} \tag{2.27}$$
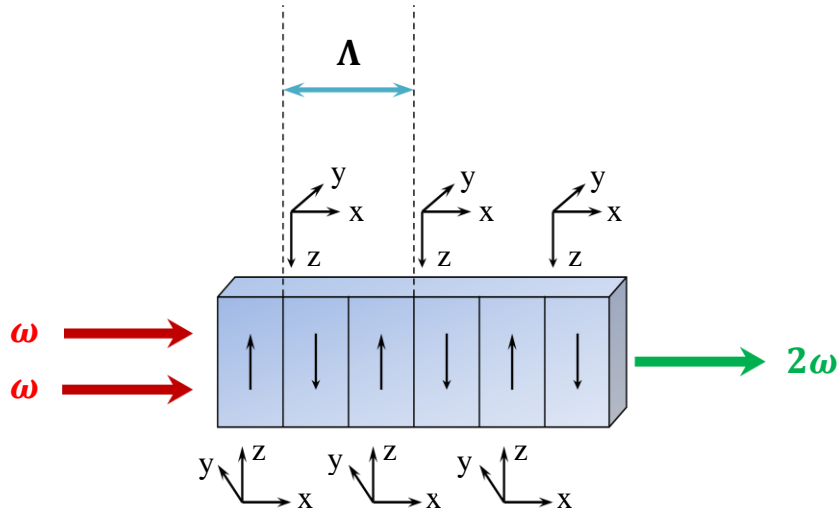
Figure 2.7: Representation of the SHG process in a QPM crystal with a schematic view

of the periodic inversion of the sign of the d_{eff} coefficient.

Using this technique, the nonlinear coefficient is modulated with a period twice the coherence length and switches its direction after the waves travel one coherence length within the nonlinear medium. Thus, the polarization is turned 180º after each coherence length, making the interacting fields propagate in phase along the propagation direction within the material, and thus enhancing the nonlinear effect. The introduction of the additional phase is adjusted by modulating the nonlinear coefficient of the medium with a period $\Lambda = 2l_c$. The quantity Λ it is called *grating period*.

QPM process is generally more efficient than birefringent phase-matching, and does not present a limitation regarding the length of the crystal. The nonlinear coefficient in the QPM process is given by the relation,

$$d = \frac{2d_{eff} \, sin \, (Dm\pi)}{m\pi} \tag{2.28}$$

where *m* is the order of the grating period and $D = l/\Lambda$ is called the *duty cycle*. Another

advantage is the QPM usually operates in the *non-critical phase-matching* regime. This implies that walk-off angle is zero as all the involved polarizations are the same. With the development of crystal growth technology of periodic poling since 90's periodically poled lithiun niobate – better known as PPLN – is widespread and the most used nonlinear material for various frequency conversion process throughout its transparency range from ~400 nm in the visible region to ~5000 nm in the mid IR region [48].

2.5 Second-harmonic generation

The first demonstration of optical SHG was led by P. A. Franken *et al.* irradiating a quartz crystal with a rubi laser [12] defined the beginning of the field of nonlinear optics. From that moment until today, the published work about SHG has become the topic of some of the most advanced device technology developments in society [46]. SHG, described schematically in Figure 2.1(a), is a second-order nonlinear process that involves two photons at a given frequency $\omega_1 = \omega_2 = \omega$, that interact in such a manner that generates an output photon at frequency 2ω.

There are many parameters to be consider in order to obtain efficient SHG, however the most obvious is the amount of power from the incident electromagnetic field at frequency ω that is converted into radiation at frequency 2ω. That is called *conversion efficiency*.

Following the plane-wave aproximation [58], in a first order approximation, it is assumend that in the frequency conversion process there is negligible depletion of the pump interacting electromagnetic field, that implies the conversion efficiency will be weak for constant pump powers [46]. Under these considerations [59], the expression of the conversion efficiency becomes

$$\eta_{2\omega} = \frac{P_{2\omega}(L)}{P_\omega(0)} = \eta_{norm_{2\omega}} \left[\frac{P_\omega L^2}{A} \right] sinc^2 \left(\frac{\Delta k L}{2} \right) \tag{2.29}$$

with

$$\eta_{norm_{2\omega}} = \frac{8\pi^2 d_{eff}^2}{c\varepsilon_0 \lambda_\omega^2 n_\omega^2 n_{2\omega}} \tag{2.30}$$

and, assuming BPM,

$$\Delta k = k_{2\omega} - k_\omega \tag{2.31}$$

where $\eta_{norm_{2\omega}}$ is the normalized conversion efficiency for a SHG process, A is the area of the beam calculated as $A = \pi \cdot w_0^2$ being w_0 de radious of the beam, or better called *beam waist*. $P_{2\omega}$ is the SHG power mesured at L, the length of the nonlinear crystal, in other words, the output power of the second-harmonic beam and P_ω is the power of the incident electromagnetic field. Besides, c is the velocity of light in vacuum, ε_0 is the permittivity of free space, λ_ω is the wavelength of the incident electromagnetic field, n_ω and $n_{2\omega}$ are the refractive indices of the incident (fundamental) and the generated (SH)
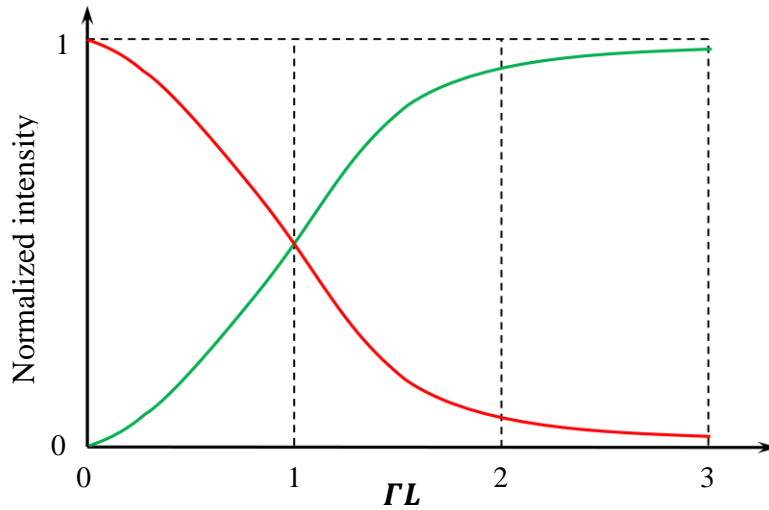
Figure 2.8: Second-harmonic and fundamental intensities as functions of ΓL for phase-matched SHG including pump depletion.

electromagnetic fields, respectively. In the expression 2.30, Δk is the wave-vector mismatch. Nevertheless, when we consider the incident beam is Gaussian – as in all the experiments presented this thesis –, the expression 2.30 requires a modification. Thus, the SHG conversion efficiency is given by [59]

$$\eta_{2\omega} = \frac{16\pi^2 d_{eff}^2 h}{c\varepsilon_0 \lambda_\omega^3 n_\omega^2 n_{2\omega}} LP_\omega \tag{2.32}$$

where h is the Boyd and Kleinman focusing parameter [60].

By in-depth analysis, the coupled-wave equations 2.21a, 2.21b and 2.21c for a single plane wavelength for the SHG process can be derived. This task was presented by J. A. Armstrong *et al*. [4], where the coupled-wave equations were derived and solved for SHG with zero input at the SH wavelength. These solutions are presented as follows,

$$\eta_{2\omega} = V_b^2 sn^2 \left(\frac{\Gamma L}{V_b} \middle| V_b^4 \right) \tag{2.33}$$

where sn is a Jacobi elliptic function [5,61,62], and

$$V_b = \left[\frac{\Delta S}{4} + \sqrt{1 + \left(\frac{\Delta S}{4} \right)^2} \right]^{-1} \tag{2.34}$$

being

$$\Delta S = \frac{\Delta k}{\Gamma} \tag{2.35}$$

and

$$\Gamma = \sqrt{\eta_{norm} I_\omega} \tag{2.36}$$

Nevertheless, with perfect phase-matching, the conversion efficiency becomes appreciable, making it impossible to ignore the depletion of the incident electromagnetic field, or pump [46]. Under this consideration, the expression 2.35 becomes [4,5,63].

$$\eta_{2\omega} = tanh^2(\Gamma L) \tag{2.37}$$

The above expression shows the SHG efficiency has a hyperbolic tangent-squared dependence on ΓL. The behavior of the *fundamental* beam and the SH beam intensities compensate each other in such a way that the fundamental beam is depleted asymptotically, approaching zero, while the SHG efficiency approaches 1 [46]. This behavior is illustrated in Figure 2.8.

This behavior is due to the fact that the fundamental beam intensity drives the nonlinear polarization, and then producing the SH. As the fundamental intensity is depleted, it becomes less effective in driving the nonlinearity [46].

2.6 Sum-frequency generation

In the section 2.2 we described the process of SFG as a second-order nonlinear process which involves two photons of frequency ω_1 and ω_2. They interact in such a manner that they generate an output photon at frequency $\omega_3 = \omega_1 + \omega_2$, according to the energy conservation principle. As it was previously mentioned, SHG is included as a degenerate case of SFG in which the two involved photons at frequencies ω_1 and ω_2 coincidentally are equal, that is $\omega_1 = \omega_2 = \omega$.

In correlation with what was stated in section 2.6 for the conversion efficiency in SHG processes, the same parameters must be consider for an efficient frequency conversion in case of SFG. Considering the above mentioned expressions for the SHG

conversion efficiency (2.30, 2.37), now these expressions are presented for the general case of a SFG process for both negligible and unegligible pump depletion. Thus, following the plane-wave aproximation, the conversion efficiency expresion with negligible pump depletion becomes [46],

$$\eta_{\omega_3} = \frac{P_{\omega_3}(L)}{P_{\omega_2}(0)} = \eta_{\omega_3\,norm} \left[\frac{P_{\omega_1} L^2}{A} \right] sinc^2 \left(\frac{\Delta k L}{2} \right) \tag{2.38}$$

with

$$\eta_{\omega_3\,norm} = \frac{8\pi^2 d_{eff}^2}{c\varepsilon_0 \lambda_{\omega_3}^2 n_{\omega_1} n_{\omega_2} n_{\omega_3}} \tag{2.39}$$

and

$$\Delta k = k_{\omega_3} - k_{\omega_1} - k_{\omega_2} \tag{2.40}$$

where $\eta_{\omega_3\,norm}$ is the normalized SFG *conversion efficiency*, P_{ω_3} is the SFG power mesured at L, and P_{ω_1} and P_{ω_2} are the power of the incident beams at frequencies ω_1 and ω_2 respectively. Besides, λ_{ω_3} is the corresponding wavelength of the generated beam at frequency ω_3, and the corresponding indices of refraction of all the interacting waves are represented by n_{ω_1}, n_{ω_2} and n_{ω_3}. The expression 2.31 also transforms into the general case 2.36 for arbitrary frequencies ω_1, ω_2 and ω_3. A corresponding treatment of the previous expresions described for SHG in the previous section can be found for SFG in the literature [4,45,46]. For perfect phase-matching, it becomes necessary to consider the pump depletion of the incident beam. Therefore, the expression 2.36 transforms into the general case,

$$\eta_{\omega_3} = \frac{\lambda_{\omega_2}}{\lambda_{\omega_3}} sn^2(\Gamma, \gamma) \tag{2.41}$$

with

$$\Gamma = \sqrt{\eta_{\omega_3 norm} I_{\omega_1}} \qquad (2.42)$$

and

$$\gamma = \sqrt{\frac{\lambda_{\omega_2} P_{\omega_2}(0)}{\lambda_{\omega_1} P_{\omega_1}(0)}} \qquad (2.43)$$

where γ is the *modulus*, an useful parameter for a better description of the SFG in terms of the Jacobi elliptic sine function. The tabulated values for the Jacobi elliptic sine function can be found in the Reference [64]. The modulus γ varies from 0 to 1 providing $\gamma < 0.1$, $sn(\Gamma, \gamma) \approx sin(\Gamma)$ while as $\gamma \to 1$, $sn(\Gamma, \gamma) \approx tanh(\Gamma)$, which is the value described in the expression 2.36 for SHG.

There are various parameters that are important for efficient SFG and, therefore, for any SHG process. These include choice of a crystal with high nonlinear optical coefficient, optimum length of the nonlinear crystal, angular, spectral and temperature acceptance bandwidth as well, as other parameters described in following sections.

2.7 Phase-matching considerations

When designing any experiment involving a second-order nonlinear process, the underlying principle is the maximization of the *gain* through a suitable choice of the nonlinear medium according to its intrinsic properties, such as high nonlinear optical coefficient, damage threshold or transparency range. Other important parameters, such as the election of the optimum length of the nonlinear crystal, the correct pump wavelength as well as an optimum focusing must be considered for an optimum frequency conversion process. Each of the above mentioned parameters play a crucial role for an efficient and

successful generation of any experiment involving second-order nonlinear processes operating at optimum performance [48]. These parameters are presented below.

Acceptance bandwidths

In any nonlinear frequency conversion process, the optimum choice of the nonlinear crystal length should ensure wide angular, spectral and temperature acceptance bandwidths, which help achieve efficient conversion. Here are presented the expressions for SHG and the expressions for the general case given in Reference [66]. Thus, the *spectral acceptance bandwidth* expression is given by [5],

$$\Delta\lambda = \frac{0.4429\lambda_\omega}{L}\left|\frac{n_{2\omega} - n_\omega}{\lambda_\omega} + \frac{\partial n_\omega}{\partial\lambda_\omega} - \frac{1}{2}\frac{\partial n_{2\omega}}{\partial\lambda_{2\omega}}\right|^{-1} \tag{2.44}$$

where *L* is the length of the nonlinear crystal while the *temperature acceptance bandwidth* expression is given by:

$$\Delta T = \frac{0.4429\lambda_\omega}{L}\left|\frac{\partial n_{2\omega}}{\partial T} - \frac{\partial n_\omega}{\partial T} - \alpha(n_{2\omega} - n_\omega)\right|^{-1} \tag{2.45}$$

where α is the linear thermal expansion coefficient of the crystal. As an example, the acceptance bandwidths for a SHG process with type-I interaction (*ee→o*) in the *yz*-plane using a 10-mm-long BIBO crystal are shown below. Using the Sellmeier equations of Reference [35] the spectral and angular acceptance bandwidths are calculated to be $\Delta\lambda$ = 0.97 nm and $\Delta\theta$ = 1.031 mrad·cm (Figure 2.9 and Figure 2.10 respectively).

Material requirements

The search for optimum nonlinear materials addressed to different parametric processes has resulted in the development of numerous nonlinear crystals. Some, but not all, are
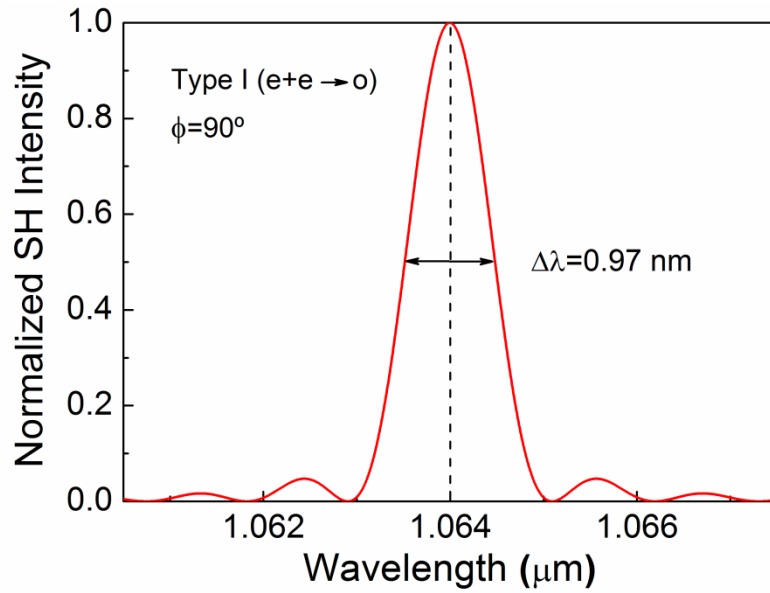
Figure 2.9: Spectral acceptance bandwidths of a 10-mm-long BIBO nonlinear crystal
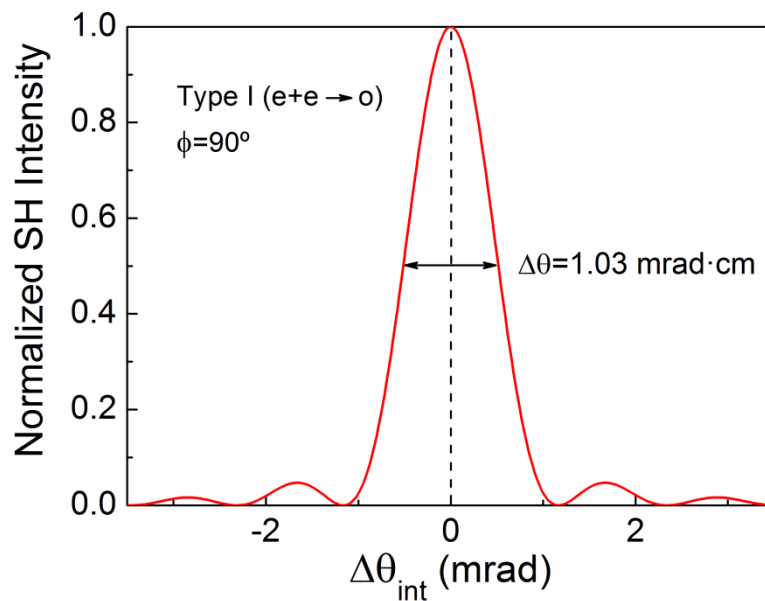
for SHG with type-I interaction (*ee→o*) in the *yz*-plane.

Figure 2.10: Angular acceptance bandwidths of a 10-mm-long BIBO nonlinear crystal for

SHG with type-I interaction (*ee→o*) in the *yz*-plane.

54

well described in [67] in the process of selection of the ideal material. There are several important parameters that have to be taken into consideration when selecting the nonlinear crystal for any frequency conversion process. A correct election in the choice of the material should include: (a) non-centrosymmetry; (b) optical anisotropy; (c) wide transparency range within the operating wavelength; (d) sufficient birefringence; (e) large variation of refractive indices with temperature, angle, pressure or electric field according with the necessities; (f) large nonlinearity – the larger, the better; (g) low spatial walk-off; (h) phase matchability, preferably NCPM; (i) high damage threshold; (j) good mechanical, chemical and thermal properties; and (k) availability of large crystals in high optical quality with low transmission losses.

However, the large number of simultaneous requirements that need to be accomplished restricts the number of potentially useful crystals to a few. Last, but not least, another important parameter determining the large nonlinearity is the nonlinear *figure-of-merit* (FOM) defined as [5],

$$FOM = \frac{d_{eff}}{\sqrt{n_{\omega_1} n_{\omega_2} n_{\omega_3}}} \qquad (2.46)$$

which is important to a assess the nonlinear efficiency of the material. The *FOM* is directly proportional to the d_{eff}, which implies that for a larger d_{eff} the greater the *FOM*, and hence the larger intrinsic nonlinear efficiency of the material.

3 High-power, picosecond ultraviolet source at 355 nm based on BiB$_3$O$_6$

This chapter constitutes the following publication:

1. *Stable, high-power, Yb-fiber-based, picosecond ultraviolet generation at 355 nm using BiB$_3$O$_6$*

   S. Chaitanya Kumar, **E. Sánchez Bautista** and M. Ebrahim Zadeh.

   Optics Letters, **40**(3), 403-406 (2015).

3.1 Motivation

Stable, high-power, picosecond UV sources are of great interest for applications ranging from laser micro-machining [72] and ultrafast laser patterning [73] to medical diagnostics and pumping optical parametric oscillators [74]. For many years, the development of such ultrafast sources has relied almost entirely on nonlinear optical techniques based on THG (~355 nm) and fourth-harmonic generation (FHG) (~266 nm) of widely established mode-locked Nd/Yb-doped solid-state lasers at ~1064 nm. The rapid advances in fiber laser technology in recent years, however, have paved the way for

the replacement of bulky, water-cooled, mode-locked solid-state lasers with compact, air-cooled, ultrafast Yb-fiber lasers at ~1064 nm. With the availability of multiwatt average powers, and the potential for further power scaling, the exploitation of mode-locked Yb-fiber lasers offers great promise for the realization of efficient and high-power picosecond UV sources in more practical designs by deploying THG and FHG schemes. On the other hand, to fully exploit the advantages of fiber lasers with regard to a compact architecture, simplicity, and portability, it would also be crucial to deploy the most direct nonlinear techniques for UV generation in order to preserve those important merits. To this end, single-pass conversion schemes offer the most effective approach to achieve this goal. Recently it has been demonstrated the viability of such single-pass schemes in combination with cw and mode-locked Yb-fiber lasers for efficient generation of high-power cw radiation in the green and UV [40], and high-average-power picosecond pulses in the green [39] as well as a fiber-based femtosecond green source [75].

At the same time, a critical factor in the attainment of highest nonlinear conversion efficiency and output power is the choice of suitable nonlinear materials. For UV generation, this choice is particularly limited, and especially challenging when low-intensity picosecond pulses at high repetition rates are involved. In addition to a wide transparency in the UV, of paramount importance are a sufficiently high effective nonlinearity, low spatial walk-off, high optical damage threshold, low transmission loss and high optical quality, as well as chemical and thermal stability. In the absence of suitable periodically poled nonlinear materials offering ready availability, wide transparency, and first-order quasi-phase-matching in the UV, borate-based birefringent crystals have proved the most viable candidates for UV generation. In particular, due to broad transparency and high damage threshold,

BBO and LBO have become materials of choice for the development of high-energy pulsed UV sources, despite their relatively low optical nonlinearity of ~2 pm/V and ~0.7 pm/V, respectively.

On the other hand, the birefringent nonlinear crystal, BIBO, also belonging to the borate family of materials, possesses unique linear and nonlinear optical properties for frequency conversion from the IR to the visible and UV [36,39,40,75-78]. As a biaxial crystal, it offers highly flexible phase-matching characteristics for various nonlinear interactions in the three optical planes. It has the largest optical nonlinearity of all borate crystals (~3.9 pm/V) [76], with high bulk UV damage threshold (50 MW/cm^2) [77] and low UV absorption coefficient ($\alpha_{UV} < 0.02$ cm^{-1}) [36], making it a promising candidate for frequency conversion into the UV. Despite a longer UV absorption edge (~280 nm) compared to BBO (~180 nm) and LBO (~160 nm), BIBO can be phase-matched in the optical *yz*-plane under type-I (*ee→o*) interaction at room temperature using SFG of IR and green radiation, to provide UV output at 355 nm with high efficiency. This makes BIBO highly attractive for efficient frequency conversion of low-energy, high-repetition-rate, picosecond pulses into the UV [78]. The phase-matching properties of some promising nonlinear materials for UV generation are listed in Table 3.1.

In this chapter, we demonstrate such a source using BIBO as the nonlinear crystal. Here, the primary pump source is a picosecond Yb-fiber laser (Fianium FP1060-20) providing up to 20 W of output power at 1064 nm at 80-MHz repetition rate. The compact, high-power and stable UV source is based on a novel multicrystal scheme comprising two stages, both involving single-pass conversion processes. The first one involves single-pass SHG followed by the second stage that involves single-pass SFG. Figure 3.1 shows the scheme of the experiment with the two stages. By looking at the

Crystal	UV Cutoff (nm)	Phase-matching	Type / Interaction	P-M angle	d_{eff} (pm/V)	FOM (d_{eff}^2/n^3)	α_{UV} (cm^{-1}) @ 355 nm	$\Delta\rho$ (mrad)
LBO	~160	Birefringent	Type-I ($oo{\to}e$)	θ=90º, φ=37.2º	0.7	0.12	0.003	0
BBO	~180	Birefringent	Type-I ($oo{\to}e$)	θ=31º	1.8	0.87	<0.1	0
BIBO	~280	Birefringent	Type-I ($ee{\to}o$)	θ=146.3º, φ=90º	3.9	2.42	0.02 (o-ray)	3.23

Table 3.1: Phase-matching properties of some nonlinear crystals for UV generation through SFG.

$$\omega + \omega = 2\omega \qquad \omega + 2\omega = 3\omega$$

Picosecond Yb-fiber laser → Crystal 1 (BIBO or LBO) SHG type-I (eoo) → BIBO SFG type-I (eeo) → 355 nm
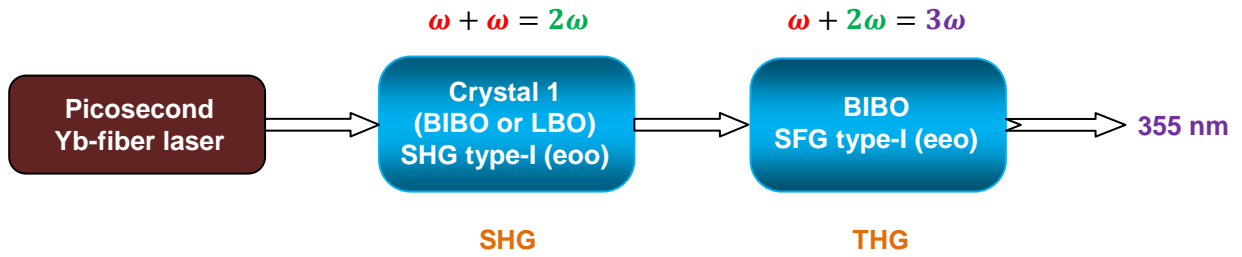
SHG   THG

Figure 3.1: Schematic view of the nonlinear processes in the experiment. "Crystal-1" represents a BIBO crystal (all-BIBO configuration) or a LBO crystal (LBO-BIBO configuration).

first stage, it is written "Crystal-1". This is because two different crystals were used in the this position in order to generate SHG obtaining different results. First, we used a BIBO crystal and, later, we used an LBO crystal for the same purpose. From now on, we will refer to them as *all-BIBO configuration* or *LBO-BIBO configuration*. In both configurations the second stage has a BIBO crystal.

This chapter is divided into two sections, one for the all-BIBO configuration, and the other for the LBO-BIBO configuration.

In the *all-BIBO* section, "Crystal-1" is a 10-mm-long BIBO crystal cut at $\theta = 168.9°$ ($\phi = 90°$) for type-I ($ee \rightarrow o$) SHG to 532 nm. On it, the fundamental beam at 1064 nm is focused to a beam waist radius of $w_{01} \sim 42\ \mu$m, constituting the first conversion stage. In the second stage, the undepleted fundamental and generated SH are collimated and refocused using two concave mirrors ($r_1 = 150$ mm, $r_2 = 200$ mm) into an elliptic beam waist radius of $w_{02} \sim 54 \times 86\ \mu$m in a second 10-mm-long BIBO crystal cut at $\theta = 146.2°$ ($\phi = 90°$) for type-I ($ee \rightarrow o$) SFG into the UV. Overall, the all-BIBO, picosecond UV source provides up to 164 mW of output power at 80 MHz repetition-rate with excellent long-term passive stability better than 0.6% rms over 6 hours and high spatial beam quality. The source also simultaneously generates 4.9 W of picosecond

green power at 532 nm with a passive power stability of 0.4% rms over 6 hours in high spatial beam quality.

In the *LBO-BIBO* section, "Crystal-1" is a 30-mm-long LBO cut at $\theta = 90°$ ($\varphi = 0°$) for type-I ($oo \rightarrow e$) NCPM in the optical *xy*-plane at 148.2 °C performing single-pass SHG. Up to 9.1 W of average green power at 532 nm is obtained at a single-pass SHG efficiency of 54%. The generated green pulses have duration of 16.2 ps at a repetition rate of 79.5 MHz, with a passive power stability better than 0.5% rms and a pointing stability <12 μrad over 1 hour, in high beam quality. As in the previous section, the green radiation is sum-frequency-mixed with the fundamental in a 10-mm-long BIBO crystal, providing as much as 1.2 W of average UV power, at an IR-to-UV conversion efficiency of 7.2%, with a passive power stability better than 0.4% rms over 3 hours and a pointing stability <45 μrad over 1 hour, in TEM_{00} spatial profile.

3.2 Design and optimization of the focusing

In order to optimize the efficiency of our nonlinear process, we used a focusing parameter [60].

$$\xi = \frac{l}{b} \tag{3.1}$$

where l is the length of the nonlinear crystal and b is the *confocal parameter* of the pump, defined as,

$$b = \frac{2\pi w_0^2 n}{\lambda} \tag{3.2}$$

being,

$$k = \frac{2\pi n}{\lambda} \tag{3.3}$$

where n is the length of the nonlinear crystal, λ is the wavelength and w_0^2 is the waist radius of the pump beam inside the nonlinear crystal. Then, by merging the expressions 3.2 and 3.3 results,

$$b = kw_o^2 \tag{3.4}$$

which is common form of the expression for the confocal parameter. In all the crystals in this experiment, the pump beam is confocally focused at the centre of the nonlinear crystal to a beam waist radius such that it ensures an optimum overlap of the interacting waves at the center of the crystal.

3.3 Experimental setup

The schematic of the experimental setup is shown in Figure 3.2. The fundamental source is a mode-locked Yb-fiber laser (Fianium FP1060-20) delivering up to 20 W of average power at 1064 nm in pulses of 20 ps duration at 79.5 MHz repetition rate. The laser has a double-peaked spectrum with a full-width at half-maximum (FWHM) bandwidth of ~1.4 nm. The output power is adjusted using a combination of a half-wave plate and a polarizing beam-splitter cube. A second half-wave plate is used to obtain the required polarization for phase-matching in the nonlinear crystals. The experiment was realized using two different crystals in the "Crystal-1" position. First, we used a 10-mm-long BIBO crystal cut at $\theta = 168.9°$ ($\varphi = 90°$) for type-I ($ee \rightarrow o$) phase-matching in the yz-plane for SHG of the 1064 nm. After, we used a 30-mm-long LBO crystal with an aperture of 3×4 mm^2 cut at $\theta = 90°$ ($\varphi = 0°$) for type-I ($oo \rightarrow e$) NCPM in the optical xy-plane at $T_{pm} = 148.2$ °C also for SHG of the 1064 nm.

The SFG stage comprises of a 10-mm-long, 3-mm-wide and 3-mm-thick BIBO
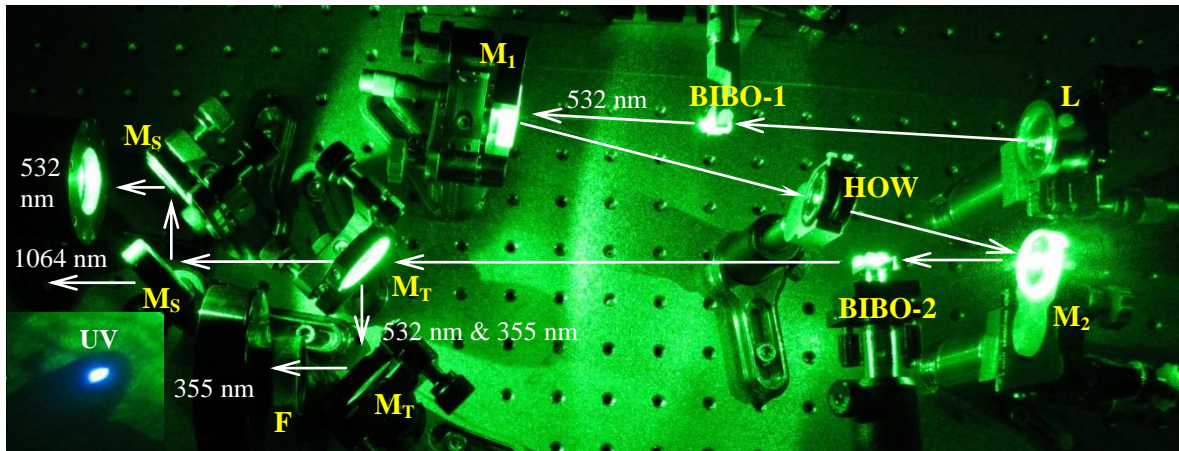
Figure 3.2: Picture of the setup and of the UV beam.

crystal, cut at $\theta = 146.3°$ ($\varphi = 90°$) in the optical *yz*-plane for type-I (*ee→o*) sum-frequency mixing of 1064 nm and 532 nm to generate UV output at 354.7 nm. In this interaction, both fundamental and SH are extraordinary, while the SFG output is ordinary. In order to achieve identical polarizations at fundamental as well as SH beam for phase-matching in the SFG stage, we used a pair of dual-wavelength wave-plates, or simply, high-order wave-plates (HOW), which simultaneously provide quarter-wave rotation at 532 nm and half-wave rotation at 1064 nm. The BIBO crystal in the SFG stage is phase-matched by angular interrogation at room temperature. The end-faces of both crystals are antireflection (AR)-coated ($R < 0.1\%$) at 1064 and 532 nm, while the BIBO faces are also AR-coated at 354.7 nm.

The fundamental beam is focused at the center of the crystal-1 in order to provide SHG output at 532 nm. The generated SH beam and the undepleted fundamental are then refocused into the BIBO crystal in the SFG stage. For this purpose, two plano-concave mirrors, M_1 and M_2, are used to provide an elliptic beam waist inside the BIBO crystal. Both mirrors are coated for high reflectivity ($R > 99\%$) at 1064 nm and 532 nm, and mounted on translation stages, so as to adjust the inter-crystal spacing between the SHG

and SFG stage. The radius of curvature of M_1 and M_2 is $r = 150$ mm and 200 mm, respectively. The generated UV radiation is then separated from the fundamental and SH beams using dichroic mirrors, M_T ($R > 99\%$ at 355 nm, $T > 99\%$ at 1064 nm and 532 nm), and further filtered using FGUV11 glass, F, while mirrors, M_S ($R > 99\%$ at 532 nm, $T > 99\%$ at 1064 nm), separate the SH wavelength from the fundamental.

3.4 All-BIBO section: Single-pass, picosecond, all-BIBO ultraviolet source
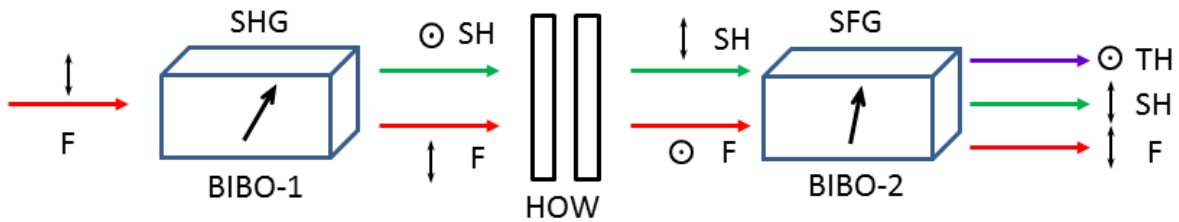

Figure 3.3: Schematic view of the all-BIBO configuration.

In this section we present a full study of both the SHG and the SFG processes that occur in both crystals of our experimental setup. In order to support our exposition, we present the theoretical calculations necessary for a successful reproduction of this experiment as well as an ideal optimization of the system. After the full characterization of SHG in BIBO presented in 2004 in [79], here a characterization of SFG in BIBO is also presented. Moreover, we present all the experimental results.

As previously mentioned, in the *all-BIBO* section, we present a picosecond UV source composed by two consecutive BIBO crystals as shown in Figure 3.3, providing up to 164 mW of output power at 80 MHz repetition-rate with excellent long-term passive stability better than 0.6% rms over 6 hours and high spatial beam quality. The source also generates 4.9 W of picosecond green power at 532 nm with a passive power stability
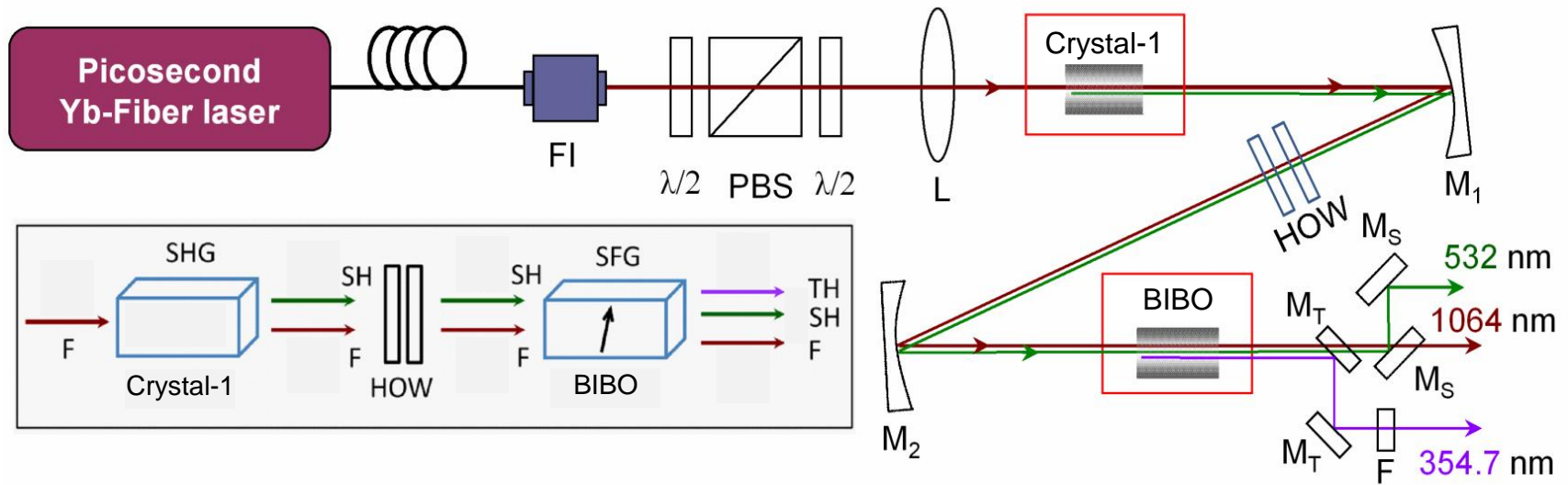
Figure 3.4: Schematic of the experimental setup for single-pass SHG and THG. $\lambda/2$: half-wave-plate; *PBS*: polarizing beam-splitter; *L*: lens; *HOW*: high-order wave-plates; $M_{1,2}$: plano-concave mirrors; M_T: dichroic mirrors. Inset: schematic of the action of the high-order wave-plates (HOW) providing simultaneous quarter-wave rotation at 532 nm and half-wave rotation at 1064 nm.

of 0.4% rms over 6 hours in high spatial beam quality.

Here, as it is shown in Figure 3.4, "Crystal-1" is a 10-mm-long BIBO crystal cut at $\theta = 168.9°$ ($\phi = 90°$) for type-I ($ee{\rightarrow}o$) SHG constituting the first conversion stage. The fundamental beam at 1064 nm is focused to a waist radius, $w_{01} \sim 42$ μm into the first BIBO crystal, corresponding to a focusing parameter of $\xi \sim 0.53$ [60]. In the second stage, the undepleted fundamental and generated SH are collimated and refocused using two concave mirrors ($r_1 = 150$ mm, $r_2 = 200$ mm) into an elliptic beam waist radius of $w_{02} \sim 54 \times 86$ μm in a second 10-mm-long BIBO crystal cut at $\theta = 146.2°$ ($\phi = 90°$) for type-I ($ee{\rightarrow}o$) SFG into the UV.

3.4.1 Second-harmonic generation using BIBO crystal

The generation of ultrashort pulses in the visible spectrum, particularly in the green centered at 532 nm, presents great interest in potential scientific and technological applications [80]. Due to the absence of suitable laser gain media, the development of high-power green sources over the past 50 years has relied almost exclusively on a variety of SHG nonlinear materials, both birefringent [39,81-87] and QPM [88] materials.

Some QPM nonlinear crystals such us periodically poled $KTiOPO_4$ and MgO-doped stoichiometric $LiTaO_3$ have been deployed in a large number of experiments in the past, performing single-pass SHG to generate high-power single-frequency green radiation both in cw and pulsed regime [89-91]. They present high nonlinear coefficient ($d_{eff} \sim 9$ pm/V) as well as long interaction length, but they also a narrow spectral acceptance bandwidth for SHG (~ 0.25 nm·cm), precluding their use in the ultrafast regime, where large spectral bandwidths are involved [39]. On the other hand, some birefringent nonlinear crystals, such as BBO and LBO present wide transmission range

into the near visible and UV and high optical damage threshold as well. However, the relatively low nonlinear optical coefficients (~2 pm/V and ~0.7 pm/V, respectively) of these crystals make the use of BBO and LBO to be addressed to applications involving high pulse energies or with a limited phase-matching geometries within the crystal. Considering these circumstances, the birefringent crystal BIBO presents unique nonlinear optical properties such as relatively large effective nonlinearity in the *yz*-plane ($d_{\text{eff}} > 3$ pm/V), wide transparency from the UV to near-IR, flexible phase-matching properties, high optical damage tolerance, ready availability, and low cost [3].

By using the Sellmeier equations reported in [35], here we present the theoretical calculations of the phase-matching angle [79] and the acceptance bandwidths used in the realization of this experiment. In the *yz*-plane, type-I (*ee→o*) interaction phase-matching can be reached for incidence angles between $\theta \sim 90°$ and 180°, over a fundamental wavelength range from 0.542 to 1.18 μm.
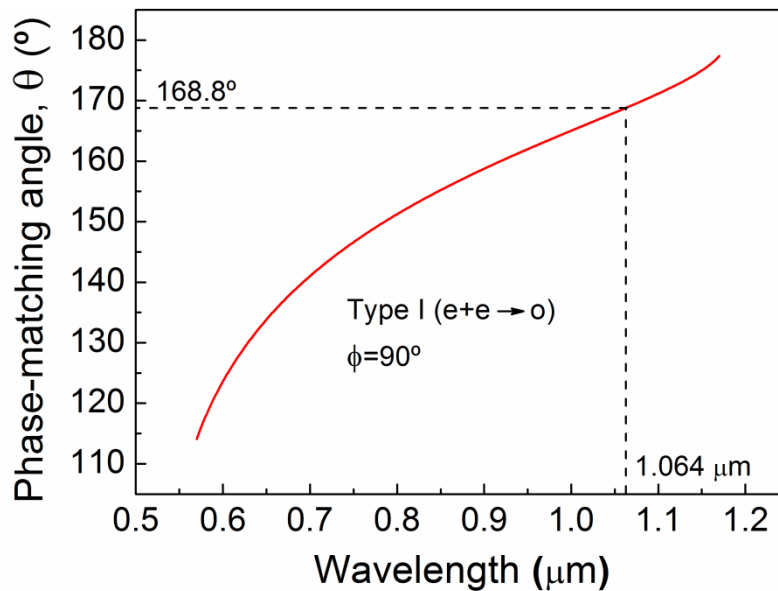

Figure 3.5: Phase-matching curve for SHG for type-I (*ee→o*) interaction in the *yz*-plane.

68

3.4.1.1 Phase-matching

Figure 3.5 shows the phase-matching curve for a pump wavelength from 0.57 to 1.16 μm, presenting a corresponding phase-matching angle from $\theta \sim 115^{\circ}$ to 176°. Of particular interest is the value corresponding to 1.064 μm, an easy reachable wavelength for numerous lasers commercially available. In this respect, for SHG of fundamental radiation near 1 μm, BIBO offers wide spectral and angular acceptance bandwidths with low special walk-off. At 1.064 μm, BIBO crystal presents a phase-matching angle of $\theta_{pm} = 168.9^{\circ}$ for SHG, which has been used during this experiment.

3.4.1.2 Acceptance bandwidths

In order to achieve efficient SHG, we first studied the phase-matching properties of the crystal evaluating the angular and spectral acceptance bandwidths. The variation of the SH output with the angle at a fixed fundamental wavelength determines the angular acceptance bandwidth of the nonlinear crystal and provides information about the uniformity of phase-matching inside of the crystal of the interacting waves. The angular acceptance bandwidth curve theoretically calculated is shown in Figure 3.6. The $sinc^2$ curve has a FWHM of $\Delta\theta = 1.03$ mrad·cm at a fixed wavelength of 1.064 μm. Moreover, it becomes very important to consider also the evolution of the spectral acceptance bandwidths, particularly in the high-repetition rate regime for materials with large spectral bandwidths. This parameter can have a dramatic effect on the second-harmonic power and efficiency, as well as the output pulse duration [79]. The spectral acceptance bandwidth curve was also numerically calculated and shown in Figure 3.7. It presents a FWHM of $\Delta\lambda = 0.97$ nm at a phase-matching angle of $\theta_{pm} = 168.8^{\circ}$.

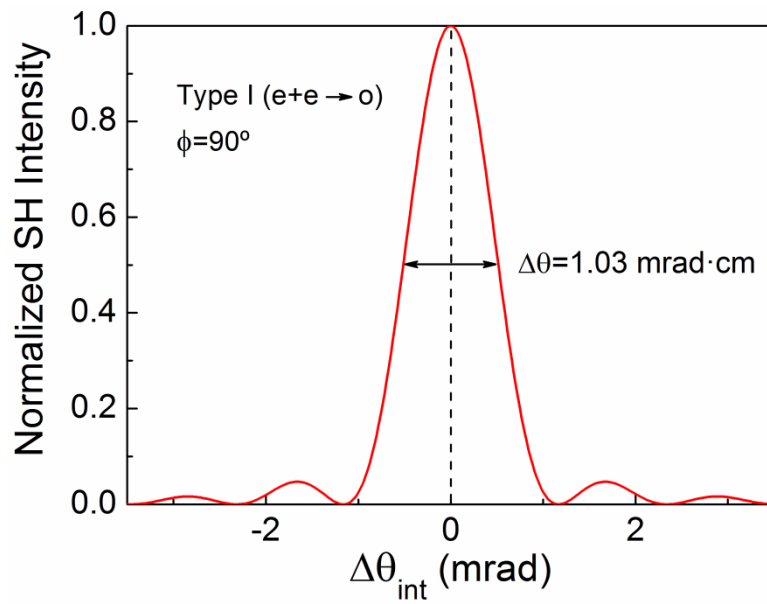Figure 3.6: Angular acceptance bandwidth for SHG for type-I (*ee→o*) interaction in the

yz-plane.
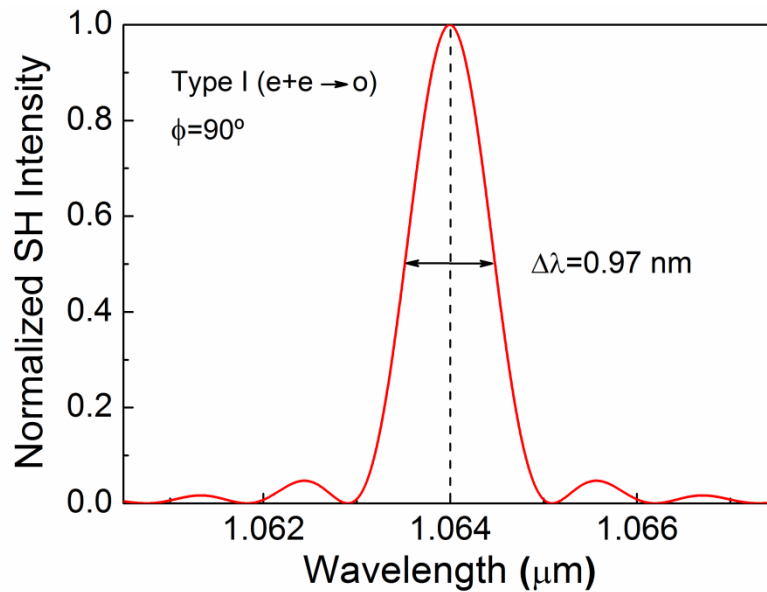

Figure 3.7: Spectral acceptance bandwidth for SHG for type-I (*ee→o*) in the *yz*-plane.
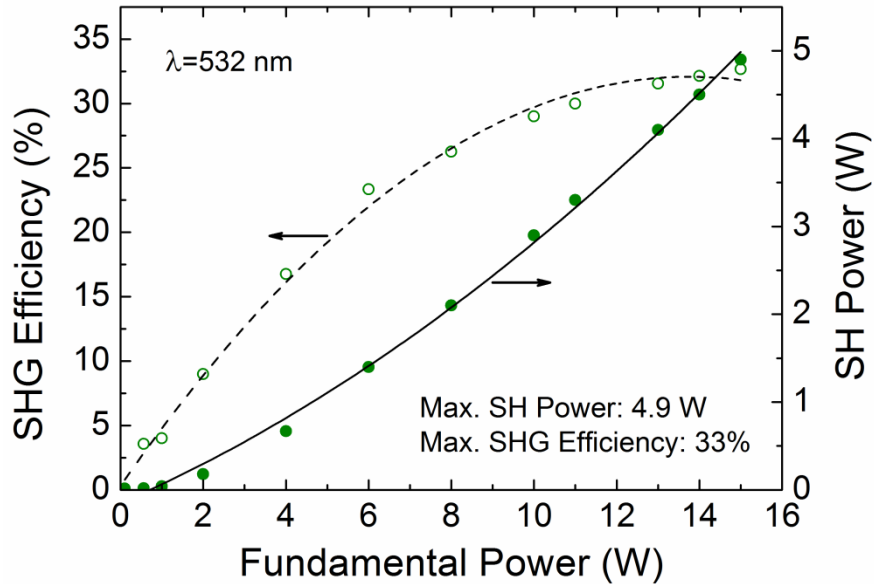
Figure 3.8: Variation of the SH power and SHG efficiency as a function of fundamental power.

3.4.1.3 Power scaling and efficiency

With the perspective of a future characterization of the generated UV output in the second stage, we first investigated the performance of the SHG stage. In Figure 3.8 it is shown the power scaling and efficiency results for single-pass SHG in the 10-mm-long BIBO crystal. The green power increases quadratically, as expected, providing a maximum of 4.9 W for the highest fundamental power of 15.0 W at the input to the BIBO crystal, at a single-pass conversion efficiency of 33%. Also shown in Figure 3.8 is the variation of SHG efficiency with fundamental power, which is expected to be linear. However, at high input power levels the variation is no longer linear, implying saturation, as observed previously [39,77,92].
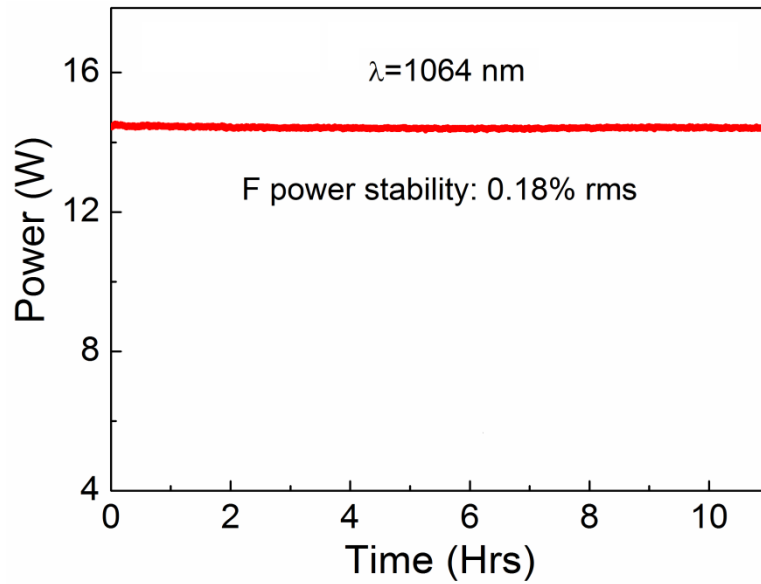
Figure 3.9: Long-term power stability of the mode-locked Yb-fiber-laser used as pump
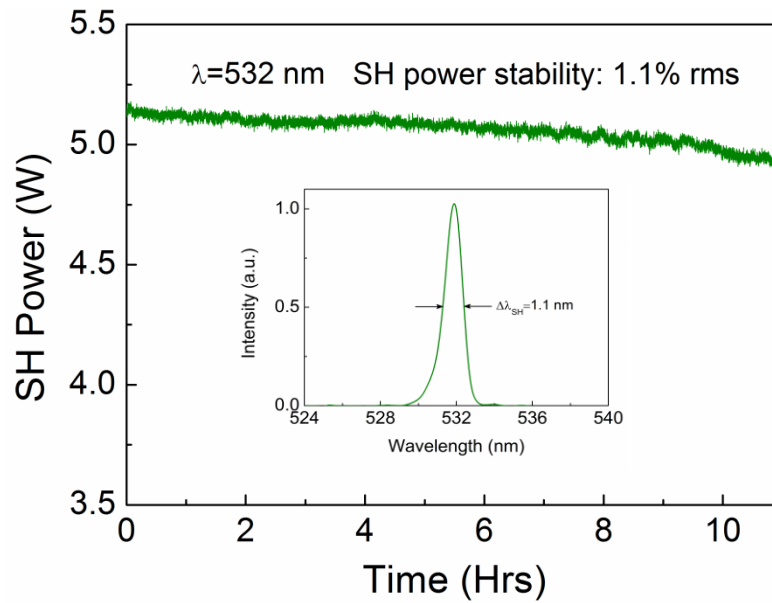
source over 11 hours.

Figure 3.10: Long-term power stability of the green source over 11 hours. Inset: SHG

spectrum, presenting a FWHM of 1.1 nm broad.

3.4.1.4 Power stability and spectrum

Using the previous mentioned mode-locked Yb-fiber-laser as a pump source, we recorded its long-term passive power stability, which presents a value better than 0,18% over 11 hours working at 16 W of pump power. This power stability measurement can be observed in Figure 3.9.

Additionally, we recorded the average passive power stability of the generated green beam, which exhibits remarkable profile without any active stabilization. As evident from Figure 3.10, an average passive power stability better than 1.1% over 11 hours has been observed. The fluctuation in the average power might be attributed to the mechanical vibrations, air currents and temperature variations, as the measurements were taken in an open laboratory environment. We have observed no sign of damage to the nonlinear crystal or beam quality degradation in the UV. Also shown in the inset of Figure 3.10 is the spectrum of the generated SH radiation centered at 0.532 μm, measured using a spectrometer with a resolution of 0.27 nm (OceanOptics, HR4000). It presents a FWHM bandwidth of $\Delta\lambda_{SH} = 1.1$ nm.

3.4.1.5 Output beam quality

Additionally to the previous parameters, for a successful attainment of a maximum SHG output power and efficiency, it is crucial to consider the spatial walk-off parameter. It causes angular separation of orthogonally polarized ordinary and extraordinary waves within the nonlinear crystal and effectively reducing the gain length for SHG [79]. Using the formalism for biaxial crystals described previously [93],

we numerically calculated the walk-off angle as function of the pump wavelength at a phase-matching angle of θ_{pm} = 168.8º for type-I ($ee{\rightarrow}o$) SHG in the *yz*-plane of BIBO crystal. This calculation is presented in Figure 3.11.

As the input beam at 1.064 μm is extraordinary polarized, the SH beam experiences a spatial walk-off of ρ = 25.54 mrad. As a result, the SHG beam profile becomes elliptic although it can be circularized using suitable beam shaping optics [94].
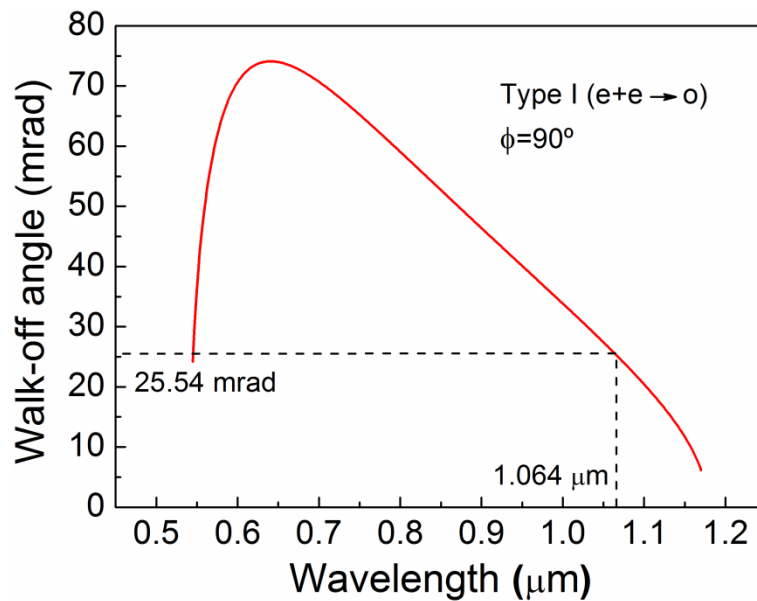

Figure 3.11: Variation of walk-off angle for type-I ($ee{\rightarrow}o$) phase-matching in *yz*-plane in BIBO crystal as a function of fundamental wavelength.

3.4.2 Sum-frequency generation using BIBO crystal

UV sources are of great interest for a variety of applications including quantum optics, optical data storage, photolithography, atmospheric sensing, flow cytometry, combustion diagnostics and other life science applications [29,30,72,95]. For many

years, access to the UV spectral region was possible mainly by bulky, complex, and power-hungry gas lasers [96]. With the advent of nonlinear materials such as LBO and BBO, optical frequency conversion has proved an attractive alternative to reach the UV wavelength range, but they present a relatively low nonlinearity (~0.7 pm/V and ~2 pm/V, respectively). Other attainment for obtaining UV might be throughout first-order QPM SFG into the UV. However it requires a grating period of 2 μm, which is still beyond the capabilities of current fabrication technology [40]. On the other hand, the birefringent material, BIBO, possesses unique nonlinear optical properties for frequency conversion from the UV to IR [3,36,76]. It can be phase-matched for UV generation at room temperature under type-I ($ee{\rightarrow}o$) interaction using SFG of IR and green radiation. Its relatively high optical nonlinearity (d_{eff} ~ 3.9 pm/V) [34], bulk UV damage threshold (50 MW/cm^2) [77], and low UV absorption coefficient (α_{UV} < 0.02 cm^{-1}) [3,36] make it a promising alternative for SFG into the UV. It also presents a nonlinear figure of merit 20 times larger as compared to that of LBO. As such, BIBO offers highly attractive properties for UV generation using SFG of 1.064 μm and 0.532 μm radiation [40].

By using the Sellmeier equations reported in [35], here we present the theoretical calculations of the phase-matching curve for SFG as well as the angular and spectral acceptance bandwidths that were necessary for a successful realization of this experiment. In the *yz*-plane, type-I interaction ($ee{\rightarrow}o$) phase-matching could be reached for incidence angles between θ ~ 90º and 180º, over a fundamental wavelength range from 0.542 to 1.18 μm. Besides, as in previous sections, walk-off calculations were realized in order to present a correct explanation of the output beam profile in the UV.
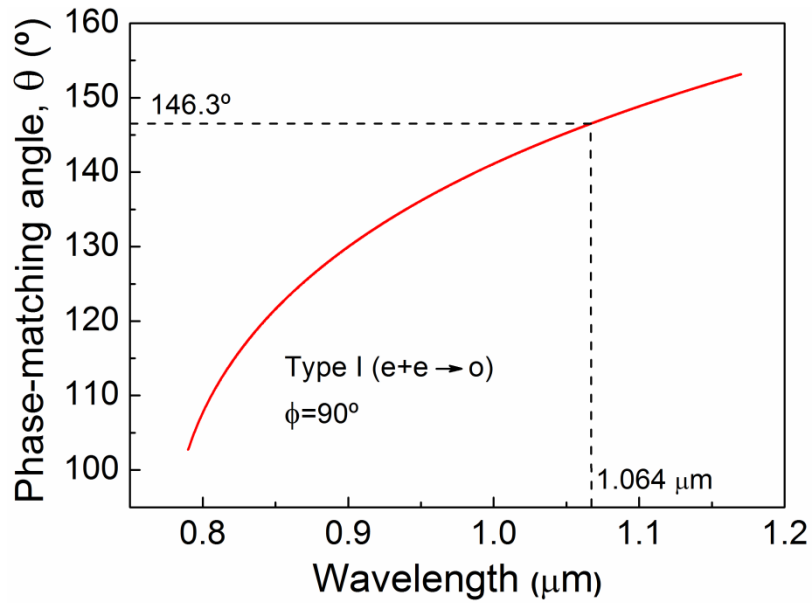
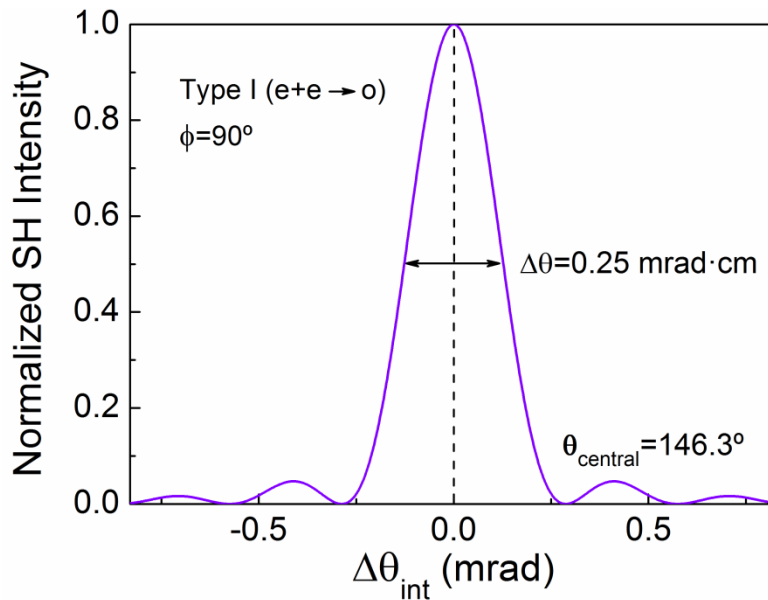Figure 3.12: Phase-matching curve for SFG for type-I (*ee→o*) interaction in the *yz*-plane.

Figure 3.13: Angular acceptance bandwidth for SFG for type-I (*ee→o*) interaction in the *yz*-plane.

3.4.2.1 Phase-matching

As it is shown in Figure 3.12, the phase-matching curve for SFG in the *yz*-plane, type-I interaction (*ee→o*) has been numerically calculated from 0.77 to 1.17 μm of pump wavelength for the BIBO crystal. It presents a corresponding phase-matching angle going from θ ~ 102º to 151º respectively. Of particular interest is the calculated value for a pump wavelength at 1.064 μm. For this value, the phase-matching angle is θ_{pm} = 146.3º, which is the value used in the realization of this experiment.

3.4.2.2 Acceptance bandwidths

For a successful and efficient SFG output, we studied the phase-matching properties of the BIBO crystal by evaluating its angular, in Figure 3.13, and spectral acceptance bandwidths as in the previous section 3.4.1.2. However, in this case we have calculated the spectral acceptance bandwidths for the two involved waves: 1.064 and 0.532 μm independently, as shown in Figure 3.14 and 3.15 respectively. The final value of the spectral acceptance bandwidth of the SFG process in BIBO will be the most restrictive of the two values. The angular acceptance bandwidth presents a FWHM bandwidth of $\Delta\theta$ = 0.25 mrad·cm at a central phase-matching angle of θ_{pm} = 146.3º. Further, the independent values of the two spectral acceptance bandwidths present a FWHM bandwidth of $\Delta\lambda$ ~ 0.2 nm at 1.064 μm in Figure 3.14 and $\Delta\lambda$ ~ 0.1 nm at 0.532 μm in Figure 3.15. Therefore, we define the final value of the spectral acceptance bandwidth of this stage as $\Delta\lambda$ ~ 0.1 nm.

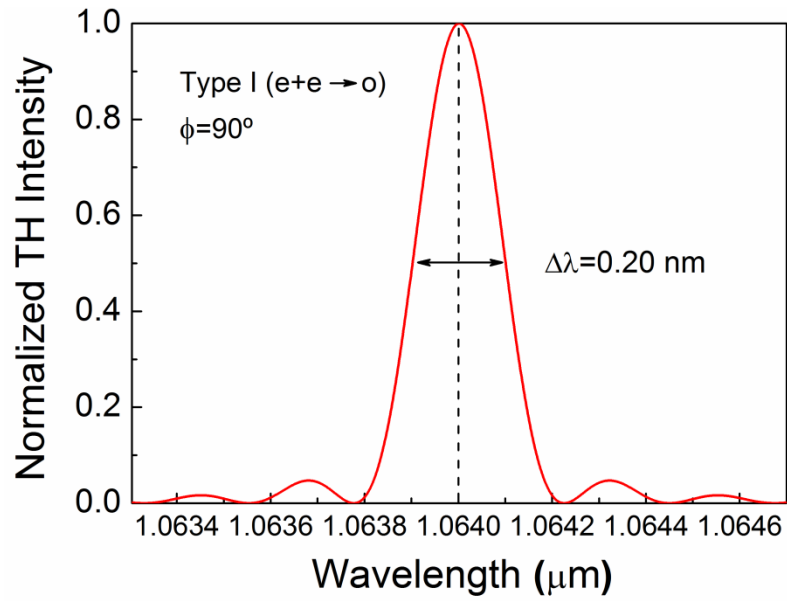Figure 3.14: Spectral acceptance bandwidth for SFG for type-I (*ee→o*) interaction in the *yz*-plane of the wave at 1.064 *μ*m.
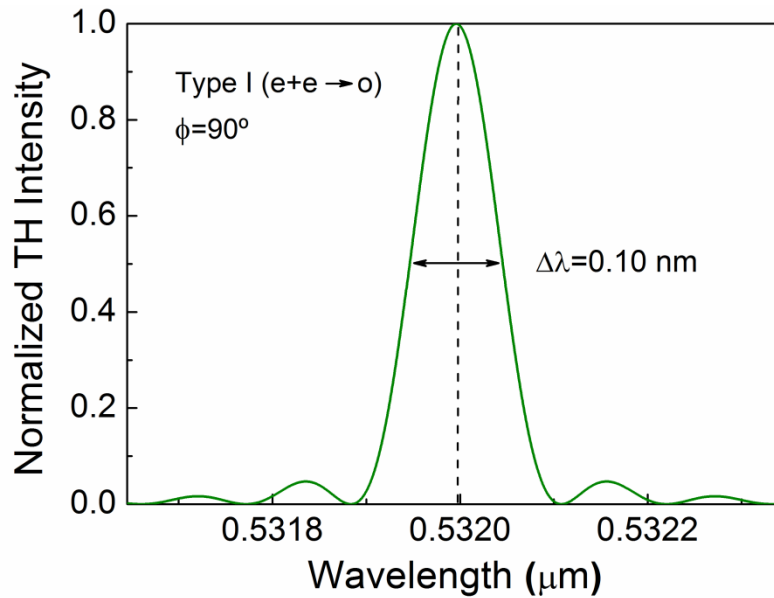

Figure 3.15: Spectral acceptance bandwidth for SFG for type-I (*ee→o*) interaction in the *yz*-plane of the wave at 0.532 *μ*m.

78

3.4.2.3 Power scaling and efficiency

In order to characterize our UV source, we performed the power scaling measurement of the generated UV radiation at the output of the SFG stage. These measurements are represented in Figure 3.16, which shows the variation of single-pass UV power generated in a 10-mm-long BIBO crystal as a function of input fundamental power to the SHG stage. It can be seen that we achieved as much as 164 mW of UV power at 354.7 nm for a fundamental power of 15.0 W at 1064 nm, presenting a single-pass maximum conversion efficiency of 1.12%. During the measurements, as the fundamental power has been increased stepwise, the angular phase-matching of the BIBO crystal has been always adjusted to generate the maximum UV power.
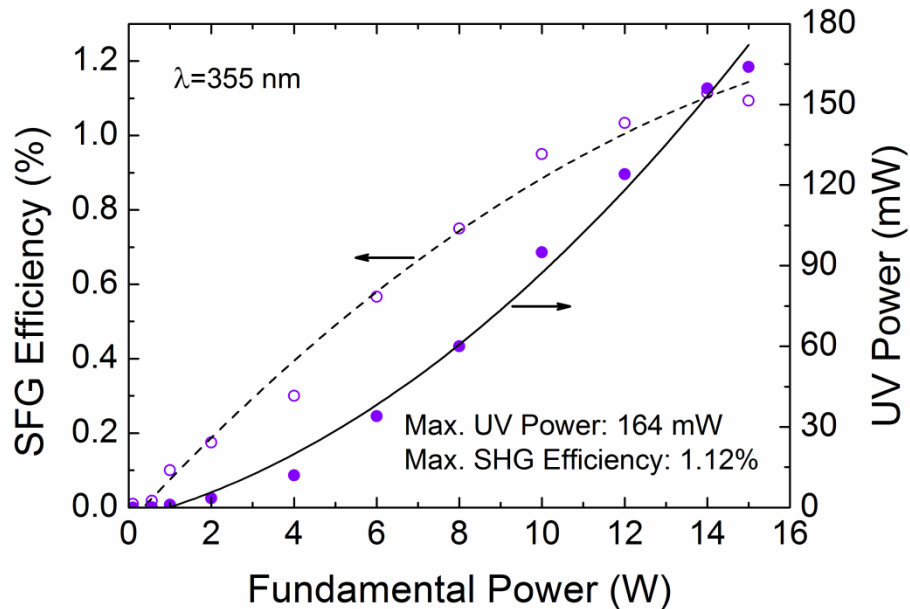

Figure 3.16: Variation of the UV power and efficiency as a function of fundamental power.

3.4.2.4 Power stability and spectrum

The average passive power exhibits remarkable stability obtained without any active stabilization. It presents passive power stability better than 2% over 11 hours and is presented in Figure 3.17. The power stability of the pump laser was shown in Figure 3.9. The fluctuation in the average power might be a consequence of the fluctuation in the SH power stability (Figure 3.10) as well as to the mechanical vibrations, air currents and temperature variations also suggested in subsection 3.4.1.4. No sign of damage to the nonlinear crystal or beam quality degradation have been observed during the realization of the experiment. The spectrum of the generated UV radiation, which is centered at 354.7 nm, has been measured using a spectrometer with a resolution of 0.27 nm (OceanOptics, HR4000). It presents a FWHM bandwidth of $\Delta\lambda_{TH} = 1.0$ nm limited by the instrument resolution and it is presented in the inset of Figure 3.17.
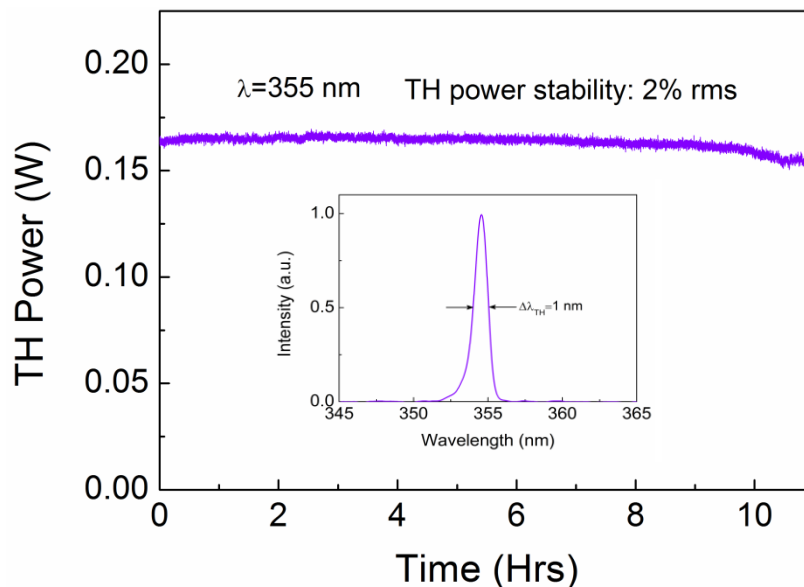
Figure 3.17: Long-term power stability of the UV source over 11 hours. Inset: UV spectrum, presenting a FWHM of 1.0 nm broad.
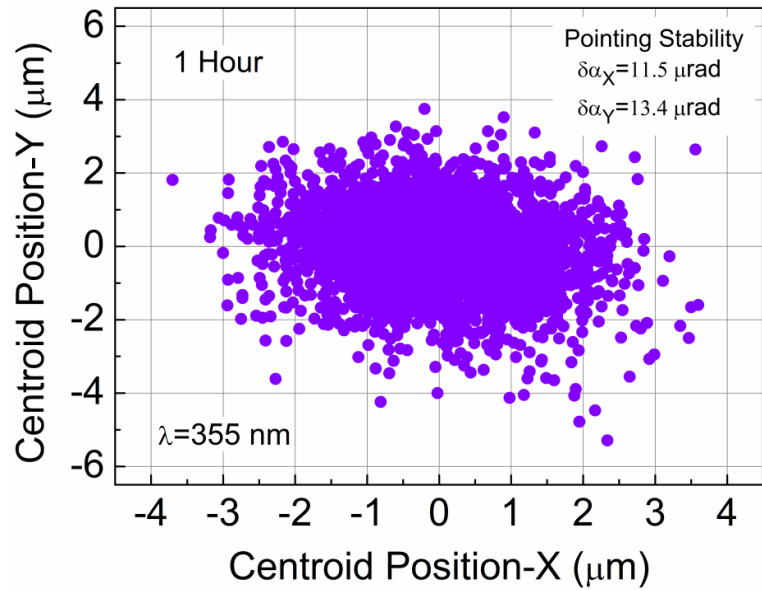
Figure 3.18: Pointing stability of the UV measured over 1 hour.

Finally, we measured the beam pointing stability of the generated UV output. We recorded the deviation in the centroid position by focusing the UV beam with a lens and using a scanning beam profiler, resulting in a pointing stability <11.5 *μ*rad in the *x*-direction and <13.4 *μ*rad in the *y*-direction, respectively, as shown in Figure 3.18. Additionally, we measured the UV beam profile using a scanning beam profiler. This profile is shown in Figure 3.19.

Figure 3.19: UV beam profile.

3.4.2.5 Output beam quality

As mentioned in section 3.5.2.3, angular separation of the orthogonally polarized ordinary and extraordinary waves within the nonlinear crystal –walk-off– should be considered for a successful attainment of maximum output power and efficiency of any frequency conversion process. Here, the theoretical walk-off angle curves at 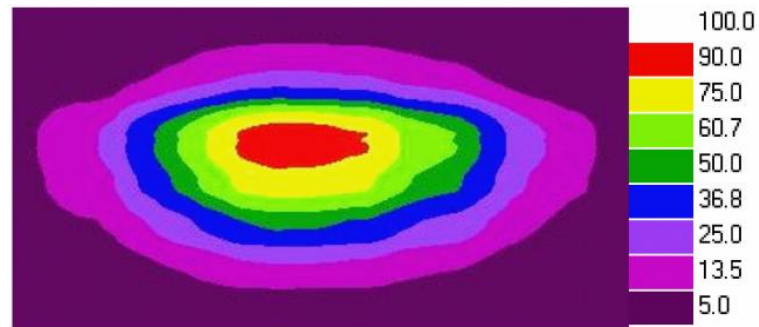a phase-matching angle of θ_{pm} = 146.3º for type-I (*ee→o*) SFG in the *yz*-plane of BIBO crystal of the two input beams at 1064 and 532 nm are presented in Figure 3.17. Due to the fact that both input beams are extraordinary polarized, they experience a spatial walk-off of ρ_F = 64.45 mrad and ρ_{SH} = 67.73 mrad –shown in Figure 3.20 and Figure 3.21 respectively–. By doing the difference between the two waves, we have calculated the relative walk-off, corresponding to the small angle of $\Delta\rho$ ~ 3.3 mrad, resulting in an elliptic UV beam as shown in Figure 3.19. As previously mentioned, by using proper cylindrical lenses the beam can be readily circularized [94].
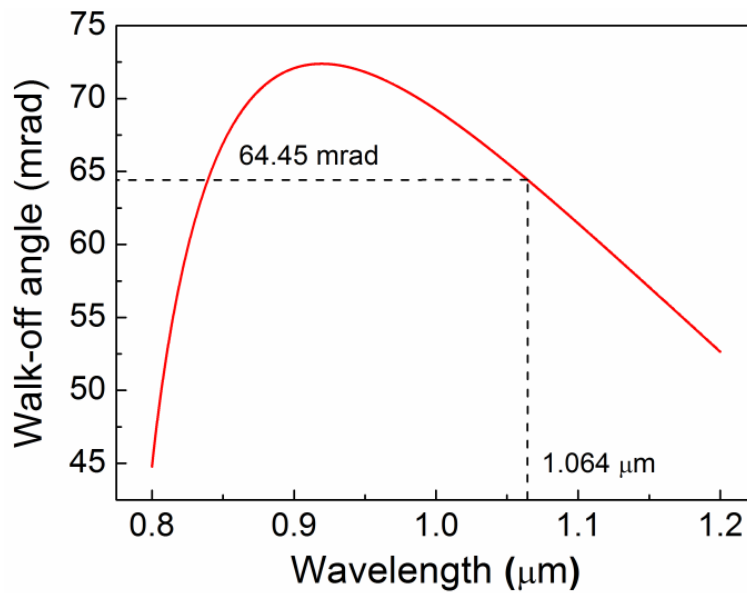

Figure 3.20: Variation of walk-off angle for type-I (*ee→o*) phase-matching in *yz*-plane

in BIBO crystal as a function of fundamental wavelength.
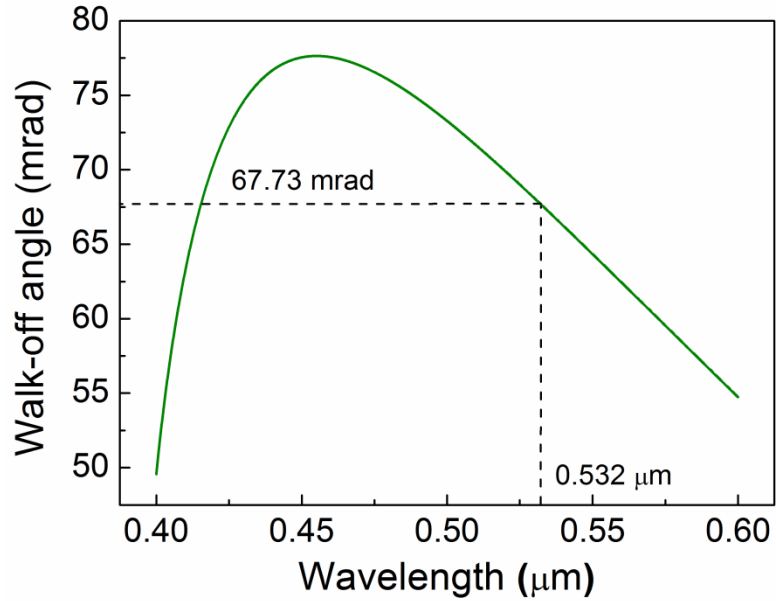
Figure 3.21: Variation of walk-off angle for type-I (*ee→o*) phase-matching in *yz*-plane

in BIBO crystal as a function of the SH wavelength.

3.5 LBO-BIBO section: Single-pass, picosecond UV source using a LBO and BIBO crystals

In this section, we demonstrate a compact and stable UV source based on a practical and robust architecture using single-pass SHG in LBO followed by SFG in BIBO, pumped by a mode-locked Yb-fiber laser (Fianium FP1060-20) at 1064 nm, as evident from the Figure 3.22. It provides as much as 1.2 W of average UV power at 355 nm at an IR-to-UV conversion efficiency of 7.2%. In the first stage, the 30-mm-long LBO crystal which is cut at $\theta = 90°$ ($\varphi = 0°$) for type-I (*oo→e*) NCPM in the optical *xy*-plane at $T_{pm} = 148.2$ °C, it performs single-pass SHG, obtaining up to 9.1 W of average green power at 532 nm with an efficiency of 54%. The generated green pulses have duration of 16.2 ps at a repetition rate of 79.5 MHz, presenting passive power stability better than 0.5% rms and a

Figure 3.22: Schematic view of the LBO-BIBO configuration.

pointing stability <12 μrad over 1 hour, in high beam quality. In the second stage, the undepleted fundamental beam and generated SH are collimated and are refocused using two concave mi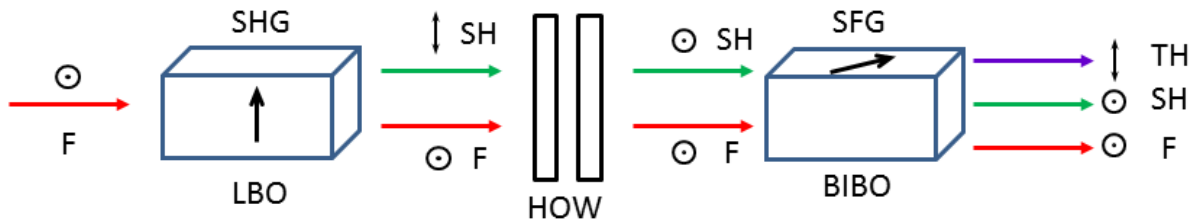rrors (r_1 = 150 mm, r_2 = 200 mm) into an elliptic beam waist radius of w_{02} ~ 54 × 86 μm in a second 10-mm-long BIBO crystal cut at θ = 146.2° (ϕ = 90°) for type-I ($ee{\rightarrow}o$) SFG into the UV. The generated UV exhibits passive power stability better than 0.4% rms over 3 hours, and a pointing stability below 45 μrad over 1 hour in TEM$_{00}$ spatial profile. To the best of our knowledge, this is the first attempt to generate high-average-power UV radiation in BIBO below 370 nm [38].

3.5.1 Second-harmonic generation using LBO crystal

Figure 3.23 shows the temperature phase-matching as a result of representing the ordinary and extraordinary refractive indices of the LBO crystal for a pump wavelength at 1.064 μm using the Sellmeier equations given by [97]. The temperature for an optimum phase-matching is T_{pm} = 148.2 °C at room temperature. However, along our experiment we were obtaining the best efficiency when setting our crystal oven up to T = 158.3 °C. This is due to the real temperature in our laboratory, which should be about 10° C below the room temperature commonly known at T_{room} = 23 °C.
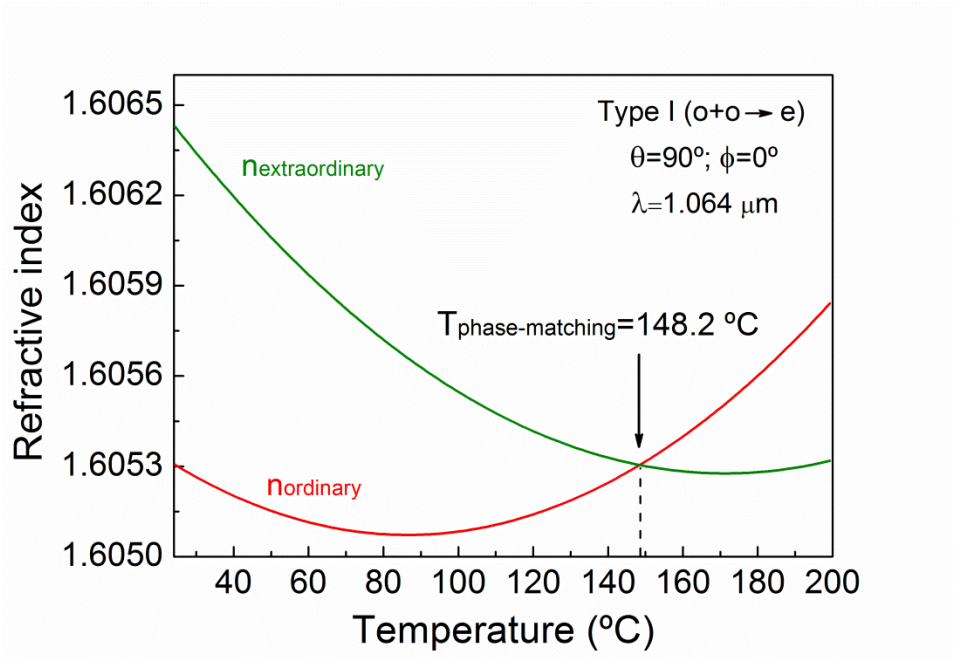
Figure 3.23: Temperature phase-matching curve for type-I ($oo{\rightarrow}e$) SHG in the *xy*-

plane.

3.5.1.1 Power scaling

In order to characterize the generated UV output, we first investigated the performance of

the SHG stage. The power scaling and efficiency results for single-pass SHG in LBO are

shown in Figure 3.24. The fundamental beam is focused at the center of the LBO crystal

to a waist radius of $w_{01} \sim 34$ μm, corresponding to a focusing parameter for the LBO

crystal of $\xi \sim 2.74$ [60]. The green power increases quadratically, as expected, providing a

maximum of 9.1 W for the highest fundamental power of 16.8 W at the input to the LBO

crystal, at a single-pass conversion efficiency of 54%. Also shown in Figure 3.24 is the

variation of SHG efficiency with fundamental power, which is expected to be linear.

However, at high input power levels the variation is no longer linear, implying saturation,

as also observed previously [39,77,92].

Figure 3.24: Variation of the SH power and SHG efficiency as a function of fundamental power.

Figure 3.25: Typical autocorrelation trace of the SH at 532 nm with duration of 16.2 ps (x 1.414, assuming a Gaussian pulse shape). Inset: SH spectrum measured at a central wavelength of 532 nm with a FWHM bandwidth of 0.6 nm.

3.5.1.2 Temporal and spectral characterization

We performed temporal and spectral characterization of the generated green beam. Figure 3.25 shows a typical autocorrelation profile a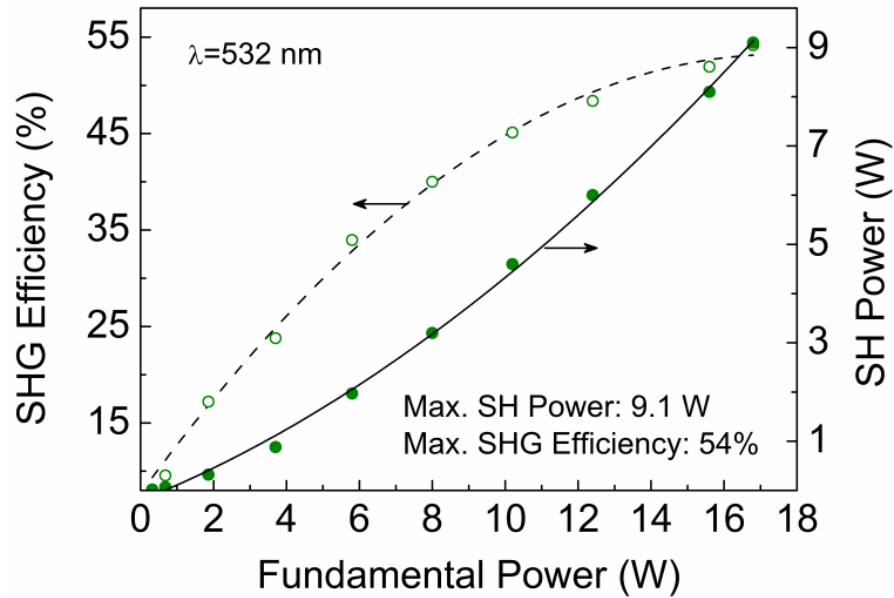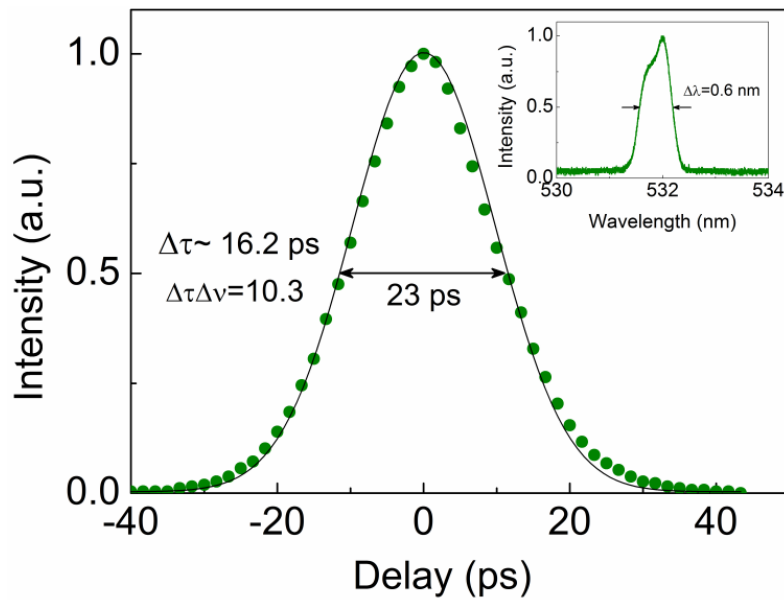t 532 nm, indicating a FWHM duration of 23 ps. Assuming a Gaussian pulse shape, this corresponds to a pulse duration of 16.2 ps. This value was also confirmed by repeating the measurement at different fundamental power levels. The SH spectrum, measured using a visible spectrum analyzer, is centered at 532 nm with a FWHM bandwidth of 0.6 nm, as shown in the inset of Figure 3.25, resulting in $\Delta v \Delta \tau \sim 10.3$. The large time-bandwidth product is essentially attributed to the non-transform-limited ($\Delta v \Delta \tau \sim 7.4$) fundamental pulses from the Yb-fiber laser.

3.5.1.3 Power and temporal stability

We also recorded the long-term power stability of the generated green beam at 9 W of average power, with the result shown in Figure 3.26. As can be seen, the output power at 532 nm exhibits excellent passive stability of better than 0.5% rms over 16 hours, compared to 0.24% rms for the fundamental measured over the same period of time. The power stability of the pump laser was shown in Figure 3.9. The far-field energy distribution of the generated green beam, measured at 9 W and at ~1 meter from the LBO crystal, is shown in inset of Figure 3.26, confirming TEM_{00} profile with a circularity of >97% owing to NCPM in LBO. Also, in Figure 3.27 is shown the green beam pointing stability. Using a lens of $f = 125$ mm focal length and a scanning beam profiler, we measured the deviation in the green beam centroid position, resulting in a pointing stability <12 μrad in the x-direction and <10 μrad in the y-direction, respectively.
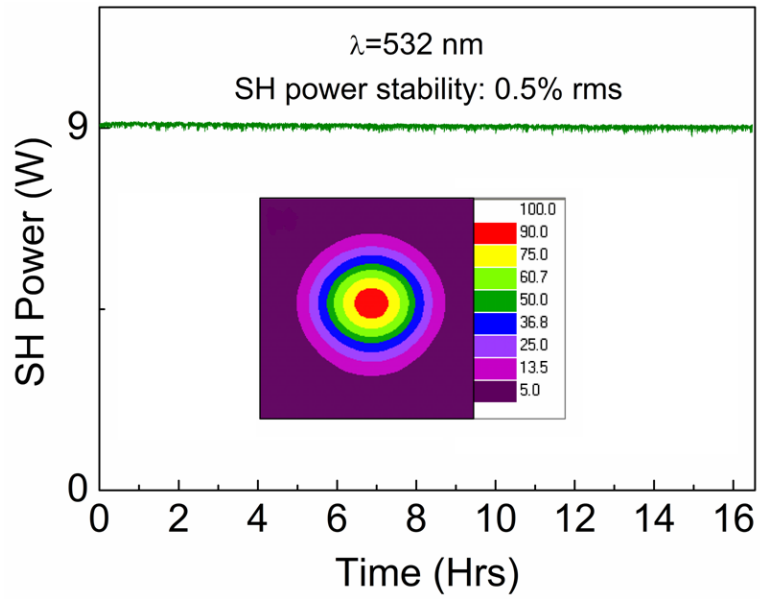
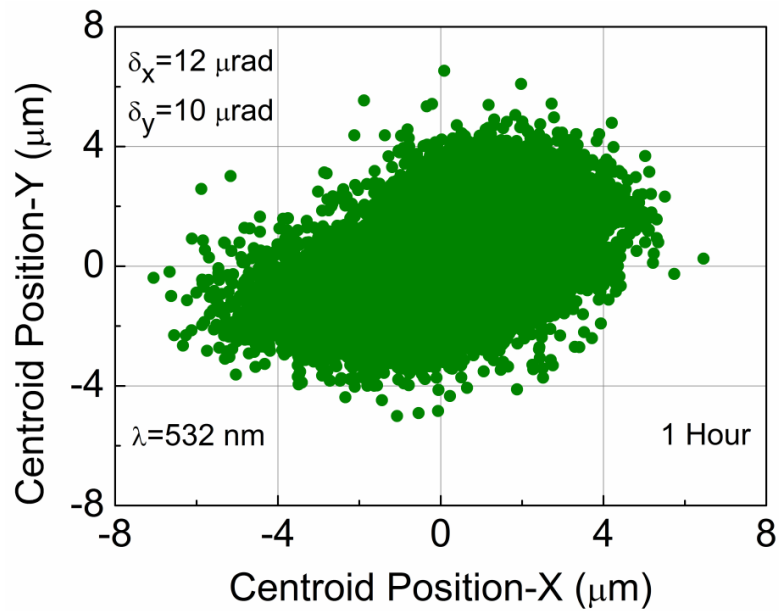Figure 3.26: Long-term power stability of the green source over 16 hours.

Figure 3.27: Green beam pointing stability of the SH measured over 1 hour.

3.5.2 Sum-frequency generation using BIBO crystal

In same way that in section 3.4.2, here, a compact and stable UV source based on a practical and robust architecture using BIBO is demonstrated. In this case, as evident from the Figure 3.22, a single-pass SHG in LBO pumped by a mode-locked Yb-fiber laser (Fianium FP1060-20) at 1064 nm in pulses of 20 ps duration at 79.5 MHz repetition rate provides as much as 9.1 W of average green power at 532 nm. This beam is collimated together with the undepleted fundamental beam and refocused using two concave mirrors ($r_1 = 150$ mm, $r_2 = 200$ mm) in a second 10-mm-long BIBO crystal cut at $\theta = 146.2°$ ($\phi = 90°$) for type-I ($ee{\rightarrow}o$) SFG. The source provides as much as 1.2 W into the UV at 355 nm, presenting at an IR-to-UV conversion efficiency of 7.2%, with passive power stability better than 0.4% rms over 3 hours, and a pointing stability below 45 μrad over 1 hour in TEM_{00} spatial profile.

3.5.2.1 Power scaling

After the complete characterization of the SHG output, we performed optimization of the SFG stage. In order to maximize SFG efficiency, ideally one green photon would be required for every fundamental photon to realize sum-frequency mixing, thereby generating one UV photon. This implies an optimum 1064/532 nm power ratio of 1/2. In the SHG stage, we generated 9.1 W of green power, with 7.6 W of unconverted fundamental remaining for SFG, resulting in a power ratio of ~1/1.2. Further, the maximum efficiency for SFG is achieved when the interacting beams have optimum overlap throughout the length of the crystal, but spatial walk-off significantly reduces this overlap. As both beams (1064 nm and 532 nm) at the input to the BIBO crystal are
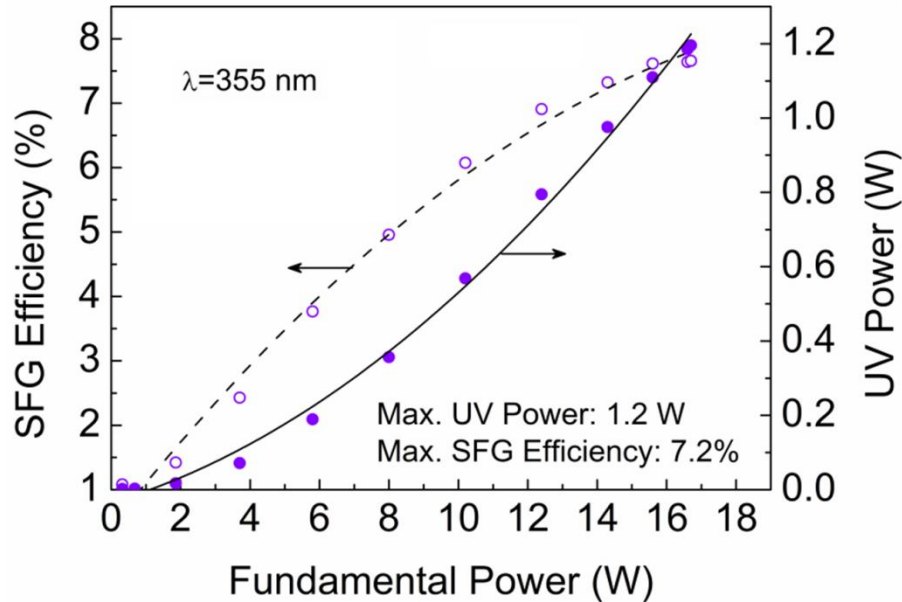
Figure 3.28: Variation of the UV power and efficiency as a function of fundamental
power.

extraordinary, they experience a small relative walk-off angle, $\Delta\rho \sim 3.2$ mrad. This fact
results in an offset of 650 μm and 680 μm at the exit face of the BIBO crystal for the
fundamental and SH beam, respectively. As such, larger beam diameters are required to
offset spatial walk-off, which in turn leads to reduced efficiency due to lower intensities.
Hence, we used the mirrors, M_1 and M_2, at small angles to focus the undepleted
fundamental as well as the SH beam to an elliptic waist, resulting in a horizontal focused
radius of $w_{02} \sim 63 \times 187$ μm. The UV power scaling results as a function of the
fundamental power, under this focusing configuration, are shown in Figure 3.28, where
the data have been corrected for the transmission loss of the UV filter, F. As evident, the
UV average power increases with the fundamental, reaching a maximum of 1.2 W for the
highest input Yb-fiber power 16.8 W, at an IR-to-UV single-pass conversion efficiency of
7.2%. This efficiency is comparable to that obtained in Reference [92] at similar average
input power, with a corresponding peak pulse power of 18.7 kW in a 17.6-mm-long LCB

crystal. This is ~1.8 times larger than the input peak power of 10.5 kW used here in a 10-mm-long BIBO crystal.
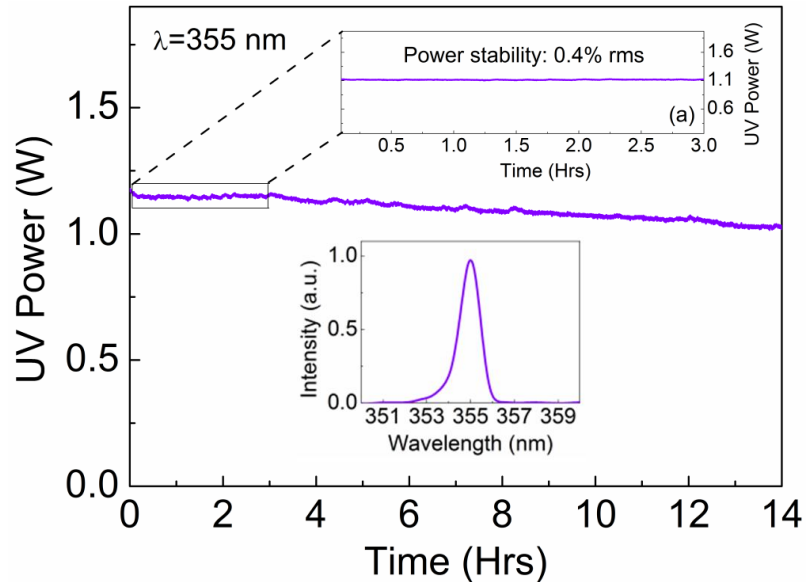
Figure 3.29: Long-term power stability of the UV source over 14 hours. Inset: (a) UV spectrum, presenting a FWHM of 1.0 nm broad.

3.5.2.2 Power and temporal stability and spectrum

Further, we recorded the passive long-term power stability of the generated UV output over 14 hours. The power stability of the pump laser was shown in Figure 3.9. As can be seen in Figure 3.29, the UV power exhibits a long-term drift resulting in a slow decline from 1.2 W down to ~1 W after 14 hours. By translating the crystal to focus the input beams to a new position inside the BIBO, we could readily recover the maximum UV power. This long-term drift in UV power could be attributed to photo-induced damage [98], two-photon absorption or dynamic color center formation, previously observed in borate crystals [99]. However,

photo-induced damage in BIBO can be repaired with high-temperature annealing at ~300 ºC [98], thus potentially improving the long-term power stability. Confirmation of the origin of the long-term power drop requires further studies. Nevertheless, during the first 3 hours of the measurement, the UV power is recorded to exhibit passive power stability better than 0.4% rms, as shown in the inset (a) of Figure 3.29. To the best of our knowledge, such power stability measurements as performed here have not been previously reported for UV generation in earlier works involving any other nonlinear material at any power level. We have not observed any permanent damage in the BIBO crystal even after >14 hours of continuous operation and repeated operation over many days and weeks. Also shown in the inset (b) of Figure 3.29 is the UV spectrum centered at 355 nm, measured using UV-visible spectrometer, indicating a bandwidth of ~1 nm (FWHM), limited by the instrument resolution.
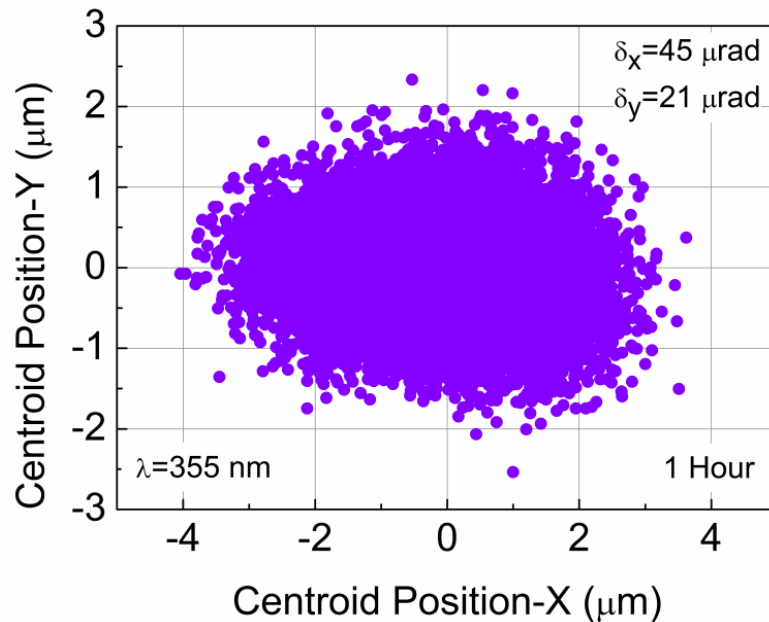
Figure 3.30: Pointing stability of the UV measured over 1 hour.

Finally, we measured the beam pointing stability of the generated UV output. We recorded the deviation in the centroid position by focusing the UV beam with a f = 50 mm focal length lens and using a scanning beam profiler, resulting in a pointing stability <45 μrad in the x-direction and <21 μrad in the y-direction, respectively, as shown in Figure 3.30.

3.5.2.3 Output beam quality

In Figure 3.31 is shown the UV beam profile measured 50 cm from the BIBO crystal, at >1 W of UV power, using a scanning beam profiler, making evident the confirmation of the TEM_{00} spatial mode. The far-field energy distribution of the UV beam exhibits a circularity of ~47% owing to the spatial walk-off in BIBO, but this can be readily circularized as mentioned previously.
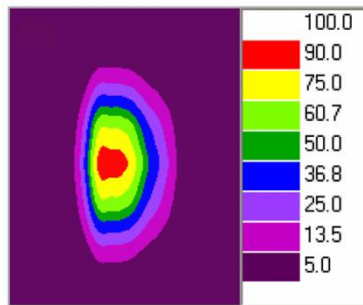
Figure 3.31: UV beam profile measured using a scanning beam profiler.

3.6 Conclusions

In this chapter, we have demonstrated a compact, stable, high-power picosecond UV source at 355 nm based on single-pass SFG in BIBO pumped by a mode-locked Yb-fiber laser at 1064 nm. The combination of Yb-fiber laser with single-pass conversion results

in a highly simplified and practical design, preserving the key advantages of fiber technology with regard to a compact, portable and air-cooled architecture. We have generated up to 1.2 W of UV average power at 79.5 MHz at an IR-to-UV conversion efficiency of 7.2%, with power stability better than 0.4% rms over 3 hours and pointing stability better than 45 μrad over 1 hour, in TEM$_{00}$ spatial profile. The generated UV power could be further enhanced by using a delay line to improve temporal overlap of 1.064 μm and 0.532 μm pulses in the crystal, as well as deploying two-crystal compensation scheme to further minimize the residual spatial walk-off in BIBO. With the power scaling potential of Yb-fiber lasers, further increase in the UV power to multiwatt levels is also a clear possibility without damage to the BIBO crystal. Additionally, we have presented the characterization of the SFG with BIBO that, to our knowledge, was never presented before. The obtained results confirm the viability of BIBO as a highly attractive material for efficient generation of low-intensity picosecond pulses in the UV.

4 High-power, picosecond ultraviolet source at 266 nm based on β-BaB$_2$O$_4$

This chapter constitutes the following publication:

1. *1.8 W, 80 MHz, picoseconds, Yb-fiber-based ultraviolet sources at 266 nm using β-BaB$_2$O$_4$*

   S. Chaitanya Kumar, J. Canals Casals, **E. Sánchez Bautista**, K. Devi and M. Ebrahim Zadeh.

   Optics Letters, **40**(10), 2397-2400 (2015).

4.1 Motivation

Generation of high-power, high-repetition-rate, picosecond UV sources are of great interest for a variety of scientific, industrial and medical applications such as precise material processing, laser marking, disc mastering, optical data storage, atmospheric sensing and spectroscopy among many others [100,101]. Nonlinear frequency conversion of well-established high-power solid state lasers in single-pass configuration is an attractive approach to produce UV radiation [39]. The development of high-average

Crystal	UV Cutoff (nm)	Phase-matching	Type / Interaction	P-M angle	d_{eff} (pm/V)	α_{UV} (cm^{-1}) @ 266 nm	ρ (mrad)	Angular acceptance [mrad·cm]	Hygrospicity
BBO	~180	Birefringent	Type-I ($oo{\rightarrow}e$)	$\theta = 47.56º$	1.75	<0.17	85.3	0.19	Hygroscopic
CLBO	~180	Birefringent	Type-I ($oo{\rightarrow}e$)	$\theta = 61.5º$	0.79	-	32.96	0.54	Highly hygroscopic
KABO	~180	Birefringent	Type-I ($oo{\rightarrow}e$)	$\theta = 57.1º$	0.24	0.10	47.16	0.34	Non-hygroscopic
RBBF	~170	Birefringent	Type-I ($oo{\rightarrow}e$)	$\theta = 36.3º$	0.34	0.62	56.49	0.32	Non-hygroscopic
KBBF	<160	Birefringent	Type-I ($oo{\rightarrow}e$)	$\theta = 36.3º$	0.39	0.11	52.88	0.42	Non-hygroscopic

Table 4.1: Phase-matching properties of some nonlinear crystals for 266 nm generation through FHG [67,102].

$$\boldsymbol{\omega + \omega = 2\omega} \qquad \boldsymbol{2\omega + 2\omega = 4\omega}$$

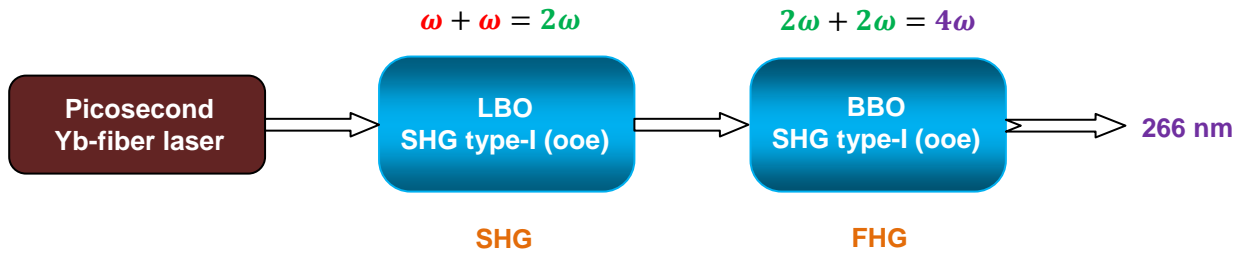| Picosecond Yb-fiber laser | → | LBO SHG type-I (ooe) | → | BBO SHG type-I (ooe) | ⇒ | 266 nm |

SHG   FHG

Figure 4.1: Schematic view of the FH generator using two consecutive SHG processes.

power UV sources at 266 nm through FHG of 1.064 μm fiber lasers in nonlinear crystals is of particular importance due to their compact footprint, lower maintenance costs, higher efficiency, longer lifetime and excellent stability. The features of these sources are strongly dependent on the choice of the nonlinear crystal due to their great variety of characteristics. For this reason, the election of the nonlinear crystal is a crucial factor to accomplish all the desirable properties in the UV source.

Borate crystals are often used in high-power UV generation due to their excellent nonlinear properties. Some of these crystals, such as BBO, $CsLiB_6O_{10}$ (CLBO), $K_2Al_2B_2O_7$ (KABO), $RbBe_2BO_3F_2$ (RBBF) and $KBe_2BO_3F_2$ (KBBF) have been used for FHG of fiber and Nd-based lasers at 266 nm [102]. BBO presents a large effective nonlinear coefficient, which is beneficial for high power 266 nm generation. In Table 4.1 are listed the characteristics of BBO and some other nonlinear crystals for 266 nm generation through FHG. In the last decade, many results have been reported in this regard in high-power 266 nm generation in cw and nanosecond regime, but the output power never exceeded 3 W [103-105] until 2009, when an output of 14.8 W was reported [102,106], which is the highest power described for BBO in nanosecond regime. However, the generation of high-power picoseconds UV generation at MHz repetition rates has been hindered so far.
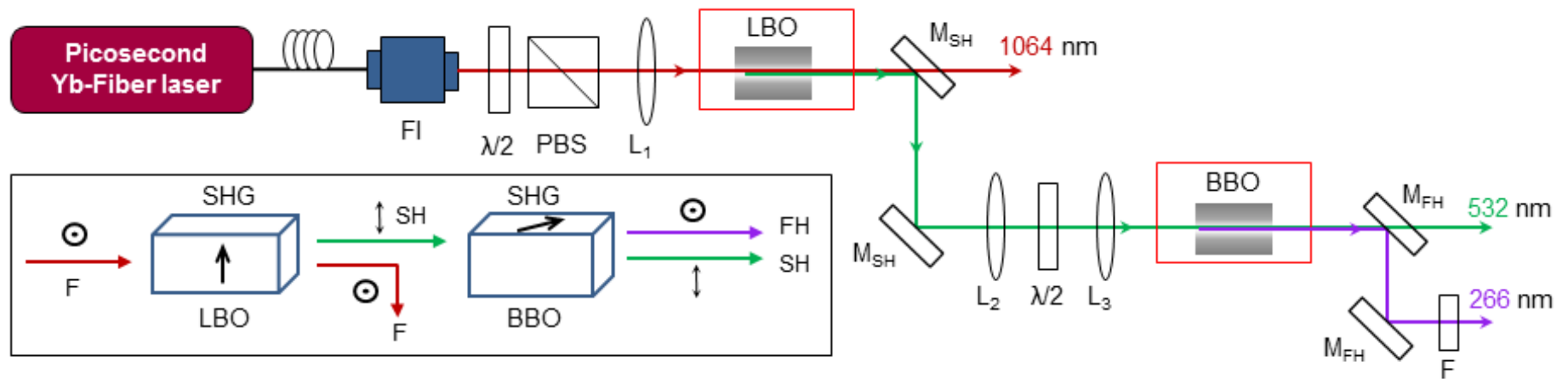
Figure 4.2 Schematic of the experimental setup for single-pass SHG and FHG: $\lambda/2$: Half-wave-plate, *PBS*: Polarizing beam-splitter,

$L_{1,2,3}$: lenses, $M_{SH,FH}$: High-reflective dichroic mirrors for 532 nm and 266 nm respectively.

In this chapter we report a stable, high-power, picosecond, 266 nm UV source based on single-pass FHG of Yb-fiber laser, generating as high as 1.7 W of UV power at 79.5 MHz, in an eliptic Gaussain beam with a TEM_{00} mode profile. Figure 4.1 shows the scheme of the experiment with two stages using two crystals. The first one comprises a second harmonic generator while the second one comprises a fourth harmonic generator. To the best of our knowledge, this is the first report of picosecond UV generation at 266 nm at MHz repetition rates, and at such high single-pass efficiency and average power.

4.2 Experimental setup

The schematic of the experimental setup is shown in Figure 4.2. The fundamental source is a mode-locked Yb-fiber laser (Fianium FP1060-20) delivering up to 20 W of average power at 1064 nm in pulses of 20 ps duration at 79.5 MHz repetition rate. The laser has a double-peaked spectrum with a FWHM bandwidth of ~1.4 nm. The output power is adjusted using a combination of a half-wave plate and a polarizing beam-splitter cube. A second half-wave plate is used to obtain the required polarization for phase-matching in the nonlinear crystals. The experiment is composed by two consecutive stages, each of them with one crystal. First, we used a 30-mm-long LBO crystal with an aperture of 3×4 mm^2 cut at $\theta = 90°$ ($\varphi = 0°$) for type-I ($oo{\rightarrow}e$) NCPM in the optical xy-plane at $T_{pm} = 148.2$ ºC for SHG of the 1064 nm (see Figure 4.3). After, the second stage comprises of a 10-mm-long, 5-mm-wide and 4-mm-thick BBO crystal, cut at $\theta = 47.43°$ ($\varphi = 90°$) for type-I ($oo{\rightarrow}e$) interaction enhancing a subsequent frequency doubling of 532 nm in order to generate the FH of 1064 nm UV output at 266 nm (see Figure 4.4). The end-faces of the LBO crystal are antireflection (AR)-coated ($R < 0.1\%$) at 1064 and 532 nm, while the
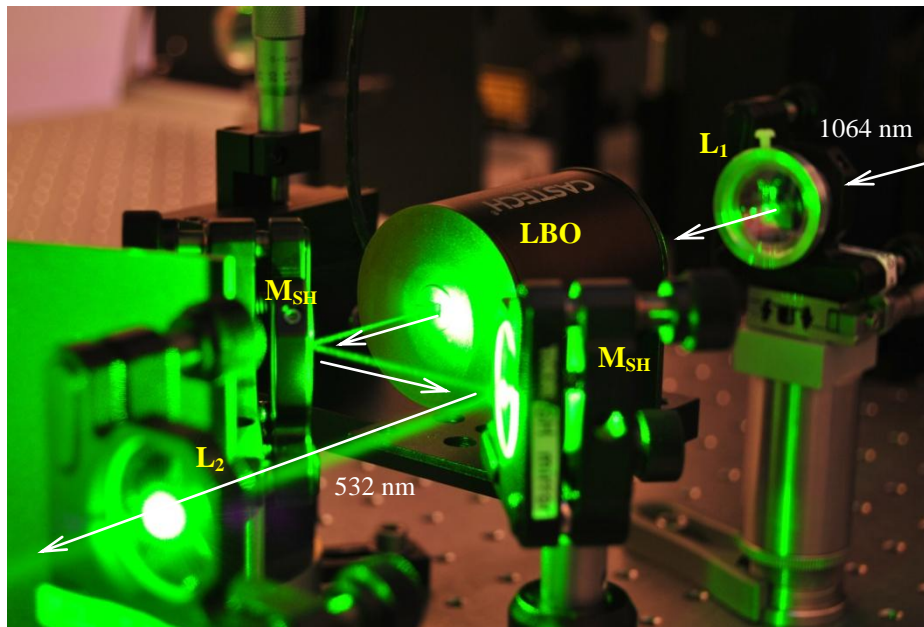
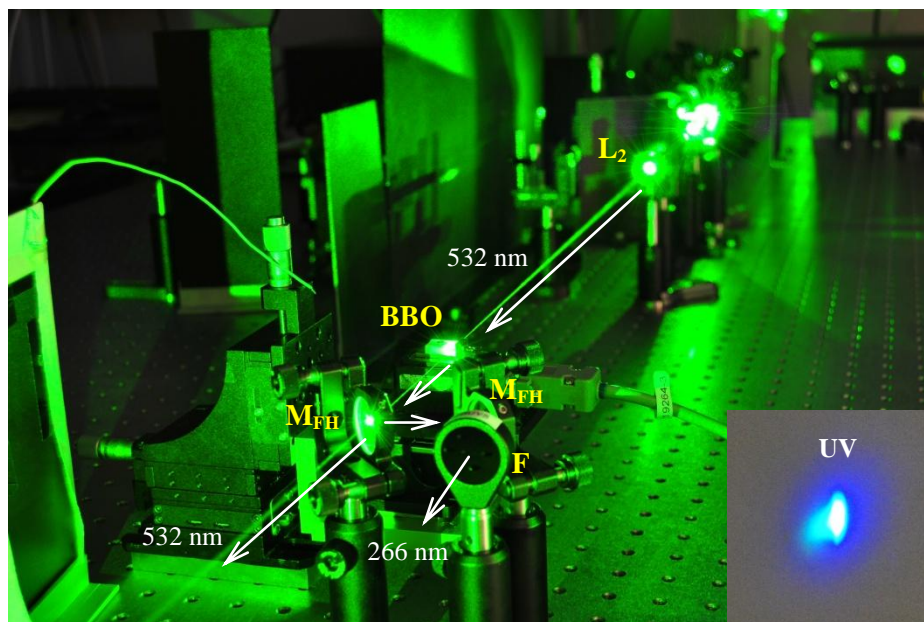Figure 4.3: Picture of the SHG stage using a LBO crystal.

Figure 4.4: Picture of the second SHG stage using a BBO crystal and the corresponding UV beam.

BBO end-faces are AR-coated at 532 and 266 nm.

The fundamental beam is focused at the center of the LBO crystal to a waist radius of $w_0 \sim 34$ μm, corresponding to a focusing parameter for the LBO crystal of $\xi \sim 2.74$ [60], to provide SHG output at 532 nm. The generated SH beam is separated from the fundamental using dichroic mirrors and then refocused using a lens of $f = 175$ mm into the BBO crystal to a waist radius of $w_0 \sim 19$ μm, corresponding to a focusing parameter for the BBO crystal of $\xi \sim 1.4$ obtained, as previously, from Boyd and Kleinman theory [60]. The generated UV radiation at 266 nm is then separated from the SH beams using another set of dichroic mirrors, and further filtered using a FGUV5 glass, *F*, in order to isolate the beam from possible reflections of the other interacting waves.

4.3 Fourth-harmonic generation using BBO crystal

As previously mentioned, a critical parameter for an efficient generation of UV radiation is the choice of nonlinear crystal. Despite its relatively low nonlinear optical coefficient, our studies show that BBO offers the most suitable material features due to high pulse energies are involved along the experiment. As such, the generated picosecond green pulses in the LBO crystal coming from the first stage are again frequency-doubled in a 10-mm-long BBO crystal cut for at $\theta = 47.43°$ for type-I ($oo{\rightarrow}e$) critical phase-matching in a single-pass scheme to achieve the FH of the Yb-fiber laser at 266 nm in the UV. Relevant calculations of the phase-matching angle for an efficient FHG, acceptance bandwidths and walk-off angle were calculated using the Sellmeier equations given in Reference [107] and are also presented below.

4.3.1 Phase-matching

The theoretical calculations of the phase-matching curve in a BBO crystal for type-I ($oo{\rightarrow}e$) interaction for frequency-doubling are presented in Figure 4.5. The pump wavelength goes from 0.42 to 0.77 μm, showing a corresponding phase-matching angle from θ ~ 75º to 30º respectively. Of particular interest is the corresponding phase-matching angle at 0.532 μm due to the nature of our experiment, in which this frequency has been obtained previously by frequency-doubling the 1.064 μm pump. At 0.532 μm, BBO crystal presents a phase-matching angle of θ_{pm} = 47.43º for SHG, which has been used during this experiment. The effective non-linear coefficient, d_{eff}, in the working wavelength presents a value of 1.14 pm/V.
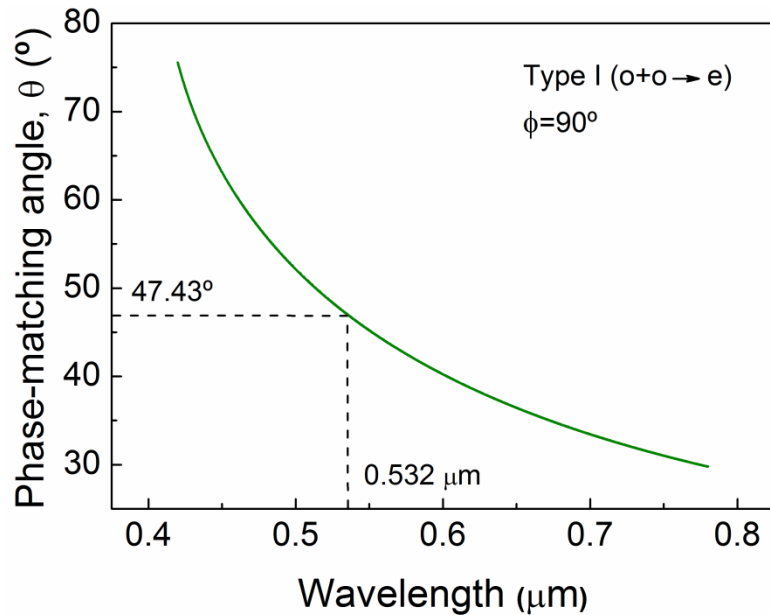
Figure 4.5: Phase-matching curve for SHG for type-I ($oo{\rightarrow}e$) interaction.

4.3.2 Acceptance bandwidths

Angular and spectral acceptance bandwidths are defined as the tolerance of phase-matching to the spatial and spectral spread of the input beam. As previously mentioned, these magnitudes compromise the output power and the conversion efficiency of the nonlinear process within the crystal. The calculated angular acceptance bandwidth curve is shown in Figure 4.6. The $sinc^2$ curve has a FWHM bandwidth of $\Delta\theta = 0.17$ mrad·cm at a fixed wavelength of 0.532 μm while the calculated spectral acceptance bandwidth curve, shown in Figure 4.7, presents a value given by the FWHM bandwidth of $\Delta\lambda = 0.07$ nm at a phase-matching angle of $\theta_{pm} = 47.43°$.
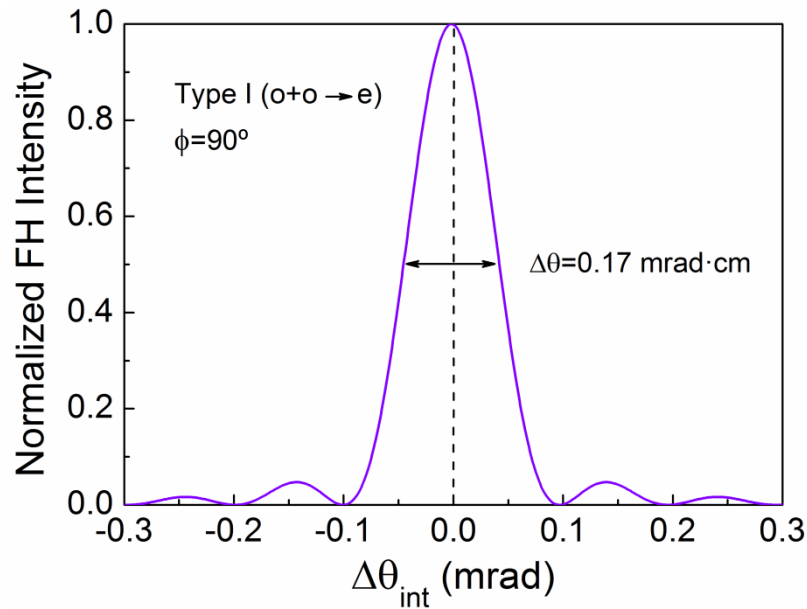
Figure 4.6: Angular acceptance bandwidth for SHG for type-I ($oo{\rightarrow}e$) interaction.
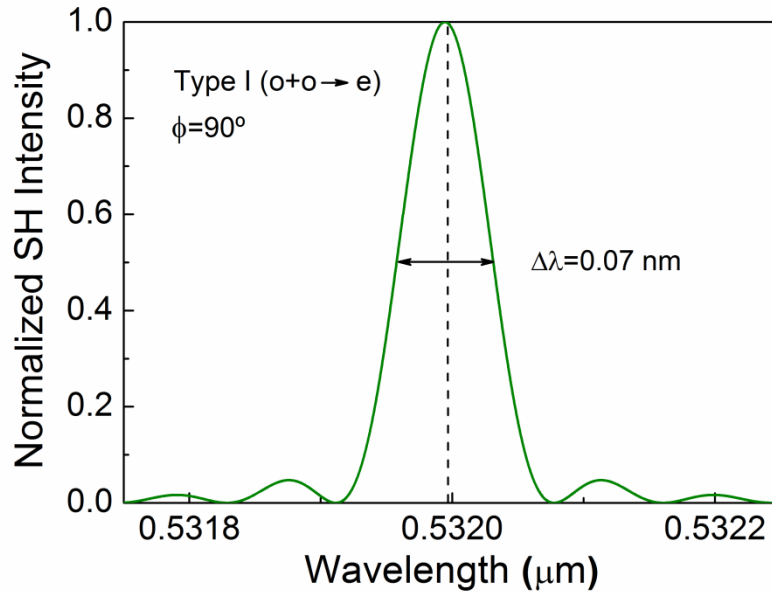
Figure 4.7: Spectral acceptance bandwidth for SHG for type-I (*oo→e*) interaction.

4.4 Power scaling and efficiency

After the previous full characterization of the LBO SHG output rigorously described in Chapter 3 (subsection 3.5.1), we performed the optimization of the SHG stage in order to perform FHG at 266 nm. Having a beam waist radius of $w_0 \sim 19$ μm, using an optimized focusing condition ($\xi = l/b \sim 1.4$) given by Boyd and Kleinman theory in the presence of crystals with spatial walk-off [60], we were able to generate a FH power as high as 1.65 W at 266 nm for a maximum input SH power of 8.3 W at the input to the BBO crystal, at a single-pass green-to-UV conversion efficiency of 19.2%. Nevertheless, the maximum conversion efficiency was obtained for an input SH power of 7.6 W, generating up to 1.48 W of UV power with a conversion efficiency of 19.5%, corresponding to an IR-to-UV nm conversion efficiency of 11%. Under this configuration, we corrected the transmission loss of the UV filter *F*, and after represented the values shown in Figure 4.8.
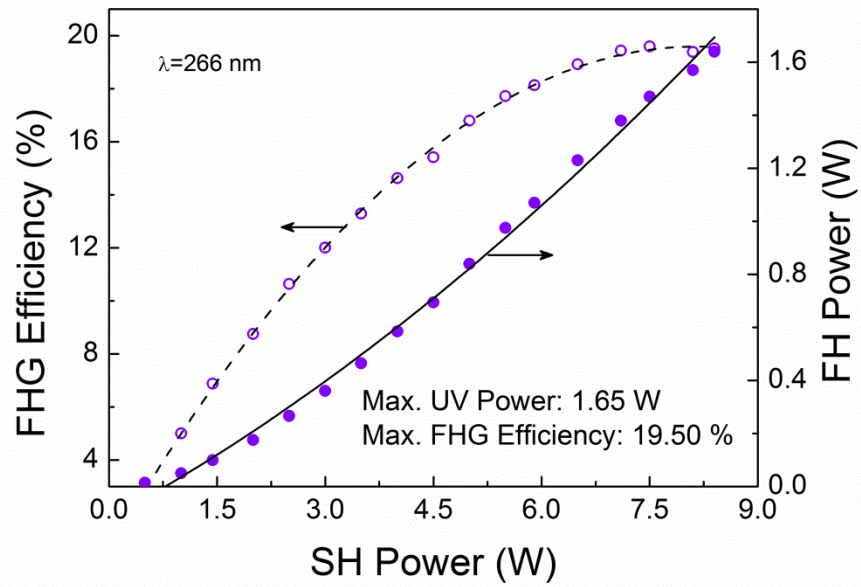
Figure 4.8: Variation of the FH power and FHG efficiency as a function of fundamental power.

Figure 4.9: Variation of the FH power as a function of the square of SH power.

The quadratic increase in the SH power and the corresponding linear variation in efficiency are maintained up to a SH power of ~6 W, beyond which saturation occurs. The saturation effect is also evident from the deviation of the linearity of the FH power with the square of SH power, as shown in Figure 4.9. Further investigations related to the UV transmission of BBO as well as the influence of the two-photon absorption are under investigation.
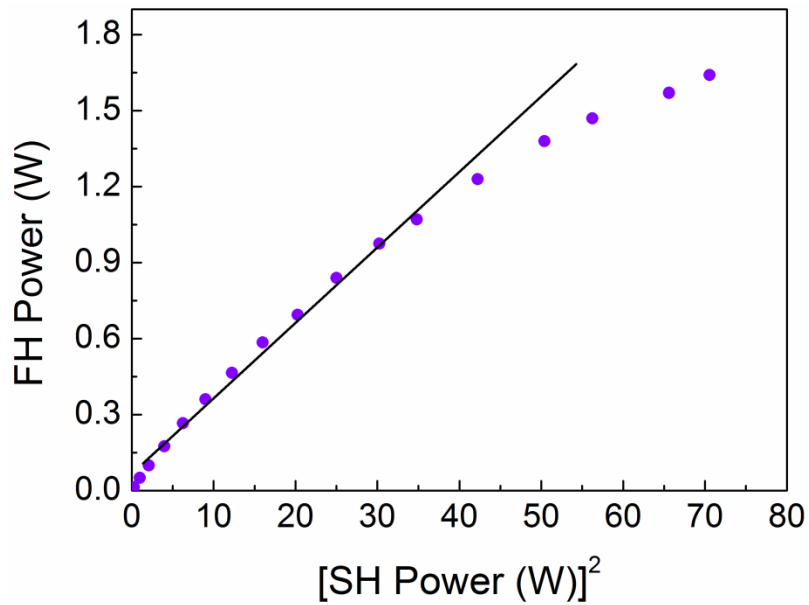
4.5 Power and temporal stability and spectrum

The passive long-term power stability of the generated UV output was recorded over 14 hours. The power stability of the pump laser was shown in Figure 3.9. As it can be seen in Figure 4.10, the UV power exhibits a long-term drift resulting in a slow decline from 1.2 W down to ~0.8 W after 14 hours, which could be attributed to two-photon absorption or dynamic color center formation, as previously observed in BBO [99]. Some reports describe decreases in the conversion efficiency and degradation in the beam quality deteriorating the stability [108,109]. Nevertheless, a part from the decrease in the UV power, no degradation in the beam quality has been observed so far. By translating the crystal to focus the input beam to a new position inside BBO, we could readily recover the maximum UV power. This also suggests that improved thermal and mechanical isolation of the system with proper temperature control and increased pump power stability can further enhance the FHG power stability even though the origin of the long-term power drop requires further studies. To our knowledge, such power stability measurements as performed here have not been previously reported for UV generation in earlier works involving BBO at any power level. We have not observed any permanent damage in the BBO crystal even after more than 14 hours of continuous
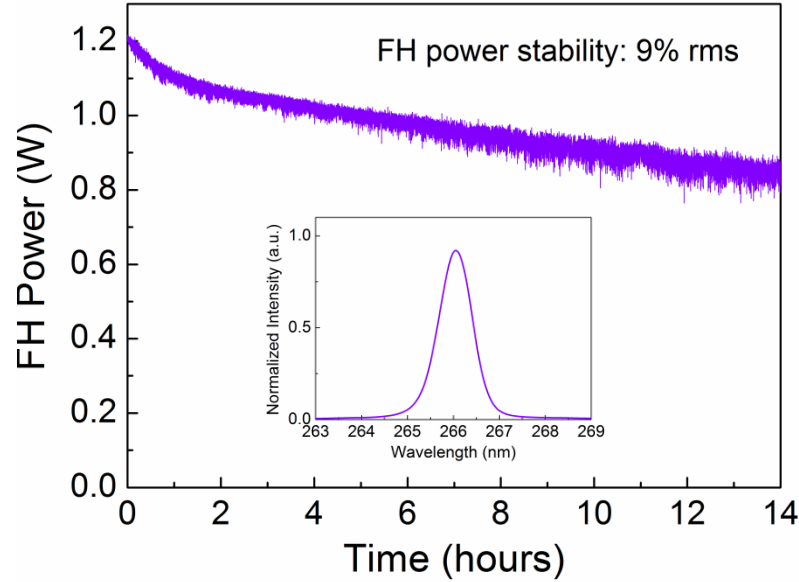
Figure 4.10: Long-term power stability of the UV source over 14 hours. Inset: UV

spectrum, presenting a FWHM of 0.8 nm broad.

operation and repeated operation over many days and weeks. Also shown in the

inset of Figure 4.10 is the UV spectrum centered at 266 nm, measured using

UV-visible spectrometer, indicating a bandwidth of ~0.8 nm (FWHM), limited by

the instrument resolution.

4.6 Output beam quality

In previous sections it was mentioned that for a successful attainment of maximum output

power and efficiency of any frequency conversion process, the angular separation of the

interacting waves within the nonlinear crystal, the walk-off, should be considered. Figure

4.11 shows the calculated walk-off angle at a phase-matching angle of $\theta_{pm} = 47.43°$ for

type-I ($oo{\rightarrow}e$) SHG of BBO crystal pumped at 532 nm. As the SH beam is ordinary

polarized, the FH beam at 266 nm experiences a spatial walk-off of $\rho \sim 85$ mrad.
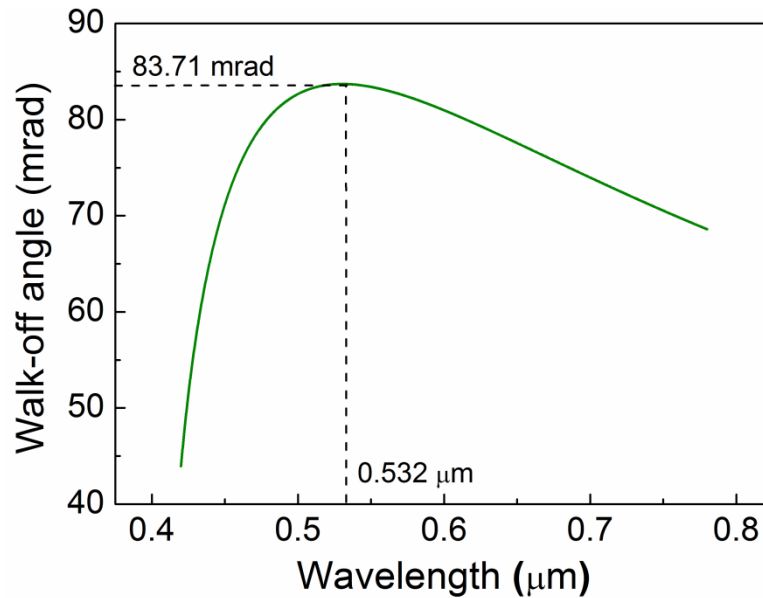
Figure 4.11: Variation of walk-off angle for type-I ($oo{\rightarrow}e$) phase-matching in BBO crystal as a function of fundamental wavelength.
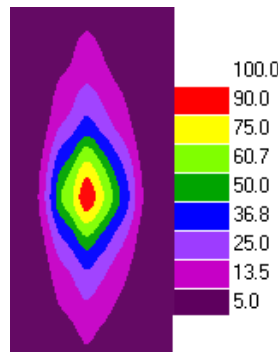
Figure 4.12: UV beam profile measured using a scanning beam profiler.

As a result, the generated UV beam is elliptic. In Figure 4.12 is shown the UV beam profile measured at 1.5 W of UV power. The image was captured using a scanning beam profiler after focusing the beam using a lens of $f = 150$ mm focal length. The image was captured exactly at the focal point of the lens. This makes evident the confirmation of the TEM$_{00}$ spatial mode. Furthermore, the UV beam is recorded to exhibit an ellipticity
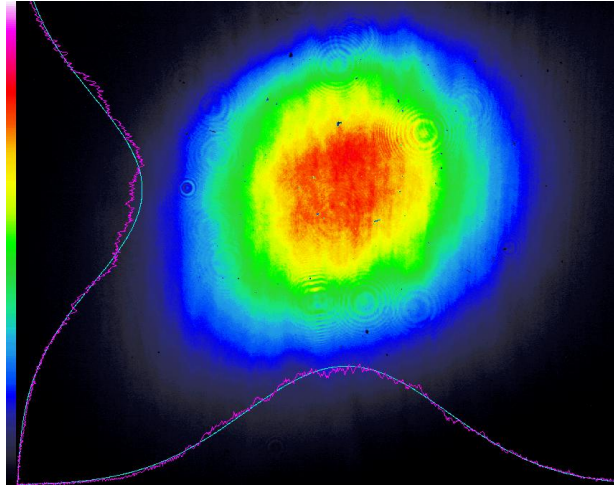
Figure 4.13: UV beam profile readily circularized using cylindrical optics.

attributed to the spatial walk-off between the SHG and the FHG beams. With the use of a suitable beam-shaping optics tools [94], circularization of the UV beam was readily feasible. The result is shown in Figure 4.13, together with the orthogonal intensity profiles and the corresponding Gaussian fits in the bottom and left sides of the image.

4.7 Conclusions

In conclusion, we have demonstrated a stable, high-power, high-repetition-rate, picosecond UV source based on single-pass FHG of a mode-locked 20-ps Yb-fiber-laser constituted by two consecutive SHG stages using LBO and BBO crystals, providing as much as 1.7 W of average power at 79.5 MHz, with a spectrum centered at 266 nm presenting a conversion efficiency from IR-to-UV of 11%. To our knowledge, this represents the highest watt-level single-pass FHG average power based in BBO crystal achieved with an ultrafast fiber laser to date. The generated UV radiation has a smooth and clean spectrum with a FWHM bandwidth of 0.8 nm centered at 266 nm. The FHG

output exhibits passive power stability better than 9% rms over 14 hours, in TEM_{00} beam profile. Together with the beam quality and good passive long-term power stability, the device represents a compact and highly practical picoseconds UV source for many practical and technological applications.

5 Summary and outlook

In this thesis we have demonstrated experiments within the framework of nonlinear frequency conversion for generating UV radiation in the picosecond time-scale at high repetition rates and high average power levels. Thanks to a deep knowledge and an excellent understanding of the properties of the utilized nonlinear crystals as well as optimized experimental techniques, we were able to improve the output features in the experiments presented in this thesis. In particular, by employing reliable concepts in nonlinear frequency conversion techniques, different experiments have been deployed using an assortment of experimental configurations resulting in a number of publications in which we emphasize in their compact, practical and robust design. The work presented in this thesis paves the way for future investigations aimed to improve the features of the high-power, picosecond UV sources.

The main outcomes of the work presented in this thesis include:

- The first demonstration of a compact, stable, high-power picosecond UV source at 355 nm based on single-pass SFG in BIBO pumped by a mode-locked Yb-fiber laser at 1064 nm comprising two stages in a novel multicrystal scheme, both

111

involving single-pass frequency conversion in BIBO. The source simultaneously generates 4.9 W of picosecond green power at 532 nm and 164 mW of picosecond UV power at 355 nm, which have been produced by a SHG scheme with the first BIBO crystal and, subsequently, frequency-mixed in a SFG scheme using a second BIBO crystal. A selective rotation of the polarization of the involved waves was introduced using a pair of high-order wave plates in order to promote a suitable interaction among the implicated waves in the second BIBO crystal and, thus, enhancing the 355 nm SFG providing up to 164 mW of output power at 80 MHz repetition-rate. Moreover, the setup presents excellent long-term passive stability better than 0.6% rms over 6 hours and high spatial beam quality with an elliptical TEM_{00} beam profile. Despite the limitations of low nonlinear conversion efficiency, by suitably deploying a two-crystal compensation scheme to further minimize the residual spatial walk-off in BIBO, the generated UV power could be further enhanced. Relevant theoretical calculations for the characterization of single-pass-SHG and SFG in the BIBO crystals have also been performed.

- A successful improvement of the previous experiment through the implementation of an LBO crystal as SH source, providing up to 9.1 W of average green power at 532 nm for a subsequent single-pass SFG in BIBO, generating up to 1.2 W of UV average power at 355 nm at 79.5 MHz repetition rate, corresponding to an IR-to-UV conversion efficiency of 7.2%. With regard to the power stability, it has resulted better than 0.4% rms over 3 hours, with a pointing stability better than 45 μrad over 1 hour, in TEM_{00} spatial profile. Besides, prospective improvements in the temporal overlap of 1064 nm and

532 nm pulses in the crystal by using a delay line could enhance the generated UV power. Further minimizations in the residual spatial walk-off in BIBO might be deployed using a two-crystal compensation scheme and thus enhancing the generated UV power. The obtained results confirm the viability of BIBO as a highly attractive material for efficient generation of low-intensity picosecond pulses in the UV.

- Further, we have also demonstrated a stable, high-power, high-repetition-rate, picosecond UV source based on single-pass FHG of a mode-locked 20-ps Yb-fiber-laser based in BBO crystal, providing as much as 1.7 W of average power at 79.5 MHz with a spectrum centered at 266 nm, representing an IR-to-UV conversion efficiency of 11%. The generated UV radiation presents a smooth and clean spectrum with a FWHM bandwidth of 0.8 nm centered at 266 nm limited by the resolution of the spectrometer. Moreover, the FHG source exhibits a passive power stability better than 9% rms over 14 hours, in an elliptic TEM_{00} beam profile. To the best of our knowledge, this is the first report of picosecond UV generation at 266 nm at MHz repetition rates, and at such high single-pass efficiency and average power based in BBO crystal achieved with an ultrafast fiber laser to date.

As a direction for the future work, the successful results presented in this thesis drives the possibility of further increase in the UV power to multi-watt levels with the power scaling potential of Yb-fiber lasers without damaging the BIBO crystal. Moreover, the performance of the BBO frequency-doubling stage in terms of power stability can further be improved by a better knowledge of the power transmission of the crystal and

the two-photon absorption effect. Besides, by isolating the BBO crystal from air currents using a proper crystal case could also affect positively in its conversion frequency features. The obtained results during this thesis confirm the viability of both BIBO and BBO crystals as highly attractive materials for efficient generation of high-power picosecond pulses in the UV.

Bibliography

[1]   T. H. Maiman, "Stimulated optical emission in ruby," *Nature,* (187), 493-495 (1960).

[2]   M. Ebrahim-Zadeh and I. T.Sorokina, "Mid-Infrared coherent sources and applications", 1st ed. Springer (2007).

[3]   M. Ebrahim-Zadeh, "Efficient Ultrafast Frequency Conversion Sources for the Visible and Ultraviolet Based on BiB_3O_6," *IEEE Journal of Selected Topics in Quantum Electronics,* **13**(3), 679 (2007) (Invited Paper).

[4]   J. A. Armstrong, N. Bloembergen, J. Ducuing and P. S. Pershan, "Interaction between light waves in a nonlinear dielectric," *Phys. Rev,* **127**, 1918-1939 (1962).

[5]   S. Chaitanya Kumar, "High-power, fiber-laser-pumped optical parametric oscillators from the visible to mid-infrared", Institute of Photonic Sciences: PhD thesis dissertation (2011).

[6]   Malcom H. Dunn and M. Ebrahim-Zadeh, "Parametric generation of tunable light from continuous-wave to femtosecond pulses," *Science,* **286**, 1513-1517 (1999).

[7]   M. Ebrahim-Zadeh, "Mid-Infrared ultrafast and continuous-wave optical parametric oscillators in solid-state mid-infrared laser sources", Springer-Verlag (2003).

[8]   M. F. L'Annunziata, "Radioactivity-Introduction and history", Elsevier (2007).

[9]   C. V. Raman and K. S. Krishnan, "A new type of secondary radiation," *Nature,*. **121**, 501-502 (1928).

[10] E. Schrodinger, "Nonlinear optics," *Proc. Royal Irish Academy,* **47** A, 77-117 (1942).

[11] E. Schrodinger, "A new exact solution in non-linear optics," *Proc. Royal Irish Academy,* **49** A, 59-66 (1943).

[12] P. A. Franken, A. E. Hill, C. W. Peters and G. Weinreich, "Generation of optical harmonics," *Phys. Rev. Lett.,* **7**(4), 118-119 (1961).

[13] M. Bass, P. A. Franken, A. E. Hill, C. W. Peters, and G. Weinreich, "Optical mixing," *Phys. Rev. Lett.,* **8**(1), 18 (1962).

[14] P. K. Tien, "Parametric amplification and frequency mixing in propagating circuits," *J. Appl. Phys.,* **29**(9), 1347-1357 (1958).

[15] P. K. Tien, and H. Suhl, "A traveling-wave ferromagnetic amplifier," *Proc. IRE,* **46**, 700-706 (1958).

[16] J. A. Giodmaine, "Mixing of light beams in crystals," *Phys. Rev. Lett.,* **8**(1), 19 (1962).

[17] R. H. Kingston, "Parametric amplification and oscillation at optical frequencies," *Proc. IRE,* **50**, 472–473 (1962).

[18] N. M. Kroll, "Parametric amplification in spatially extended media and application to the design of tuneable oscillators at optical frequencies," *Phys. Rev.,* **127**, 1207–1211 (1962).

[19] R. W. Terhune, P. D. Maker, and C. M. Savage, "Optical harmonic generation in calcite," *Phys. Rev. Lett.,* **8**(10), 404-406 (1962).

[20] A. W. Smith and N. Braslau, "Observation of an optical difference frequency," *J. Appl. Phys.,* **34**, 2105-2106 (1963).

[21] J. A. Giordmaine and R. C. Miller, "Tunable coherent parametric oscillation in LiNbO$_3$ at optical frequencies," *Phys. Rev. Lett.,* **14**, 973-976 (1965).

[22] R. G. Smith, J. E. Geusic, H. J. Levinstein, S. Singh, and L. G. Van Uitert,, "Low-threshold optical parametric oscillator using Ba$_2$NaNb$_5$O$_{15}$," *J. Appl. Phys.,* **39**, 4030-4032 (1968).

[23] R. L. Byer, M. K. Oshman, J. F. Young, and S. E. Harris, "Visible cw parametric oscillator," *Appl. Phys. Lett.,* **13**, 109-111 (1968).

[24] S. Matsumoto, E. J. Lim, H. M. Hertz, and M. M. Fejer, "Quasi-phase-matched second harmonic generation of blue light in electrically periodically-poled lithium tantalate waveguides," *Electron. Lett.,* **27**(22), 2040-2042 (1991).

[25] P. D. Maker, R. W. Terhune, M. Nissenoff and C. M. Savage, "Effects of dispersion and focusing on the production of optical harmonics," *Phys. Rev. Lett.,* **8**, 21-22 (1962).

[26] S. A. Akhmanov and R. V. Khokhlov, "Concerning one possibility of amplification of light waves," *Sov. Phys. J. Exp. Theor. Phys.,* **16**, 252–254 (1963).

[27] K. Devi, "Continuous-wave optical parametric oscillators and frequency conversion sources from the ultraviolet to the mid-infrared", Institute of Photonic Sciences: PhD thesis dissertation (2013).

[28] M. Ebrahim-Zadeh, "Advances in Ultrafast and Continuous-Wave Optical Parametric Oscillators," *IEEE PhotonicsGlobal@Singapore,* Vols. Paper D2-3-01, December (2008).

[29] S. Khripunov, D. Radnatarov, S. Kobtsev, and A. Skorkin, "Variable-wavelength second harmonic generation of cw Yb-fiber laser in partially coupled enhancement cavity," *Opt. Express,* **22**(6), 7046-7051 (2014).

[30] A. K. Jayasinghe, J. Rohner, and M. S. Hutson, "Holographic UV laser microsurgery," *Biomedical Opt. Express,* **2**(9), 2590-2599 (2011).

[31] C. L. Tang and L. K. Cheng, "Fundamentals of optical parametric processes and oscillators in Laser science and technology series", Harwood academic publishers (1995).

[32] M. Ghotbi, A. Esteban-Martin, and M. Ebrahim-Zadeh, "BiB_3O_6 femtosecond optical parametric oscillator," *Opt. Lett.,* **31**(21), 3128-3130 (2006).

[33] M. Ghotbi, A. Esteban-Martin, and M. Ebrahim-Zadeh, "Tunable, high-repetition-rate, femtosecond pulse generation in the ultraviolet," *Opt. Lett.,* **33**(4), 345-347 (2008).

[34] H. Hellwig, J. Liebertz, L. Bohaty, "Exceptional large nonlinear optical coefficients

in the monoclinic bismuth borate BiB_3O_6 (BIBO)," *Solid State Commun.,* **109**, 249 (1999).

[35] H. Hellwig, J. Liebertz, and L. Bohaty, "Linear optical properties of the monoclinic bismuth borate BiB_3O_6," *J. Appl. Phys.,* **88**(1), 240-244 (2000).

[36] M. Ghotbi, Z. Sun, A. Majchrowski, E. Michalski, I. V. Kityk and M. Ebrahim-Zadeh, "Efficient third harmonic generation of microjoule picosecond pulses at 355 nm in BiB_3O_6," *Appl. Phys. Lett.,* **89**(17), 173124-173124 (2006).

[37] M. Ghotbi, Z. Sun, A. Majchrowski, E. Michalski, I. V. Kityk and M. Ebrahim-Zadeh, "High-average-power femtosecond pulse generation in the blue using BiB_3O_6," *Opt. Lett.,* **29**(21), 2530-2532 (2004).

[38] M. Ghotbi and M. Ebrahim-Zadeh, "990 mW average power, 50% efficient, high-repetition-rate picosecond-pulse generation in the blue with BiB_3O_6," *Opt. Lett.,* **30**(24), 3395-3397 (2005).

[39] S. Chaitanya Kumar and M. Ebrahim-Zadeh, "High-power, fiber-pumped, picosecond green source based on BiB_3O_6," *Laser Phys.,* **24**, 025401 (2014).

[40] S. Chaitanya Kumar, K. Devi and M. Ebrahim-Zadeh, "Stable, continuous-wave, ytterbium-fiber-based single-pass ultraviolet source using BiB_3O_6," *Opt. Lett.,* **38**(23), 5114-5117, (2013).

[41] P. E. Powers, Thomas J. Kulp, and S. E. Bisson, "Continuous tuning of a continuous-wave periodically poled lithium niobate optical parametric oscillator by use of a fan-out grating design," *Opt. Lett.,* **23**(3), 159-161 (1998).

[42] A. J. Henderson and R. Stafford, "Intra-cavity power effects in singly resonant cw OPOs," *Appl. Phys. B,* **85**(2-3), 181-184 (2006).

[43] S. Chaitanya Kumar, R. Das, G. K. Samanta, M. Ebrahim-Zadeh, "Optimally output-coupled, 17.5 W, fiber-laser-pumped continuous-wave optical parametric oscillator," *Appl. Phys. B: Lasers Opt.,* **102**(1), 31-35 (2011).

[44] G. K. Samanta, G. R. Fayaz, Z. Sun, and M. Ebrahim-Zadeh, "Highpower, continuous-wave, singly resonant optical parametric oscillator based on MgO:sPPLT," *Opt. Lett.,* **32**(4), 400-402 (2007).

[45] R. W. Boyd, "Nonlinear Optics", San Diego, USA: Academic Press (2007).

[46] R. L. Sutherland, "Handbook of nonlinear optics", 2nd edition, Marcel Dekker, Inc. (1996).

[47] E. Sánchez Bautista, Characterization of femtosecond pulses from *xz* BIBO OPO, Institute of Photonic Sciences: MSc. thesis dissertation (2011).

[48] V. Ramaiah-Badarla, Ultrafast optical parametric oscillators. Novel systems, techniques, and concepts, Institute of Photonic Sciences: PhD thesis dissertation (2014).

[49] V. Ramaiah-Badarla, A. Esteban-Martin and M. Ebrahim-Zadeh, "Self-phase-locked degenerate femtosecond optical parametric oscillator based on BiB$_3$O$_6$," *Laser Photonics Rev.,* **7**(5), L55–L60 (2013).

[50] M. Ebrahim-Zadeh, S. Chaitanya Kumar, A. Esteban-Martin and G. K. Samanta, "Breakthroughs in photonics 2012: Breakthroughs in optical parametric oscillators," *IEEE Photon. J.,* **5**, 0700105 (2013).

[51] R. W. Munn and C. N. Ironside, "Nonlinear optical materials", CRC Press, (1993).

[52] D. A. Kleinman, "Nonlinear dielectric polarization in optical media," *Phys. Rev.,* **126**, 1977-1979 (1962).

[53] P. A. Franken and J. F. Ward, "Rev. Mod. Phys.," *Optical harmonics and nonlinear phenomena,* **35**, 23-29 (1963).

[54] B. Jaffe, W. Cooke, and H. Jaffe, "Piezoelectric Ceramics", Academic Press (1971).

[55] F. Zernike and J. E. Midwinter, "Applied nonlinear optics", Wiley (1973).

[56] M. Ebrahim-Zadeh, "Parametric light generation," *R. Soc. Lond. A,* **361**, 2731-2750 (2003).

[57] "http://en.wikipedia.org/wiki/Slowly_varying_envelope_approximation," [Online].

[58] "http://en.wikipedia.org/wiki/Plane_wave," [Online].

[59] D. S. Hum, M. M. Fejer, "Quasi-phasematching," *C. R. Physique,* **8**, 108-198 (2007).

[60] G. D. Boyd and D. A. Kleinman, "Parametric interaction of focused Gaussian light beams," *J. Appl. Phys.,* **39**, 3597-3639 (1968).

[61] M. Abramowitz and I. Stegun, "Handbook of Mathematical Functions", Dover, NY

(1965).

[62] D. Eimerl, "High average power harmonic generation," *IEEE J. Quantum Elect.,* **23**(5), 575-592 (1987).

[63] R. C. Eckardt and J. Reintjes, "Phase-matching limitations of high efficiency second-harmonic generation," *IEEE J. Quantum Elect.,* **20**, 1178-1187 (1984).

[64] P. F. Byrd and M. D. Friedman, Handbook el Elliptic Integrals for Engineers and Scientist, New York: Springer-Verlag (1971).

[65] M. Ebrahim-Zadeh and M. H. Dunn, "Optical parametric oscillators, Handbook of optics", 2nd ed., Chapter. 22, Washington, D.C.: Optical Society of America (2000).

[66] M. M. Fejer, G. A. Magel, D. H. Jundt, and R. L. Byer, "Quasi-phase-matched second harmonic generation: Tuning and tolerances," *IEEE J. Quantum Elect.,* **28**, 2631-2654 (1992).

[67] D. N. Nikogosyan, "Nonlinear Optical Crystals: A Complete Survey", Cork, Ireland: Springer (2005).

[68] "http://en.wikipedia.org/wiki/Envelope_%28waves%29," [Online].

[69] J. C. Diels and W. Rudolph, "Ultrashort laser pulse phenomena", Academic press (2006).

[70] C. Rulliere, "Femtosecond laser pulses", **2**, Springer (1998).

[71] A. M. Weiner, "Ultrafast optics", Wiley series in pure and applied optics (2009).

[72] T. Rauch, and R. Delmdahl, "Advanced UV lasers enable precision processing," *Laser Tech. J,* **6**, 20-24 (2009).

[73] D. Karnakis, A. Kearsley and M. Knowles, "Ultrafast laser patterning of OLEDs on flexible substrate for solid-state lighting," *J. Laser Micro/Nanoengineering,* **4**(3), 218-223 (2009).

[74] V. Kubecek, S. Kumazaki, A. Agnesi, G. C. Reali, Y. Takagi, and K. Yoshihara, "*β*-Barium borate and lithium triborate picosecond parametric oscillators pumped by a frequency-tripled passive negative-feedback mode-locked Nd:YAG laser," *J. Opt. Soc. Am. B,* **10**(11), 2211-2217 (1993).

[75] A. N. Chaitanya, A. Aadhi, R. P. Singh, and G. K. Samanta, "Type-I frequency-doubling characteristics of high-power, ultrafast fiber laser in thick BIBO crystal,"

Opt. Lett., **39**(18), 5419-5422 (2014).

[76] V. Petrov, M. Ghotbi, O. Kokabee, A. Esteban-Martin, F. Noack, A. Gaydardzhiev, I. Nikolov, P. Tzankov, I. Buchvarov, K. Miyata, A. Majchrowski, I. Kityk, F. Rotermund, E. Michalski, and M. Ebrahim-Zadeh, "Femtosecond nonlinear frequency conversion based on BiB$_3$O$_6$," *Laser & Photon. Rev.,* **4**(1), 53-98 (2010).

[77] M. Peltz, J. Bartschke, A. Borsutzky, R. Wallenstein, S. Vernay, T. Salva and D. Rytz, "Harmonic generation in bismuth triborate (BiB$_3$O$_6$)," *Appl. Phys. B,* **81**(4), 487-495 (2005).

[78] G. K. Samanta, S. Chaitanya Kumar, A. Aadhi, and M. Ebrahim-Zadeh, "Yb-fiber-laser-pumped, high-repetition-rate picosecond optical parametric oscillator tunable in the ultraviolet," *Opt. Express,* **22**(10), 11476-11487 (2014).

[79] M. Ghotbi and M. Ebrahim-Zadeh, "Optical second-harmonic generation properties of BiB$_3$O$_6$," *Optics Express,* **12**(24), 6002-6019 (2004).

[80] N. M. Wakida, C. S. Lee, E. T. Botvinick, L. Z. Shi, A. Dvornikov and M. W. Berns, "Laser nanosurgery of single microtubules reveals location-dependent depolymerization rates," *Journal Biomed. Opt.,* **12**(2), 024022 (2007).

[81] Z. Zhao, B. M. Dunham, I. Barzarov and F. W. Wise, "Generation of 110 W infrared and 65 W green power from a 1.3-GHz sub-picosecond fiber amplifier," *Opt. Express,* **20**(5), 4850 (2012).

[82] Q. Liu, F. Lu, M. Gong, C. Li and D. Ma, "15 W output power diode-pumped solid-state lasers at 515 nm," *Phys. Lett.,* **4**(1), 30 (2007).

[83] Y. Shao, D. Zhang, H. P. Liu, H. J. Jin, Y. L. Li, Z. H. Tao, Q. R. Ruan and T. Y. Zhang, "Continuous-wave green thin-disk laser at 524 nm based on frequency-doubled diode-pumped Yb:GSO crystal," *Laser Phys. Lett.,* **8**(8), 587 (2011).

[84] B. Liu and Y. L. Li, "Diode-pumped frequency-doubled Yb:SYS-LBO green laser at 534 nm," *Laser Phys. Lett.,* **8**(9), 653 (2011).

[85] V. A. Akulov, D. M. Afanasiev, S. A. Babin, D. V. Churkin, S. I. Kablukov, M. A. Rybakov and A. A. Vlasov, "Frequency tuning and doubling in Yb-doped fiber lasers," *Laser Phys.,* **17**(2), 124 (2007).

[86] V. A. Akulov, S. A. Babin, S. I. Kablukov and A. A. Vlasov, "Fiber lasers with a

tunable green output," *Laser Phys.,* **18**(11), 1225-1229 (2008).

[87] V. A. Akulov, S. A. Babin, S. I. Kablukov and K. S. Raspopin, "Intracavity frequency doubling of Yb-doped fiber laser with 540–550 nm tuning," *Laser Physics,* **21**(5), 935-939 (2011).

[88] S. M. Riecke, K. Lauritsen, R. Erdmann, M. Uebernickel, K. Paschke and G. Erbert, "Pulse-shape improvement during amplification and second-harmonic generation of picosecond pulses at 531 nm," *Opt. Lett.,* **35**(10), 1500 (2010).

[89] S. Chaitanya Kumar, G. K. Samanta and M. Ebrahim-Zadeh, "High-power, single-frequency, continuous-wave second-harmonic-generation of ytterbium fiber laser in PPKTP and MgO:sPPLT," *Opt. Express,* **17**(16), 13711-13726 (2009).

[90] S. Chaitanya Kumar, K. Devi, G. K. Samanta and M. Ebrahim-Zadeh, "Fiber-laser-based green-pumped continuous-wave singly-resonant optical parametric oscillator," *Laser Phys.,* **21**(4), 782-789 (2012).

[91] S. Chaitanya Kumar, G. K. Samanta, K. Devi and M. Ebrahim-Zadeh, "High-efficiency, multicrystal, single-pass, continuous-wave second harmonic generation," *Opt. Express,* **19**(12), 11152-11169 (2011).

[92] K. Li, L. Zhang, D. Xu, G. Zhang, H. Yu, Y. Wang, F. Shan, L. Wang, C. Yan, Y. Wu, X. Lin and J. Yao, "High-power picosecond 355 nm laser based on $La_2CaB_{10}O_{19}$ crystal," *Opt. Lett.,* **39**(11), 3305-3307 (2014).

[93] J. Yao, W. Sheng, and W. Shi, " Accurate calculation of the optimum phase-matching parameters in three-wave interactions with biaxial nonlinear-optical crystals," *J. Opt. Soc. Am. B,* **9**(6), 891-902 (1992).

[94] "http://www.newport.com/Beam-Shaping-with-Cylindrical-Lenses/144888/1033/content.aspx," [Online].

[95] W. G. Telford, *Cytometry,* **54**(1), 48 (2003).

[96] M. Shahidi, H. Jara, H. Pummer, H. Egger, and C. K. Rhodes, "Optically excited XeF* excimer laser in liquid argon," *Optics Letters,* **10**(9), 448-450 (1985).

[97] D. N. Nikogosyan, "Lithium Triborate (LBO)," *Appl. Phys. A,* **58**(3), 181-190 (1994).

[98] J. H. Jang, I. H. Yoon, C. S. Yoon, "Cause and repair of optical damage in

nonlinear optical crystals of BiB_3O_6," *Opt. Mater.,* **31**(6), 781-783 (2009).

[99] M. Takahashi, A. Osada, A. Dergachev, P. F. Moulton, M. Cadatal-Raduban, T. Shimizu, N. Sarukura, "Improved fourth harmonic generation in β-BaB_2O_4 by tight elliptical focusing perpendicular to walk-off plane," *J. Cryst. Growth.,* **318**(1), 606-609 (2011).

[100] C. X. Wang, G. Y. Wang, A. V. Hicks, D. R. Dudley, H. Y. Pang and N. Hodgson, "High-power Q-switched TEM_{00} mode diode pumped solid state lasers with >30 W output power at 355 nm," *Proc. SPIE,* **6100**, 335–348 (2006).

[101] S. Orthaus, M. König, T. Schönau, V. Buschmann, S. Tannert, C. Lauritsen, F. Koberling, U. Ortmann and R. Erdmann, "Time-resolved microscopy of native fluorophores," *Optik & Photonik,* **8**(1), 33-36 (2013).

[102] L. Wang, N. Zhai, L. Liu, X. Wang, G. Wang, Y. Zhu and C. Chen, "High-average-power 266 nm generation with a $KBe_2BO_3F_2$ prism-coupled device," *Optics Express,* **22**(22), 27086-27093 (2014).

[103] M. Oka, L. Y. Liu, W. Wiechmann, N. Eguchi and S. Kubota, "All solid-state continuous-wave frequency-quadrupled Nd:YAG laser," *IEEE J. Sel. Top. Quantum Electron.,* **1**(3), 859-866 (1995).

[104] L. B. Chang, S. C. Wang and A. H. Kung, "Efficient compact watt-level deep-ultraviolet laser generated from a multi-kHz Q-switched diode-pumped solid-state laser system," *Opt. Commun.,* **209**(4-6), 397-401 (2002).

[105] T. Südmeyer, Y. Imai, H. Masuda, N. Eguchi, M. Saito and S. Kubota, "Efficient 2nd and 4th-harmonic generation of a single-frequency, continuous-wave fiber amplifier," *Opt. Express,* **16**(3), 1546–1551 (2008).

[106] Q. Liu, X. P. Yan, X. Fu, M. Gong and D. S. Wang, "High power all-solid-state fourth-harmonic generation of 266 nm at the pulse repetition rate of 100 kHz," *Laser Phys. Lett.,* **6**(3), 203–206 (2009).

[107] D. N. Nikigosyan, "Beta barium borate (BBO)," *Applied Physics,* **52**(6), 359-368 (1991).

[108] S. Wu, G. A. Blake, S. Sun and H. Yu, "Two-photon absorption inside β-BBO crystal during UV nonlinear optical conversion," *Proc. SPIE ,* **3928**, 29–35 (2000).

[109] N. Kondratyuk and A. Shagov, "Nonlinear absorption at 266nm in BBO crystal and its influence on frequency conversion," *Proc. SPIE,* **47518**, 110–115 (2002).